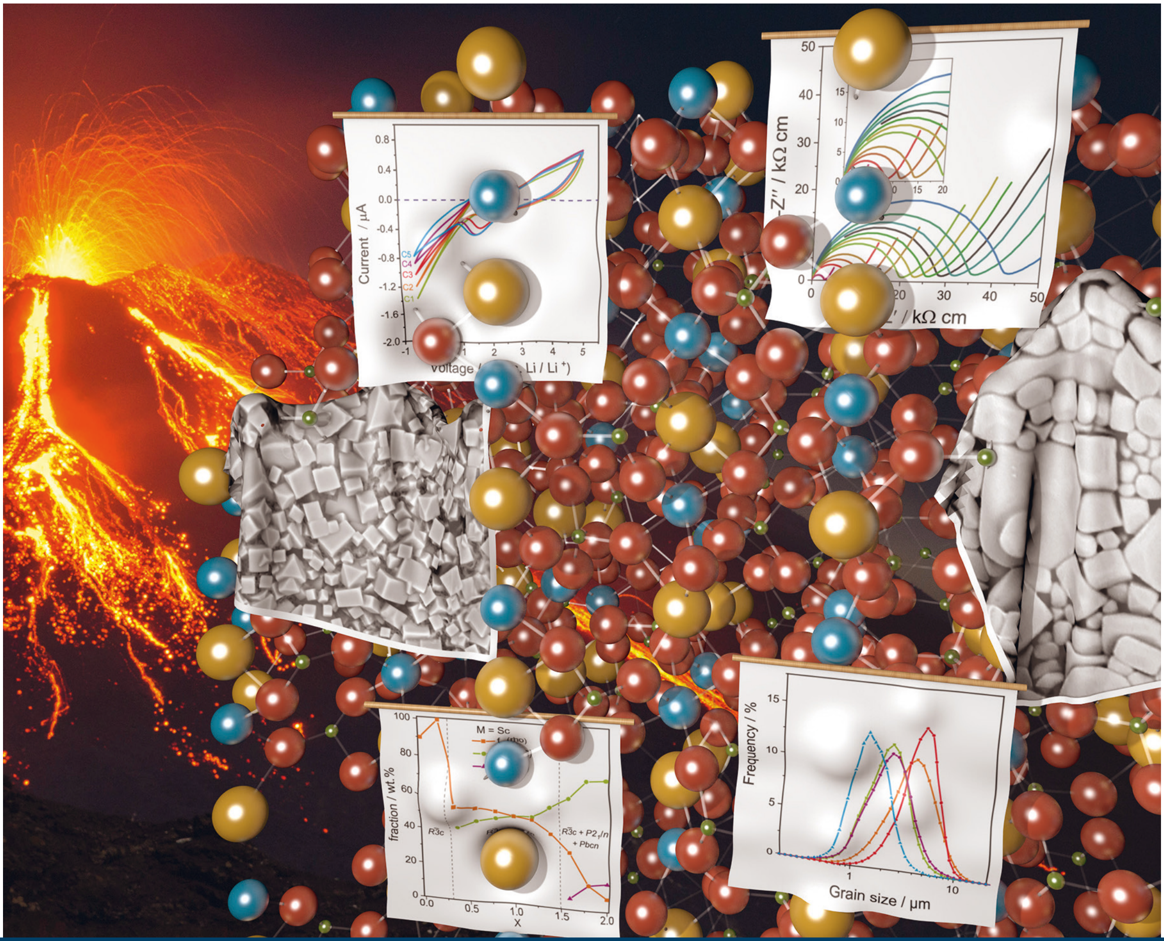

Optimization of NaSICON-type lithium- ion conductors for solid-state batteries

Asmaa Loutati

Energie & Umwelt / Energy & Environment
Band / Volume 664
ISBN 978-3-95806-824-7

Mitglied der Helmholtz-Gemeinschaft

JÜLICH
Forschungszentrum

Schriften des Forschungszentrums Jülich
Reihe Energie & Umwelt / Energy & Environment Band / Volume 664

Forschungszentrum Jülich GmbH
Institute of Energy Materials and Devices (IMD)
Werkstoffsynthese und Herstellungsverfahren (IMD-2)

Optimization of NaSICON-type lithium- ion conductors for solid-state batteries

Asmaa Loutati

Schriften des Forschungszentrums Jülich
Reihe Energie & Umwelt / Energy & Environment Band / Volume 664

ISSN 1866-1793 ISBN 978-3-95806-824-7

Bibliografische Information der Deutschen Nationalbibliothek.
Die Deutsche Nationalbibliothek verzeichnet diese Publikation in der
Deutschen Nationalbibliografie; detaillierte Bibliografische Daten
sind im Internet über http://dnb.d-nb.de abrufbar.

Herausgeber und Vertrieb: Forschungszentrum Jülich GmbH
Zentralbibliothek, Verlag
52425 Jülich
Tel.: +49 2461 61-5368
Fax: +49 2461 61-6103
zb-publikation@fz-juelich.de
www.fz-juelich.de/zb

Umschlaggestaltung: Grafische Medien, Forschungszentrum Jülich GmbH

Druck: Grafische Medien, Forschungszentrum Jülich GmbH

Schriften des Forschungszentrums Jülich
Reihe Energie & Umwelt / Energy & Environment, Band / Volume 664

D 464 (Diss. Duisburg-Essen, Univ., 2024)

ISSN 1866-1793
ISBN 978-3-95806-824-7

Vollständig frei verfügbar über das Publikationsportal des Forschungszentrums Jülich (JuSER)
unter www.fz-juelich.de/zb/openaccess.

Abstract

The continuing depletion of fossil fuels, rising oil prices and the need to reduce CO_2 emissions have stimulated intensive research into alternative energy technologies based on renewable and clean sources. Among the various technologies, electrochemical energy storage in rechargeable lithium-ion batteries (LIBs) plays an important role, both for powering a wide range of electronic devices and electric vehicles, and for storing electricity generated from alternative energy sources such as solar and wind. Commercial LIBs using organic liquid electrolytes dominate the market. However, the reactivity of liquid electrolytes at very positive or negative potentials limits the choice of suitable electrode materials and thus the available energy density. In addition, the toxicity and flammability of organic electrolytes raise serious safety concerns.

As an alternative to conventional liquid electrolyte LIBs, solid-state battery (SSB) concepts using solid electrolytes (SEs) are currently under intense investigation. Among numerous classes of materials, ceramic SEs are particularly attractive due to their non-flammability, relatively high ionic conductivity at room temperature (RT) and high chemical stability in air, resulting in potentially very high intrinsic safety of the batteries. In particular, Li-containing NaSICONs (Na Super Ionic CONductors) are currently receiving a great deal of attention due to the large structural variability and high ionic conductivity that can be achieved by substituting the lattice framework with various elements. Within this class of materials, lithium aluminum germanium phosphate $Li_{1+x}Al_xGe_{2-x}(PO_4)_3$ (LAGP) and lithium aluminum titanium phosphate $Li_{1+x}Al_xTi_{2-x}(PO_4)_3$ (LATP) are solid-state Li-ion conductors with the highest ionic conductivity at RT. However, the main drawback of germanium and titanium-containing materials is the low electrochemical stability at negative potentials caused by the reduction of Ge^{4+} to Ge^{2+} and Ti^{4+} to Ti^{3+}, which prevents the use of lithium metal anodes and reduces the energy density of the battery. To overcome this problem, the aim of this work was to increase the reduction stability of NaSICON compounds by replacing Ge and Ti with more reduction stable ions. To this end, various compositions of the type $Li_{1+x}M^{3+}_xZr_{2-x}(PO_4)_3$, where $M^{3+} = Al^{3+}, Sc^{3+}, Y^{3+}$, were synthesized by solution-assisted solid-state reaction. The effect of substitution on crystallographic parameters, relative density, sintering temperature, ionic conductivity, and electrochemical stability was

systematically investigated. The cationic substitution of M^{3+} (M = Al, Sc, Y) for Zr^{4+} in $LiZr_2(PO_4)_3$ (LZP) stabilizes the rhombohedral NaSICON structure (space group $R\bar{3}c$) at RT and increases the ionic conductivity significantly. Here, at 25 °C and with a comparable relative density of 94-96 %, an ionic conductivity of 2.7×10^{-5} S cm^{-1}, 6.7×10^{-5} S cm^{-1} and 3.6×10^{-6} S cm^{-1} was achieved with the compositions $Li_{1.2}Sc_{0.2}Zr_{1.8}(PO_4)_3$, $Li_{1.2}Y_{0.2}Zr_{1.8}(PO_4)_3$ and $Li_{1.2}Al_{0.2}Zr_{1.8}(PO_4)_3$, respectively. Compared to $Li_{1+x}Sc_xZr_{2-x}(PO_4)_3$, the Y^{3+} substitution in LZP slightly enhanced the ionic conductivity and marked the maximum Li^+-ion conductivity at RT with composition x = 0.2 in the whole system $Li_{1+x}M^{3+}{}_xZr_{2-x}(PO_4)_3$. However, the Al^{3+}-substitution decreased the ionic conductivity at RT.

In addition to cationic substitution, the effect of polyanionic substitution on ionic conductivity was investigated in the two materials series $Li_{3+x}Sc_2Si_xP_{3-x}O_{12}$ ($0 \leq x \leq 0.6$) and $Li_{1.2+x}Sc_{0.2}Zr_{1.8}Si_xP_{3-x}O_{12}$ ($0.3 \leq x \leq 2.8$). The substitution of $(PO_4)^{3-}$ with $(SiO_4)^{4-}$ in the system Li_2O-Sc_2O_3-ZrO_2-SiO_2-P_2O_5 effectively lowers the sintering temperature. Moreover, the introduction of zirconium can limit the evaporation of lithium species even at high sintering temperature. Silicate substitution in $Li_{3+x}Sc_2Si_xP_{3-x}O_{12}$ ($0 \leq x \leq 0.6$) has been shown to stabilize the monoclinic symmetry (space group $P2_1/n$) resulting in the increase of total ionic conductivity. The ionic conductivity at 25 °C increased from 2×10^{-6} S cm^{-1} for x = 0 to 1.2×10^{-5} S cm^{-1} for x = 0.15, which is the highest ionic conductivity of the investigated compositions in the Li_2O-Sc_2O_3-ZrO_2-SiO_2-P_2O_5 system. The purity of the NaSICON materials has a strong influence on the grain boundary resistance and thus on the ionic conductivity.

Selected ceramic NaSICON electrolytes such as LZP, $Li_{1.2}Y_{0.2}Zr_{1.8}(PO_4)_3$, and $Li_3Sc_2(PO_4)_3$ (LSP) were found to be more stable with respect to lithium than LATP and LAGP. LSP proved to be chemically and electrochemically very stable and might act as an anode protection material in combination with lithium metal.

Kurzfassung

Die anhaltende Erschöpfung fossiler Brennstoffe, steigende Ölpreise und die Notwendigkeit, den CO_2-Ausstoß zu reduzieren, haben eine intensive Forschung zu alternativen Energietechnologien auf der Grundlage erneuerbarer und sauberer Quellen angeregt. Unter den verschiedenen Technologien spielt die elektrochemische Energiespeicherung in wiederaufladbaren Lithium-Ionen-Batterien (LIBs) eine wichtige Rolle, sowohl für den Antrieb verschiedenster elektronischer Geräte und Elektrofahrzeuge als auch für die Speicherung von Strom aus alternativen Energiequellen wie Sonne und Wind. Kommerzielle LIBs mit organischen Flüssigelektrolyten dominieren den Markt. Allerdings schränkt die Reaktivität flüssiger Elektrolyte bei sehr positiven oder negativen Potentialen die Auswahl geeigneter Elektrodenmaterialien und damit die verfügbare Energiedichte ein. Darüber hinaus werfen die Toxizität und Entflammbarkeit organischer Elektrolyte ernsthafte Sicherheitsbedenken auf.

Als Alternative zu herkömmlichen Flüssigelektrolyt-LIBs werden derzeit Konzepte für Festkörperbatterien (SSB) mit Festelektrolyten (SEs) intensiv untersucht. Unter zahlreichen Materialklassen sind keramische Festelektrolyte aufgrund ihrer Nichtentflammbarkeit, ihrer relativ hohen Ionenleitfähigkeit bei Raumtemperatur und ihrer hohen chemischen Stabilität an der Luft besonders attraktiv, was zu einer potenziell sehr hohen Eigensicherheit der Batterien führt. Insbesondere Li-haltige NaSICONs (Na Super Ionic CONductors) erfahren derzeit große Aufmerksamkeit aufgrund der großen Strukturvariabilität und hohen Ionenleitfähigkeit, die durch den Ersatz des Gittergerüsts durch verschiedene Elemente erreicht werden können. Innerhalb dieser Materialklasse sind Lithiumaluminiumgermaniumphosphat $Li_{1+x}Al_xGe_{2-x}(PO_4)_3$ (LAGP) und Lithiumaluminiumtitanphosphat $Li_{1+x}Al_xTi_{2-x}(PO_4)_3$ (LATP) Festkörper-Li-Ionenleiter mit der höchsten Ionenleitfähigkeit bei Raumtemperatur. Der Hauptnachteil germanium- und titanhaltiger Materialien ist jedoch die geringe elektrochemische Stabilität bei negativen Potentialen, die durch die Reduktion von Ge^{4+} zu Ge^{2+} und Ti^{4+} zu Ti^{3+} verursacht wird, was den Einsatz von Lithium-Metallanoden verhindert und die Energiedichte der Batterie verringert. Um dieses Problem zu überwinden, bestand das Ziel dieser Arbeit darin, die Reduktionsstabilität von NaSICON-Verbindungen zu erhöhen, indem Ge und Ti durch reduktionsstabilere Ionen ersetzt wurden. Zu diesem Zweck wurden verschiedene Zusammensetzungen des Typs $Li_{1+x}M_{3+x}Zr_{2-x}(PO_4)_3$, wobei $M^{3+} = Al^{3+}$, Sc^{3+}, Y^{3+}, durch lösungsunterstützte Festkörperreaktion synthetisiert. Der Einfluss der Substitution auf kristallographische Parameter, relative Dichte, Sintertemperatur, Ionenleitfähigkeit und elektrochemische Stabilität wurde systematisch untersucht. Der kationische Ersatz von Zr^{4+} durch M^{3+} (M = Al, Sc, Y) in $LiZr_2(PO_4)_3$ stabilisiert die rhomboedrische NaSICON-Struktur (Raumgruppe $R\bar{3}c$) bei Raumtemperatur und erhöht die Ionenleitfähigkeit deutlich. Hier wurde bei 25 °C und einer vergleichbaren relativen Dichte von 94-96 % eine Ionenleitfähigkeit von 2.7×10^{-5} S cm^{-1}, 6.7×10^{-5} S cm^{-1} und 3.6×10^{-6} S cm^{-1} mit den Zusammensetzungen $Li_{1.2}Sc_{0.2}Zr_{1.8}(PO_4)_3$, $Li_{1.2}Y_{0.2}Zr_{1.8}(PO_4)_3$ and $Li_{1.2}Al_{0.2}Zr_{1.8}(PO_4)_3$ erreicht. bzw. Im Vergleich zu $Li_{1+x}Sc_xZr_{2-x}(PO_4)_3$ erhöhte die Y^{3+}-Substitution in $LiZr_2(PO_4)_3$ die Ionenleitfähigkeit leicht und markierte die maximale Li^+-Ionenleitfähigkeit bei Raumtemperatur mit der Zusammensetzung x = 0,2 im gesamten System $Li_{1+x}M_{3+x}Zr_{2-x}(PO_4)_3$. Allerdings verringerte die Al^{3+}-Substitution die Ionenleitfähigkeit bei Raumtemperatur.

Zusätzlich zur kationischen Substitution wurde der Einfluss der polyanionischen Substitution auf die Ionenleitfähigkeit in den beiden Materialreihen $Li_{3+x}Sc_2Si_xP_{3-x}O_{12}$ ($0 \leq x \leq 0{,}6$) und $Li_{1.2+x}Sc_{0.2}Zr_{1.8}Si_xP_{3-x}O_{12}$ ($0{,}3 \leq x \leq 2{,}8$) untersucht. Der Ersatz von $(PO_4)_{3-}$ durch $(SiO_4)_{4-}$ im System Li_2O-Sc_2O_3-ZrO_2-SiO_2-P_2O_5 senkt effektiv die Sintertemperatur. Darüber hinaus kann die Einführung von Zirkonium die Verdampfung von Lithiumspezies selbst bei hohen Sintertemperaturen begrenzen. Es wurde gezeigt, dass die Silikatsubstitution in $Li_{3+x}Sc_2Si_xP_{3-x}O_{12}$ ($0 \leq x \leq 0{,}6$) die monokline Symmetrie (Raumgruppe P21/n) stabilisiert, was zu einer Erhöhung der Gesamtionenleitfähigkeit führt. Die Ionenleitfähigkeit bei 25 °C stieg von 2×10^{-6} S cm^{-1} für x = 0 auf 1.2×10^{-5} S cm^{-1} für x = 0,15, was die höchste Ionenleitfähigkeit der untersuchten Zusammensetzungen im System Li_2O-Sc_2O_3-ZrO_2-SiO_2-P_2O_5 darstellt. Die Reinheit der NaSICON-Materialien hat einen starken Einfluss auf den Korngrenzenwiderstand und damit auf die Ionenleitfähigkeit.

Ausgewählte keramische NaSICON-Elektrolyte wie $LiZr_2(PO_4)_3$, $Li_{1.2}Y_{0.2}Zr_{1.8}(PO_4)_3$, und Li $LiSc_2(PO_4)_3$ wurden elektrochemisch hinsichtlich ihrer Reduktionsstabilität untersucht und erwiesen sich als stabiler gegenüber Lithium als LATP und LAGP. $Li_3Sc_2(PO_4)_3$ erwies sich als chemisch und elektrochemisch sehr stabil und könnte in Kombination mit Lithiummetall als Anodenschutzmaterial fungieren.

Table of Contents

I Introduction

1.1 Motivation: electrochemical energy storage

The impending depletion of fossil fuel resources, increasing carbon dioxide emissions, climate change, and environmental problems are the predicted home-made problems of mankind. It has been universally recognized that the world is facing energy problems [1]. Solving these problems is becoming increasingly important, and we urgently need to rethink the overall strategy of energy production and consumption. A variety of renewable and clean energy sources have been developed, such as wind, wave and solar power, but these energy sources are not constant; they fluctuate depending on the time, day, and place. The variable nature of these renewable and clean energy sources makes electrical energy storage a must for continuous energy supply [2-4].

Lithium ion batteries (LIBs) are the most successfully developed technology for electrochemical energy storage. With their high energy density and capacity, long cycle life, good performance and no memory effect [5], they are the state of the art for powering a wide range of electronic devices and electric vehicles as well as for storing electricity generated from alternative energy sources. Thanks to continuous research and development efforts, the performance of modern LIBs has improved significantly since their introduction by Sony in 1990 and is approaching the theoretical performance limit [6,7, 8].

All batteries consist of two electrodes, an anode (negative electrode) and a cathode (positive electrode), which are connected by an ionically conductive material (so-called electrolyte) that transports the Li ions between the electrodes [4, 9] (Figure 1.1). An electrolyte is a medium containing mobile ions that provide ionic conductivity but do not conduct electrons.

The active electrode materials in state-of-the-art LIBs are generally Li-intercalation compounds that are capable of reversibly incorporating/releasing Li ions into/from their respective structures, e.g. graphitic carbon as an active anode material (AAM) or layered lithium metal oxides as cathode active materials (CAM). During charging, the Li ions are de-intercalated from the layered oxide compound and intercalated into the graphite layers. The process is reversed during discharging.

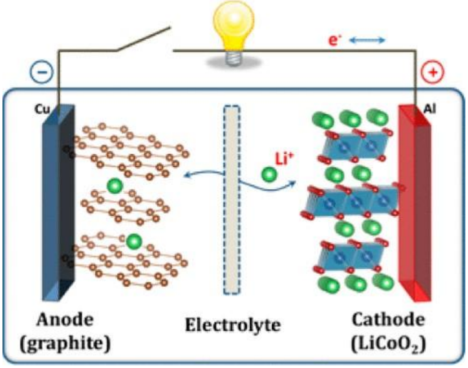

Figure 1.1: Schematic representation of a conventional lithium-ion battery. Reprinted with permission from ref [10]. Copyright 2013 American Chemical Society.

LIBs have established themselves in various markets and application areas, e.g. in consumer electronics, electric vehicles, stationary energy storage systems, etc. [11]. However, the classical LIBs use flammable organic liquid electrolytes. The main drawbacks in this context are the limited operating temperature and safety issues such as leakage risks and corrosion, flammability due to the low thermal stability and low flame point, so that fires and explosions can easily occur. Solid state batteries (SSB) is a battery technology that uses solid electrolytes (SE) instead of liquid electrolytes. SSBs are expected to provide better safety aspects, longer life, no leakage and contamination, high resistance to shock and vibration, and the possibility of easy miniaturization. An overview of SEs is given in the next section.

1.2 Overview of solid electrolytes

Solid electrolyte (SE) is an ionically conducting and electronically insulating solid material. The most important properties of SE for use in SSBs are high ionic conductivity, low electronic conductivity, wide electrochemical stability window, good chemical and electrochemical compatibily with other components, suitable mechanical properties, simple manufaturing processes, low cost, ease of device integration and environmental friendliness. The main classes of SEs currently being considered for use in SSBs are sulfides, polymers, and oxides, each with relative advantages and disadvantages that affect their economic viability.

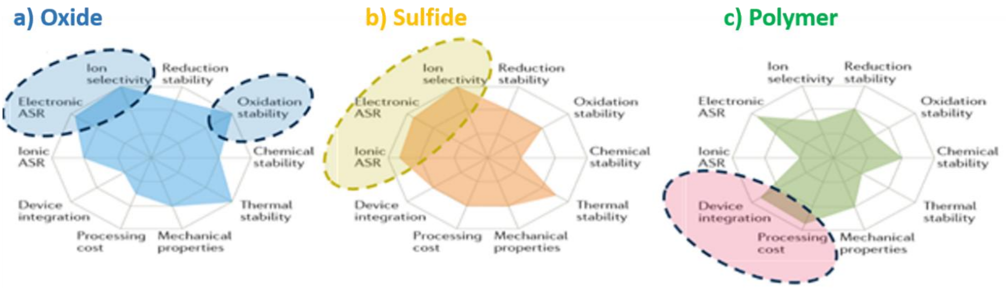

Figure 1.2: Performance properties,(including area-specific resistance, ASR) of different solid electrolyte materials: oxide (blue), sulfide (orange), and polymer (green). [25]. Reprinted with permission, license number: 5342020718198.

Sulfide solid electrolytes:

Sulfide-type SE are closely related to a lithium super ionic conductor (LiSICON)-type solid electrolyte of the γ-Li_3PO_4 type [26, 27]. Due to the much weaker interaction of Li^+ with S^{2-} compared to O^{2-}, sulfide-type SE exhibit higher Li-ion mobility and ionic conductivities than their oxide counterparts [26]. In particular, thio-LiSICON compounds with the composition $Li_{4-x}Ge_{1-x}P_xS_4$ ($0 < x < 1$), which occur as glasses, glass-ceramics and ceramics, have attracted much attention in recent years due to their excellent properties [27, 28]. For example, the ceramic thio-LiSICON $Li_{10}GeP_2S_{12}$ has a very high ionic conductivity of 1.2×10^{-2} S cm^{-1} at 27 °C [28]. The glassy Li_2S-P_2S_5 [26, 29] and glass-ceramic $70Li_2S$-$30P_2S_5$ [30] exhibit high ionic conductivities of 5.4×10^{-5} Scm^{-1} and 3.2×10^{-3} Scm^{-1} at RT, respectively.

Solid sulfide electrolytes have a high ionic conductivity, which is comparable to or higher than that of organic liquid electrolytes. However, the sulfide electrolytes are generally not stable in ambient atmosphere due to reaction with moisture. Several Li_2S-P_2S_5 electrolytes have been investigated with regard to structural changes and H_2S formation upon exposure to air [31]. $67Li_2S$-$33P_2S_5$ glass and Li_2S produced large amounts of H_2S, with strong structural changes. In $67Li_2S$-$33P_2S_5$ glass, the original $P_2S_7^{4-}$ group decomposed into OH and SH groups, and SH further reacted to form OH group and H_2S. In the case of Li_2S crystals, LiOH and H_2S were formed. $75Li_2S$-$25P_2S_5$ glass and glass-ceramic electrolytes showed almost no structural changes and little H_2S formation due to the good chemical stability of PS_4^{3-} group against hydrolysis. For the use of sulfide electrolytes in SSBs, it is therefore necessary to select a suitable chemical composition and to protect the batteries from the ambient atmosphere. On the one hand, sulfide SSEs are promising candidates with desirable advantages such as excellent Li-ion conductivity of more than 1 mS cm^{-1}, sufficient deformability for easy mechanical processing, lower grain boundary resistance, and low processing temperature. On the other hand, this class of materials also has serious drawbacks, such as a very narrow electrochemical stability window and consequently incompatibility with high-voltage CAMs and alkali metal AAMs, sensitivity to the air or moisture, and the need for high pressure during operation to maintain the morphological integrity.

Polymer solid electrolytes:

The advantages of polymer-based SSBs include greater safety, low cost, nontoxicity, flexible shape and ease of fabrication compatible with existing LIB technology [48]. The development of polymer batteries began as early as the 1980s after the discovery of lithium-ion conduction in a system based on poly(ethylene oxide) PEO [32-35]. After this discovery, various lithium-ion conducting polymers such as poly(methyl methacrylate) (PMMA) [36, 37], poly(acrylonitrile) (PAN) [38, 39] and poly(vinylidene fluoride) (PVDF) [40] have been increasingly used for the development of solid-state polymer LIBs. Polymer electrolytes can be divided into three classes: dry solid polymer electrolytes, gel polymer electrolytes and composite polymer electrolytes. Since gel polymers are not in the solid state, they are not described here.

All polymer electrolytes rely on a dissolved Li salt for the ionic conductivity. In dry polymer electrolytes, no liquid is added and the polymer acts as a solid solvent for the lithium ions [41-44]. However, the ionic conductivity of dry polymer systems is very low $<10^{-5}$ S/cm at ambient temperature and 10^{-4} S cm^{-1} at 65-78 °C.

Composite solid polymer electrolytes consist of ionically conductive polymers such as PEOs containing a lithium salt ($LiPF_6$ or $LiAsF_6$) and are often mixed with liquid electrolytes or inorganic oxide nanoparticles (e.g., Al_2O_3, ZrO_2, SiO_2, or TiO_2). Addition of ceramic particles results in a more amorphous polymer matrix by inhibiting chain crystallization and attracting Li from the salt [45-47].

Solid polymer electrolytes are nontoxic and can maintain contact across an electrode/electrolyte interface during battery operation. However, this class of materials also has serious drawbacks, such as a very low ionic conductivity at RT , higher operation temperatures (usually >60°C), a narrow operation temperature range limited by a glass transition temperature, a relatively narrow electrochemical stability window (in particular low oxidation stability and incompatible with high-voltage cathode materials), poor mechanical stability [49, 50], and a low transference number. Although PEO is a cheap polymer already produced on a large scale, the synthesis and scale-up of other polymers different from PEO are still a challenge, and their production costs are very high.

Besides pure solids, quasi-solid-state electrolyte (QSE) also belong to SEs. QSE is a solid-liquid composite material. Ideally, QSE should combine the advantages of individual components and exhibit high ionic conductivity and mechanical strength. However, most quasi-solid electrolytes prepared by immobilizing ionic liquid (IL) or organic liquid electrolyte in inorganic scaffold generally have poor interfacial compatibility and low Li- ion transference number, which limits their application. Sun et. al prepared a QSE (ZIF-8 QSE) based on a zeolitic imidazolate framework-8 (ZIF-8), in which the ZIF-8 has a special cage structure that interacts with the guest electrolyte to form a composite electrolyte with a good ionic conductivity of about 1.05×10^{-4} S cm^{-1}, and a higher transference number of about 0.52. It is worth noting that the ZIF-8-based QSEs exhibit good thermal stability up to 350 °C without thermal runaway, which is significantly higher than that of a conventional organic liquid battery systems.

1.2.1 Oxide electrolytes

The term oxide electrolytes is generally applied to various classes of inorganic materials, including oxides, phosphates and silicates, which can be amorphous, glassy or polycrystalline (ceramic). Oxide electrolytes attract the attention of researchers and engineers due to their relatively high Li-ion conductivity at RT up to a few mS cm^{-1}, nonflammability, high chemical stability, wide electrochemical stability window and in particular high oxidation stability, wide operational temperature range and processability in air [51-53]. The most studied oxide electrolytes are lithium phosphorus oxynitride (LiPON), garnet-type ceramic, i. e. $Li_7La_3Zr_2O_{12}$ (LLZO) [57-59], and perovskite-type $Li_{3x}La_{2/3-x}TiO_3$ [60, 61].

LiPON is a known Li-ion conductor with a high electrochemical stability, but its applications are limited to thin-film batteries due to high costs and relatively low ionic conductivities of around10^{-6} S cm^{-1} [127]. Additionally, perovskite-type $Li_{3x}La_{2/3-x}TiO_3$ is of interest since it shows a significantly higher ionic conductivity of 10^{-3} S cm^{-1} at RT. Unfortunately, this electrolyte is not stable in contact with Li metal due to the reduction of Ti^{4+} to Ti^{3+} [128]. Furthermore, the oxide-based ceramic materials with garnet structure attract a lot of attention since they are stable against a Li metal anode. Cubic LLZO, which was synthesized by Weppner *et al.* [130] in 2007 for the first time, shows ionic conductivity of 3×10^{-4} S cm^{-1} at RT and an activation energy of 0.3 eV. In contrast, a significantly lower conductivity of only 1.63×10^{-6} S cm^{-1} was found for the tetragonal LLZO phase. In recent years a series of dopants and substituents such as Al [126, 131], Ta[132, 133], Ga[61, 134, 135], W[136], and Nb[137, 138] has been investigated to stabilize the cubic LLZO structure at RT and to improve its ionic conductivity. Due to these efforts, the RT ionic conductivity of the state of the art cubic LLZO reached 10^{-3} S cm^{-1} [31, 126, 132-134, 139]. In particular, Ta-substituted LLZO (LLZO: Ta) shows an outstanding performance in terms of a relatively high ionic conductivity of up to 1.2 S cm^{-1} at RT, as well as a good stability towards Li metal and CAMs [122, 140-142]. High ionic and low electronic conductivity, high safety (non-flammability), wide electrochemical window (0 – 5 V), compatibility with Li metal, and inertness to oxygen render garnet-type LLZO one of the most promising SEs for SSBs [126, 132, 143].

In addition to the above-mentioned oxides-type electrolytes, special attention has been paid to LiSICON-type [27, 56] and NaSICON-type [54, 55] phosphate electrolytes because of their structural and thermal stability. Since this work focuses on NaSICON-type electrolytes, this class of materials will be discussed in more detail.

1.2.1.1 Lithium Super Ionic Conductor (LiSICON)

Hong et al. [62] was the first to report a LiSICON-type solid electrolyte $Li_{14}Zn(GeO_4)_4$, which showed ionic conductivity of 1.25×10^{-1} Scm^{-1} at 300 °C. Kuwano et al. [65] prepared new LiSICON-type solid electrolytes $Li_{3+x}Ge_xV_{1-x}O_4$ $(0 < x < 1)$, among which two compositions $Li_{3.5}Ge_{0.5}VO_4$ and $Li_{3.6}Ge_{0.6}V_{0.4}O_4$ revealed high bulk and total ionic conductivities of 4×10^{-5} Scm^{-1} and $\sim 10^{-5}$ Scm^{-1} at 18 °C, respectively.

Hu et al. [66] prepared solid solutions between Li_4SiO_4 and Li_3PO_4, $Li_{4-x}Si_{1-x}P_xO_4$ $(0 < x < 1)$. The highest ionic conductivity of $Li_{3.5}Si_{0.5}P_{0.5}O_4$ and $Li_{3.4}Si_{0.4}P_{0.6}O_4$ was about 10^{-6} Scm^{-1} at RT.

Song et al. [67] partially doped O^{2-} with Cl^{-}, and obtained LiSION-type $Li_{10.42}Si_{1.5}P_{1.5}Cl_{0.08}O_{11.92}$ and $Li_{10.42}Ge_{1.5}P_{1.5}Cl_{0.08}O_{11.92}$ with ionic conductivities of 1.03×10^{-5} Scm^{-1} and 3.7×10^{-5} Scm^{-1} at 27 °C, respectively.

1.2.1.2 Na^+ Super Ionic Conductor (NaSICON)

NaSICON type compounds were originally reported by Hong, Kafalas and Goodenough in 1976 describing the synthesis and characterization of the solid solution $Na_{1+x}Zr_2Si_xP_{3-x}O_{12}$ $(0 \leq x \leq 3)$ with high Na^+ ionic conductivity related to their 3-D open framework [54, 55]. NaSICON structure is not limited to sodium, but is rather a large family of materials with the general formula $AM_2(PO_4)_3$, NaSICON compounds display very attractive compositional diversity and are likely to achieve high conductivity. A variety of substitutions have been reported and are summarized in [70].

The A-site can be occupied by:

- monovalent cations: Li^+, Na^+, K^+, Rb^+, Cs^+, H^+, H_3O^+, NH^{4+}, Cu^+, Ag^+,
- divalent cations: Mg^{2+}, Ca^{2+}, Sr^{2+}, Ba^{2+}, Cu^{2+}, Pb^{2+},Cd^{2+}, Mn^{2+}, Co^{2+}, Ni^{2+}, Zn^{2+},
- trivalent cations: Al^{3+}, Y^{3+}, La^{3+}-Lu^{3+}
- tetravalent cations: Ge^{4+}, Zr^{4+}, Hf^{4+}

The A-site can also be vacant if the M site is occupied by a pentavalent cation.
The M site can be occupied by:

- divalent cations: Cd^{2+}, Mn^{2+}, Co^{2+}, Ni^{2+}, Zn^{2+}
- trivalent cations: Al^{3+}, Ga^{3+}, In^{3+}, Sc^{3+}, Ti^{3+}, V^{3+}, Cr^{3+}, Fe^{3+}, Y^{3+}, La^{3+}-Lu^{3+}
- tetravalent cations: Si^{4+}, Ge^{4+}, Sn^{4+}, Ti^{4+}, Zr^{4+}, Hf^{4+}, V^{4+}, Nb^{4+}, Mo^{4+},
- pentavalent cations: V^{5+}, Nb^{5+}, Ta^{5+}, Sb^{5+}, As^{5+}.

The crystal structure of NaSICON $A_xM_2(PO_4)_3$ is composed of corner-sharing PO_4 tetrahedra and MO_6 octahedra providing a relatively open 3-D network of sites and conduction pathways for various A cations. In general, two main types of cavities are considered, referred to as M1 and M2. The former is a sixfold coordinated site and the latter is an irregular eightfold coordinated site [3].

Taylor et al. [71] replaced sodium with lithium to obtain a new category of solid Li^+ ionic conductors related to the compound LZP. Aono et al. [24] investigated the electrical properties of $Li_{1+x}M_xTi_{2-x}P_3O_{12}$ (M = Al, Cr, Ga, Fe, In, La, Sc and Y) materials and determined a maximum ionic conductivity of 7 × 10^{-4} S cm^{-1} at RT for $Li_{1.3}Al_{0.3}Ti_{1.7}P_3O_{12}$. Similarly, $Li_{1+x}Al_xGe_{2-x}P_3O_{12}$ materials show very high ionic conductivity at RT in a wide stoichiometry range. Kumar et al. [73] and Fu et al. [74] reported that $Li_{1.5}Al_{0.5}Ge_{1.5}P_3O_{12}$ and $Li_{1.4}Al_{0.4}Ge_{0.6}P_3O_{12}$ materials have an ionic conductivity at RT of 10^{-2} S cm^{-1} and 10^{-4} S cm^{-1}, respectively. However, the instability of Ti^{4+} and Ge^{4+} towards reduction to Ti^{2+} and Ge^{2+}, respectively, in direct contact with metallic lithium as an anode still remains a major problem [75], resulting in severe performance degradation and limiting the application of NaSICON-type SSBs with lithium metal anodes [76, 77]. Therefore, there is still a need to develop Ti/Ge-free NaSICON-type Li^+-ion conductors with improved thermodynamic stability, even though such attempts have a long history.

1.2.2 Variety of NaSICON-type solid electrolytes

NaSICON-type $LiM_2P_3O_{12}$ (M = Ti, Zr, Ca ,Sr, Sc, Y, Al) materials are of interest as potential SE in SSBs due to their lithium ion transport performences and high chemical stability in ambient atmosphere. Table 1.2.2 summarizes the ionic conductivities at RT of materials with the composition $Li_{1+x}M_xZr_{2-x}P_3O_{12}$ with M = Sc, Y, Al.

Table 1.2.2: Ionic conductivities at room temperature of materials with the composition $Li_{1+x}M_xZr_{2-x}P_3O_{12}$ with M = Sc, Y, Al.

x	**This work**	**Literature**	
0	5.4 × 10^{-7}	1 × 10^{-10} [12]	
		8.73 × 10^{-7} [79]	
		4.77 × 10^{-7} [80]	
		2 × 10^{-6} [81]	
		1 × 10^{-9} [82]	
		3.3 × 10^{-6} (rh.) [83]	

		1×10^{-11} (mon.) [83]#				
		8.06×10^{-7} [84]				
		1×10^{-5} [84]				
		1.5×10^{-6} [85]				
		6.07×10^{-8} [21]				
	Sc substitution		**Y substitution**		**Al substitution**	
	This work	**Literature**	**This work**	**Literature**	**This work**	**Literature**
0.02				4.8×10^{-6} [86]		
0.05				3.0×10^{-7} [15]		5.8×10^{-7} [80]
0.1				2.3×10^{-5} [87] 2.9×10^{-5} [87]* 7.7×10^{-6} [15]		6.4×10^{-7} [80]
0.15				3.1×10^{-5} [87] 7.1×10^{-5} [87] *		
0.2	2.7×10^{-5}		6.7×10^{-5}	2.3×10^{-5} [87] 6.5×10^{-5} [15]	3.6×10^{-6}	1.9×10^{-6} [80]
0.225						2.1×10^{-6} [80]
0.25						2.1×10^{-6} [80]
0.275						3.1×10^{-6} [80]
0.3						1.9×10^{-6} [80]
0.4	9.7×10^{-6}		4.8×10^{-5}		9.5×10^{-7}	
0.5						9.4×10^{-7} [80]
0.6	8.2×10^{-6}		3.9×10^{-5}		6.8×10^{-7}	2.2×10^{-7} [80]
0.8	7.1×10^{-6}		2.7×10^{-5}		5.2×10^{-9}	
1	8.2×10^{-7}		7.5×10^{-7}		8.3×10^{-11}	4.8×10^{-7} [88] + 3.6×10^{-7} [88] + 3.7×10^{-7} [88] +
	Sc substitution		**Y substitution**		**Al substitution**	
	This work	**Literature**	**This work**	**Literature**	**This work**	**Literature**
1.2	6.5×10^{-6}		1.5×10^{-6}			
1.4	5.6×10^{-6}	3.0×10^{-7} [1]	5.8×10^{-7}			
1.6	2.7×10^{-6}	1.2×10^{-6} [1] 1.6×10^{-5} [9] #	3.2×10^{-7}			
1.8	4.5×10^{-6}	1.1×10^{-5} [1] 2.3×10^{-5} [9] # 2×10^{-6} [10]	4.7×10^{-7}			
1.85		8.9×10^{-6} [1]				
1.9		2.1×10^{-6} [1] 1.1×10^{-5} [9] #				
1.95		6.6×10^{-7} [1]				
1.96		9.1×10^{-9} [9] #				
2	6.5×10^{-7}	1.5×10^{-8} [89]	2.3×10^{-7}			

		8.5×10^{-13} [9] #				
		2×10^{-9} [90] **				
		5.4×10^{-7} [90] ***				
		3×10^{-6} [90] ****				
		3.2×10^{-7} [91]				

#: extrapolated value form high-temperature data, *: Spark-plasma sintering (SPS), **: $Li_3Sc_2(PO_4)_3$ ceramics fabricated without ball-milling of the powder, ***: $Li_3Sc_2(PO_4)_3$ ceramics fabricated with ball-milled powder and sintered at 1200 °C, ****: $Li_3Sc_2(PO_4)_3$ ceramics fabricated with ball-milled powder and sintered at 1400 °C [90]. +: $Li_xAlZr(PO_4)_3$ (x = 1.8, 2.0, 2.2).

1.3 Objective of this thesis

The development of Ti-free and Ge-free Li^+ ionic conductors of the NaSICON-type with improved thermodynamic stability is still required. A general strategy to increase the electrochemical stability is to replace "critical" redox-active ions such as Ti or Ge in the NaSICON structure with redox-inactive ions. Zirconium is the most popular element for this purpose, but the ionic conductivity of Zr-based NaSICONs is far inferior to that of Ti- and Ge-based compounds, and their sintering temperature is usually even higher than that of LATP and LAGP. Therefore, many studies have been conducted to improve the properties of Zr-based NaSICON-SEs by partially replacing Zr^{4+} ions with di- or trivalent cations in the general formula $Li_{1+(4-n)x}M^{n+}{}_xZr^{4+}{}_{2-x}(PO_4)_3$ when M was Sc [29, 30], Y [31, 32], Al [33, 34], Ca [35, 36] and Sr [37, 38] and Fe, Cr, and In [39].

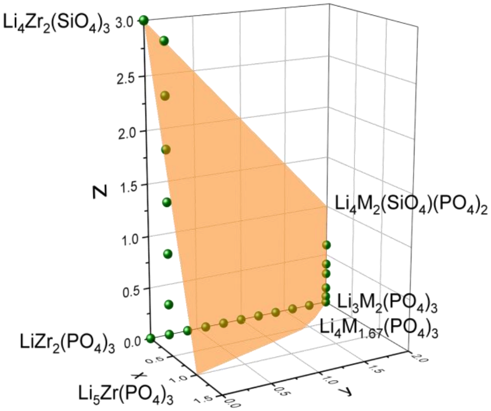

Figure 1.3: Exploratory research of NaSICON materials in the system Li_2O-M_2O_3-ZrO_2-SiO_2-P_2O_5. The orange surface corresponds to the compositional limits of the NaSICON materials according to the formula $Li_{1+4x+y+z}Zr_{2-x-y}M^{3+}{}_y(SiO_4)_z(PO_4)_{3-z}$. The end members at the corners of the orange surface are given as chemical formulas. The green bullets indicate the investigated samples.

In this thesis, we will discuss the materials with cation and polyanionic substitutions in the $Li_{1+x}M^{3+}{}_xZr_{2-x}(SiO_4)_y(PO_4)_{3-y}$ system. In Figure 1.3, the horizontally arranged green spheres with $M^{3+} = Al^{3+}, Sc^{3+}, Y^{3+}$ ($y = 0$) correspond to the materials with cation substitutions. The vertically arranged green spheres with $M^{3+} = Sc^{3+}$ correspond to the materials with polyanionic substitutions.

1.3.1 Partial cation substitutions

The ionic conductivity of LZP has been intensively studied and a wide range of ionic conductivity from 10^{-8} to 10^{-6} S cm^{-1} has been observed depending on the preparation method, final lithium stoichiometry, crystallographic symmetry, densities and microstructures of the sintered pellets [11, 15, 92-95]. The ionic conductivity in NaSICON-type materials can be significantly improved by the partial substitution of tetravalent with trivalent metal cations, which leadsto additional lithium ions in the structure and improves the mobility of the charge carriers [12, 70]. Furthermore, by incorporating elements with different ionic size into the crystal structure of LZP, the size of bottlenecks of lithium transport pathways can be adjusted and the ionic conductivity can be controlled. In this regard, several NaSICON-type materials have already been investigated [11, 12, 15, 80, 81, 87, 88, 93, 94, 96-98].

Mariappan et al. and Li et al. [15, 87] stabilized the rhombohedral structure of LZP at RT by substituting Y^{3+} for Zr^{4+}. The authors studied the electrical properties of the compounds $Li_{1+x}Y_xZr_{2-x}(PO_4)_3$ with $0.1 \leq x \leq 0.2$ [15] and $0.05 \leq x \leq 0.2$ [87], respectively, and obtained a remarkably improved ionic conductivity of 0.7×10^{-4} S cm^{-1} at 25°C [87] for $Li_{1.15}Y_{0.15}Zr_{1.85}(PO_4)_3$ densified by spark plasma sintering. They reported that Y^{3+} is a suitable substitution ion for Zr^{4+} in LZP, leading to an increase in lattice parameters and cell volume due to the different ionic radii of Zr^{4+} (0.72 Å) and Y^{3+} (0.9 Å) [99].

Savitha et al. [88] and Zhang et al. [80] examined the systems $Li_xAlZr(PO_4)_3$ ($x = 1.8, 2.0, 2.2$) and $Li_{1+x}Al_xZr_{2-x}(PO_4)_3$ ($x = 0.2, 0.225, 0.25, 0.275, 0.3, 0.5$), respectively, reaching an ionic conductivity of 4.4×10^{-5} S cm^{-1} for the sample $Li_{2.2}AlZr(PO_4)_3$ at 400 °C [88] and 3.1×10^{-6} S cm^{-1} for $Li_{1.0.275}Al_{0.275}Zr_{1.725}(PO_4)_3$ at RT [80]. Cassel et al. [81] obtained a stable rhombohedral phase with $Li_{1.2}Ca_{0.1}Zr_{1.9}(PO_4)_3$, which showed an increased ionic conductivity at RT of 1.2×10^{-7} S cm^{-1} for the material prepared by solid-state reaction and 7.2×10^{-7} S cm^{-1} for the material prepared by sol-gel method. Also the substitution with Sr was studied and the compound $Li_{1.2}Sr_{0.1}Zr_{1.9}(PO_4)_3$ reached the highest ionic conductivity of 3.4×10^{-5} S cm^{-1} when sol-gel synthesis was used [84]. Furthermore, the latter material was also investigated by Smith et al. [97] using classical solid-state reaction method. Here the total ionic conductivity was 2.1×10^{-5} S cm^{-1} with a relative density of ~97% after hot-pressing.

The ionic conductivity of LSP was reported to be 10^{-7} S cm^{-1} [99]. Amatucci et al. explored the optimization of LSP by substituting $A1^{3+}$ and Y^{3+} for Sc^{3+}. The ionic conductivitis at RT were reported as 1.5 × 10^{-5} S cm^{-1}, 5 × 10^{-6} S cm^{-1} and 5 × 10^{-5} S cm^{-1} for $Li_3Sc_{1.6}Al_{0.4}(PO_4)_3$, $Li_3Sc_{1.5}Y_{0.5}(PO_4)_3$ and $Li_{4.8}Sc_{1.4}(PO_4)_3$, respectively [90]. Furthermore, $Li_{2.8}Sc_{1.8}Zr_{0.2}(PO_4)_3$ has an ionic conductivity of 2 × 10^{-6} S cm^{-1} [99].

Suzuki et al. described the synthesis, structure and ionic conductivity of Li-ion conductors of $Li_{3+2x}(Sc_{1-x}Mg_x)_2(PO_4)_3$, $Li_{3-4x}(Sc_{1-x}M_x)_2(PO_4)_3$ (M = Nb, Ta) [89] and $Li_{3-2x}(Sc_{1-x}M_x)_2(PO_4)_3$ (M = Ti, Zr, Sn, Hf) [89, 100]. Ionic conductivity of members of these solid solutions is summarized in Annex 1.

Sato et al. [101] studied the system $Li_{3-2x}(Sc_{1-x}Zr_x)_2(PO_4)_3$. The highest ionic conductivity of 1.04 × 10^{-3} S cm^{-1} was reported for the sample with $x = 0.05$ at 150 °C, but no value at RT was presented.

The research results of the partial cation substitutions show improvements in ionic conductivity, but the values still cannot meet the requirements for high battery performance. Moreover, the results confirmed that most of the crystal structures for NaSICON materials have rhombohedral symmetry with space group $R\bar{3}c$. Orthorhombic, monoclinic and triclinic symmetry variations appear more rarely, depending on composition, synthesis conditions and temperature. On the one hand, long duration of sintering (up to 10 h) at high temperatures (above 1200 °C) [15] is required to stabilize the rhombohedral phase showing the fast ion conductivity and on the other hand sintering at high temperatures increase the evaporation of lithium species and the occurrence of micro-cracking during cooling from high temperature to RT [104, 105]. Furthermore, the loss of lithium species at high sintering temperature [106] is the reason for intensified pore formation [107]. All these aspects eventually result in ionic conductivity values which cannot meet the high battery performance requirements.

Therefore, there is a strong need to reduce the sintering temperatures of Li-containing NaSICON materials to avoid micro-cracks, limit the lithium evaporation, and achieve high relative density and high ionic conductivity. For that purpose, the next section is the re-investigation of the system $Li_{1+x}M^{3+}_xZr_{2-x}(SiO_4)_y(PO_4)_{3-y}$ ($M^{3+} = Al^{3+}, Sc^{3+}, Y^{3+}$) with a systematic optimization of the sintering conditions to further increase the ionic conductivity of NaSICON materials.

1.3.2 Polyanion partial substitutions

In the polyanionic substitutions two solid solutions were investigated with the aim to reduce the sintering temperature and to increase the ionic conductivity (see Figure 1.3):

a) The series $Li_{3+x}Sc_2Si_xP_{3-x}O_{12}$ with $0 \leq x \leq 0.6$ derived from the parent compound LSP ($x= 0$). Beyond $x = 0.6$ the conductivity is expected to decrease due to the decreasing number of vacancies [54].

b) Partial substitution of P^{5+} by Si^{4+} in the system $Li_{1.2+x}Sc_{0.2}Zr_{1.8}Si_xP_{3-x}O_{12}$ with $0 \leq x \leq 2.8$. The mentioned series is an extension of the exploration in the same system with the cation substitution in the solid solution $Li_{1+x}Sc_xZr_{2-x}P_3O_{12}$. The composition $Li_{1.2}Sc_{0.2}Zr_{1.8}P_3O_{12}$ showed the highest conductivity of 2.7 × 10^{-5} S cm^{-1} within this series.

c) Full anion substitution of P^{5+} with Si^{4+} was considered $Li_4Zr_2Si_3O_{12}$ (LZS) in order to study the chemical stability against lithium metal in comparison with LZP and LSP. To our knowledge, the fully-substituted LZP has received hardly any attention so far and no research has been carried out on this compound and the second series mentioned above.

In addition, this work will provide a broader insight into the properties of NaSICON materials substituted with trivalent ions and re-examined materials using systematic optimization of sintering conditions to further increase the ionic conductivity of NaSICON materials. The thermal, crystallographic, microstructural, and electrical properties of the prepared samples are evaluated and discussed in comparison with previously obtained results.

II Materials and Methods

2.1 Material Synthesis

2.1.1 Powder Synthesis

Powders in Li_2O-M_2O_3-ZrO_2-SiO_2-P_2O_5 system where M = Sc, Al, Y were synthesized by the solution assisted-solid state reaction (SA-SSR) as described elsewhere [110]. Stoichiometric quantities of high purity Li_2CO_3 (Alfa Aesar, 99 %), Sc_2O_3 (Projector GmbH, 99.5 %), Y_2O_3 (Alfa Aesar, 99 %), Al_2O_3 (Alfa Aesar, 99.9 %), ZrO_2 (Saint-Gobain, 99.8 %), SiO_2 (Alfa Aesar, 99.8%) were mixed in a quartz glass beaker using water to obtain a homogeneous aqueous suspension. Additionally, a corresponding amount of $NH_4H_2PO_4$ (Merck KGaA, 99 %) was added during stirring. The whole mixture was stirred overnight with 250 rpm at 70 °C for the slow evaporation of H_2O. The homogenized mixture was first heated up to 100 °C and then the dried solid mixture was calcined in an oven at (500 °C – 900 °C) depending on composition and stoichiometry for 3 hours to form an amorphous raw powder.

2.1.2 Milling

The annealed powder was manually ground in an agate mortar. To reduce the particle size for further processing, the obtained powder was finally milled in a grinding bowl with ethanol as the dispersing medium and with 5 mm ZrO_2 balls using a planetary ball mill (Pulverisette 7 premium line, Fritsch Germany) at 350 rpm for 5 hours before being subsequently dried at 70 °C for 6 h.

2.1.3 Sintering

Sintering is the process of consolidation when all part remain solid mass by pressure and heat treatment which is below the melting point of the material, in this study the sintering temperatures were extracted from the shrinkage curves in the dilatometer and DTA/TG measurements [39-41].

2.1.3.1 Free sintering

The annealed and freshly milled powders were pressed by uniaxial cold pressing into pellet-shaped samples with a pressure of about 150 MPa for two minutes and sintered in Platinum (Pt) crucibles. The sintering was carried out under ambient atmosphere in high temperature chamber furnace.

2.1.3.2 Field-Assisted Sintering Technology/Spark Plasma Sintering (FAST/SPS)

To improve the densification process, a field-assisted sintering, also known as Field-Assisted Sintering Technology /Spark Plasma Sintering (FAST/SPS), was used [114]. By applying mechanical pressure and fast Joule heating, FAST/SPS enables sintering of dense ceramics at lower temperatures with significantly shorter dwell times as compared with conventional free sintering.

FAST/SPS process was performed in a HP D5 FAST/SPS device (FCT System GmbH, Rauenstein, Germany) [115] in vacuum (around 0.6 mbar). Before sintering a graphite foil (SGL Carbon) with a thickness of 0.35 mm was wrapped around the internal diameter of 12 mm of a metallic mold made of molybdenum based alloy TZM (Plansee SE, Austria) fully covering the internal wall. Then, the lower disk punched from graphite foil was inserted into the mold, 2 g of NaSICON powder was filled in and sandwiched by another disk punched from graphite foil. The graphite foil was used to separate the powder sample from the pressing tools as well as to improve the heat transfer and ease removal of the sample from the mold. The FAST/SPS device is equipped with uniaxial hydraulic press (pressing force up to 50 kN) and with a 37 kW power source and can reach a maximum temperature of 2400 °C at a maximum voltage of 8 V. The temperature was controlled by an axial pyrometer, which measured the temperature from the upper punch. In this work, the sintering was performed at temperatures of 1000 °C -1200 °C. A uniaxial pressure of 50 MPa was applied with 0.16 hours dwell time. The heating rate was 600 K/h and slow cooling rate of 120 K/h in order to obtain crack-free samples. After ejection of the samples, the graphite foil was dry polished off from all pellet surfaces by SiC sandpaper. Then all samples were thermally treated in air in a chamber furnace at 900 °C for 4 hours to restore oxygen stoichiometry and remove carbon residues.

2.2 Powder characterization

2.2.1 Elemental analysis

The stoichiometry of the powders was controlled by Inductively Coupled Plasma Optical Emission Spectroscopy (ICP-OES) using a Thermo Scientific iCAP7600 spectrometer with optical scale and CID semi-conductor detector, axial und radial reflection, and wavelengths between 166 nm and 847 nm. 50 mg of powder were mixed with 0.5 g of lithium borate in a platinum crucible and fired for one hour at 1000 °C in a muffle furnace. The liquefied material was dissolved in 30 mL HCl (5%). Afterwards the sample solutions were transferred to sample vials containing 0.5 mL of HF and filled to 50 mL volume. For each composition this measurement was done twice.

2.2.2 Particle size distribution

The particle size distribution (PSD) of the milled powders was verified with a laser scattering particle size analyzer (Horiba LA-950V2 with a 650 nm and a 405 nm laser source). This technique utilizes the diffraction patterns of the laser beam targeted on sample particles and is capable of measuring the particles ranging from nanometers to millimeters in size. The resulting data were analyzed applying the Mie theory [111, 112]. The powders after ball milling have a similar agglomerate morphology. Furthermore, the

PSDs of all powders are nearly identical with a mean particle size of about 1.1 µm. Therefore, any differences in the sintering process are not related to the different particle sizes of the powders.

2.3 Thermal analysis

2.3.1 DTA/TG

Differential thermal analysis / thermogravimetry (DTA/TG) measurements was performed on the calcined powders up to 1600 °C in air with heating and cooling rates of 300 K/h using the simultaneous thermal analyzer STA449F1 Jupiter coupled with the mass spectrometer QMS 403C Aëolos from NETZSCH-Gerätebau GmbH. During TG experiment, the changes in weight are measured depending on temperature and provide data about the thermal stability, the purity and the presence of humidity in a sample.

The DTA analysis records the temperature differences between the sample and a reference while they undergo identical thermal treatments. Indeed, a DTA curve is a plot of the differential temperature against temperature (or time) and the peaks orientation depends on the noticed phenomenon either as exothermic (downwards peak) or endothermic (upwards peak). Many phenomena can be observed with exo- or endothermic signals such as crystal structure change, phase transition, solid state reaction, crystallization, oxidation or reduction are noticed as exothermic signal but melting is noticed as endothermic signal.

2.3.2 Dilatometry

The dilatometry experiments were carried out with a 402C dilatometer also from NETZSCH-Gerätebau GmbH. During the measurement the change in length of the pressed pellets was recorded until a shrinkage of 25 % was reached. Since the shrinkage of the sample is registered during the dilatometry experiment, the data can be used to adapt the sintering conditions for the systematic studies of the grain size and morphology changes [113]. During the sintering experiment, the sample is heated up to a given temperature and the temperature is hold for a given time. $\frac{\Delta L}{L_0}$ is plotted versus the temperature or versus the time during the isothermal period of the thermal program.

2.3.3 Relative density

Correct density measurement is an important characterization for analyzing the sintering property of the samples. Experimental density was determined geometrically according to equation 2

$$\rho_e = \frac{m}{v} \qquad \text{Equation 2}$$

where ρ_e is the experimental density of the sample, m is the mass and v is the volume. The theoretical density ρ_t was obtained from the Rietveld refinement results of the X-ray diffraction (XRD). Finally, the relative density ρ_r was calculated according to equation 3

$$\rho_r = \frac{\rho_e}{\rho_t}$$ Equation 3

2.4 Crystal structure

2.4.1 X-ray diffraction

XRD is a non-destructive analytical technique used to obtain information about the crystallographic properties of the material including phase composition and lattice structure. The incident beam of X-rays is elastically scattered by the electrons of the atoms in a material producing secondary spherical waves. The waves undergoing constructive interference are registered by a detector, as shown in Figure 2.4.a. The criterion for constructive interference is given by Bragg's law (Figure 2.4.b) [116].

$$n\lambda = 2d_{hkl}\sin(\theta)$$ Equation 4

where n is an integer, θ the angle of incidence with the lattice plane and d_{hkl} the distance between lattice planes. Each set of lattice planes can be indexed by an integer triple *hkl*, called the Miller indices, which represent the intersections points of the plane with the unit cell edges. The entire sample surface is scanned when 2θ = 180°, and Bragg's law applies at the points where the scattered waves constructively interfere. By measuring the intensity of scattered waves (reflections) as a function of scattering angle (using a movable detector, Figure. 2.4a), a diffraction pattern is collected. Very strong intensities, known as Bragg peaks, are obtained in the diffraction pattern when the lattice is highly ordered and the scattered waves satisfy the Bragg condition [116].

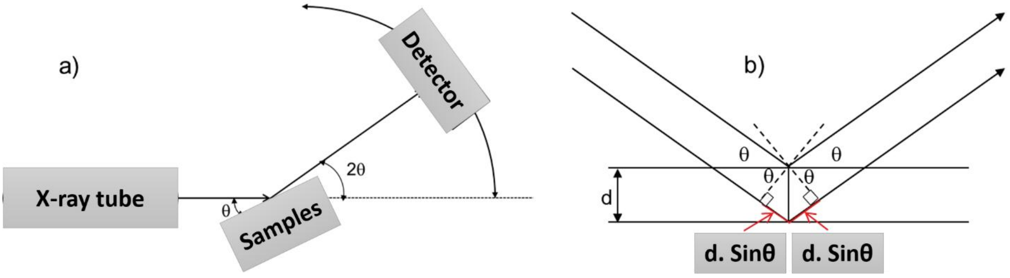

Figure 2.4: Schematic of (a) X-ray diffractometer and (b) Braggs diffraction law [117].

The unit cell information for a given lattice is obtained using the following relationship [118]:

$$\frac{1}{d_{hkl^2}} = (\frac{h}{a} + \frac{k}{b} + \frac{l}{c})^2 \qquad \text{Equation 5}$$

for a cell of any crystalline material. However, it is reduced to

$$\frac{1}{d_{hkl^2}} = \frac{4}{3a^2} \times (h^2 + k^2 + l^2) + \frac{l^2}{c^2} \qquad \text{Equation 6}$$

for a rhombohedral unit cell where $a = b \neq c$ and $\alpha = \beta = 90\,°$ and $\gamma = 120\,°$

$$\frac{1}{d_{hkl^2}} = \frac{h^2}{a^2 sin^2 \beta} + \frac{k^2}{b^2} + \frac{l^2}{c^2 sin^2 \beta} - \frac{2hl\, cos\, \beta}{ac\, sin^2 \beta} \times (1 - cos^2 \beta)^{-1} \qquad \text{Equation 7}$$

for a monoclinic unit cell where $a \neq b \neq c$ and $\alpha = \gamma = 90\,° \neq \beta$

The space group and lattice parameters can be calculated from given set of d-values using equation 6 and 7 for rhombohedral and monoclinic structure, respectively. Despite the fact that these calculations are straightforward for one reflection at a given d-value, the calculation of a complete XRD pattern for polycrystalline material is quite complex and complicated. This is because the XRD pattern of a polycrystalline material is related to other parameters, such as the preferred orientation of crystallographic planes or the overlap of reflections (e.g., from different structures of one or more phases). Indeed, complex algorithms are required to derive the correct space group and unit cell parameters from a complete diffraction pattern. These algorithms have been developed and are used in data analysis in the Jana computer program [119].

The phase purity of the different synthetized powders or sintered pellets was controlled by XRD. The X-ray analyses were carried out with a Bruker D4 Endeavor diffractometer using Cu K_α radiation. A typical measurement was in the range of diffraction angles from $2\theta = 10°$ to $80°$ with a step size of 0.02° and a dwell time of 0.75 s of measurement time per step. The data were analyzed with the program package X'Pert HighScore (PANalytical B.V., version 3.0.5).

2.4.2 Rietveld refinement

The XRD patterns can provide detailed information about the crystal structure, atomic positions, lattice parameters, and site occupancy of atoms within the unit cell when the shape and intensities of the reflections are fitted using the Rietveld refinement method. The method is named after H.M. Rietveld [120, 121], who coordinated mathematical expressions that could be used to generate diffraction patterns similar to that of neutron powder diffraction patterns.

H.M. Rietveld used the following equation to calculate the intensity $I_{c,i}$ at each 2θ step i:

$$I_{c,i} = s \times \sum L_{hkl} \times |F_{hkl}|^2 \times \varphi(2\theta_i - 2\theta_{hkl}) \times P_{hkl} \times A + I_{b,i} \qquad \text{Equation 8}$$

where the second intensity term $I_{b,i}$ is the intensity of the background, while the first term represents the contribution of every Bragg reflection. In each contribution, both the crystal structure (atomic coordinates, thermal displacement and site occupancies) and the diffraction experiment (unit cell, peak profile broadening, etc.) are denoted as follows:

- s, the overall scale factor
- L_{hkl}, containing the Lorentz and polarisation factors as well as a multiplicity factor
- F_{hkl}, the structure factor for the (hkl)th Bragg reflection
- $\varphi(2\theta i\text{-}2\theta hkl)$, a profile function were $2\theta_i$ is the diffraction angle corrected for the 2θ zero error
- P_{hkl}, a preferred orientation function
- A, the absorption factor depending on the instrument geometry [123, 124].

A decade later, the same simulation was performed with XRD diffraction patterns [122]. This is due to the fact that each XRD pattern results from multiple superimposed and overlapped Gaussian peaks as well as a background. In Rietveld refinement, all these peaks are taken into account to fit the XRD pattern using a combination of complex mathematical expressions [123].

With time and technology improvement, the Rietveld refinement has been implemented in several computer programs that significantly reduce the effort required to perform such a refinement. In this work, the crystallographic details of the materials were determined using TOPAS V.4.2 computer software (Bruker AXS 2008, Karlsruhe, Germany). For such refinement, the program requires high-resolution XRD patterns recorded with the same diffractometer as used for routine measurement, but with different parameters: $10\,° \leq 2\theta \leq 140\,°$ with increment of 2θ of 0.01° increment for 2θ and measurement time of 2 s at each step.

2.5 Electrochemical characterization

2.5.1 Electrochemical Impedance Spectroscopy

Electrochemical Impedance Spectroscopy (EIS) is an electrochemical analysis technique that allows to measure the impedance (complex resistance) of a system using AC. It examines the response of the system to a sinusoidal perturbation of the potential (or, less commonly, the current) as a function of frequency. The wide range of frequencies, which can be varied by several orders of magnitude from the mHz to MHz range, provides access to virtually all steps of an electrochemical process, from the slowest to the fastest.

EIS makes it possible to obtain electrical and electrochemical quantitative information (resistance, capacitance, kinetic constants) about charge transfer and charge transport processes at heterogeneous interfaces and in the bulk of electronically or ionically conducting materials, making it a very important technique for characterizing various processes [125, 126].

During the impedance measurement, a sinusoidal signal U_t with small amplitude U_0 is applied to the system electrode/sample/electrode:

$$U_t = U_0 \ sin(\omega t) = U_0 e^{jwt} \ , \ \omega = 2\pi f \qquad \text{Equation 9}$$

where ω is the angular frequency and f is the AC signal frequency.

U_0 should be small enough to obtain a pseudo-linear response of the system. In this case, as in linear systems, the current response to U_t is also a sinusoid with the same frequency but with a phase shift ϕ.

$$I_t = I_0 \, sin(\omega t + \phi) = I_0 \ e^{j(\omega t+\phi)} \qquad \text{Equation 10}$$

where I_0 is the amplitude of the current response.

For pure resistive systems, the frequency-dependent phase shift ϕ is zero [125]. According to Ohm's law, the impedance can be calculated as follows:

$$Z(\omega) = \frac{U_t}{I_t} = \frac{U_0 e^{jwt}}{I_0 e^{j(wt+\phi)}} = |Z| e^{-j\phi} = Z' - jZ'' \qquad \text{Equation 11}$$

where Z' and Z'' are real and imaginary components of the complex impedance [125].

The impedance measurements are performed in a defined frequency range at specific frequency values. For each frequency, the magnitude $|Z|$ and phase ϕ are measured and Z' and Z'' are calculated and plotted against each other in the impedance spectra as a function of frequency. In a Nyquist plot, the imaginary (capacitance) part of the impedance is plotted on the y-axis with the real (resistance) part of the impedance on the x-axis. In such plots, semicircles representing different polarization processes occurring in the electrochemical system are observed. Each semicircle (or each polarization process) can be analyzed as a combination of capacitive and resistive properties. The spectra can be simulated and fitted using an equivalent circuit of capacitors and resistors.

In the Zview® (Scribner Associates Inc) fitting software used to analyze the impedance spectra, a non-ideal capacitance, called constant-phase-element (CPE), can be used to simulate the non-perfect capacitance, e.g. of an electrode/sample interface. The impedance of the *CPE* is calculated as:

$$Z_{CPE} = \frac{1}{(jw)^n \, C_{CPE}} \qquad \text{Equation 12}$$

where ω is the frequency, n is an exponent usually between 1 and 0.5 [127] and C_{CPE} is related to the capacitance C correspondent to :

$$C = R^{\frac{1-n}{n}} \times C_{CPE^{\frac{1}{n}}} \quad [128]$$ Equation 13

If n → 1, then $C_{CPE} \rightarrow C$ and an ideal capacitor is observed. Decreasing n indicates a non-ideal system and n = 0.5 corresponds to a pure diffusion process.

Impedance spectra of polycrystalline materials often consist of two semicircles, each corresponding to a contribution from a particular process (bulk or grain boundary resistance), which in sum gives the total impedance. The semicircle visible at higher frequencies, referred to in this work as the first semicircle, represents the bulk resistance contribution. Bulk resistance, also called grain-interior resistance, is an intrinsic property of a material and depends mainly on its composition and crystal structure. The second semicircle, which is observed at lower frequencies, results from the contribution of the grain boundaries to the total impedance. Grain boundary resistance depends on the material composition, but is greatly affected by the processing conditions and the morphology of the starting powder.

The conductivity of the pellet is calculated from the specific resistance values according to the expression:

$$\sigma_x = \frac{l}{A \times R_x}$$ Equation 14

Where l is the thickness of the measured pellet and A the area of the electrode. Often it is not possible to distinguish between different processes, or the different processes cannot be assigned, so only the total conductivity of the sample is expressed as:

$$\sigma_{TOTAL} = \frac{l}{A \times \sum_x R_x}$$ Equation 15

The activation energy of the ionic conductivity of a material is also determined from impedance data at different temperatures using Arrhenius law:

$$\sigma_T \, T = A \, e^{\frac{-E_a}{kT}}$$ Equation 16

where σ_T is the conductivity at the absolute temperature T, E_a is the activation energy composed of a barrier energy ΔH_b for charge migration and a relaxation energy ΔH_r of the local lattice environment, A is a pre-exponential constant containing the number of charge carriers, jump distance and attempt frequency [129, 130] and k is the Boltzmann constant.

In this work, Impedance Spectroscopy (IS) was used to measure the ionic conductivity of sintered dense pellets of synthesized compounds. For the measurements, blocking gold electrodes were applied on both surfaces of the pellet by sputtering gold for 2 minutes using a Cressington 108 coater, resulting in ~30 nm thick layers. Prior to sputter coating, both sides of the pellet were dry polished using SiC sandpapers to 4000 grit. The measurements were performed at 25 °C and at different temperatures from −40 °C to 100 °C with 20 °C steps in a climate chamber (VT 4002EMC, Vötsch Industrietechnik) using a BioLogic VMP-300 multichannel potentiostat. The frequency was varied from 7 MHz to 1 Hz with an amplitude of 10 mV.

2.5.2 Cyclic voltammetry

Cyclic Voltammetry (CV) is a popular potentiodynamic electrocanalytical technique used in battery research. It provides information on the thermodynamics (redox potential) and kinetics (electron transfer, diffusion rate) of electrochemical reactions [131]. In a CV experiment, the electrode potential is varied linearly at a given scan rate (in mV s^{-1}) in a defined potential range in both forward and reverse direction. The starting potential value is usually chosen before any electrochemical reaction occurs, and the final value is set after the reaction is nearly complete but before any other undesired reaction, e.g. the decomposition of electrolyte, occurs. In cyclic voltammograms the current is plotted against the applied potential. For a reversible redox process in which n electrons are exchanged, the potential is directly related to the concentration of the redox species according to the Nernst equation:

$$E = E^0 - \frac{RT}{nF}\ln\left(\frac{a_{red}^v}{a_{ox}^v}\right) \qquad \text{Equation 17}$$

where E is the applied potential in V, E^0 (V) the standard potential, R is the universal gas constant (8.314 J K^{-1} mol^{-1}), T the temperature in K, F the Faraday constant (9.65 10^4 C mol^{-1}) and n is the amount of electrons exchanged during the redox reaction [131]. a_{ox} and a_{red} are the activities of the oxidized and reduced species, respectively. The standard cell potential is determined by the reduction potentials of the electrode materials E^0 under standard conditions (equation 18).

$$E^0 = E^0_{Cathode} - E^0_{Anode} \qquad \text{Equation 18}$$

Dependence of the current and potential on the scan rates provides information about the kinetics of the electrochemical process. For a kinetically fast system, the peak current is proportional to the square root of the scan rate as described in the Randles–Ševčík equation (equation 19):

$$i_p^a = i_p^c = 2.69 \cdot 10^5 n^{3/2} A D^{1/2} v^{1/2} C \qquad \text{Equation 19}$$

where A is the area of the working electrode in cm^2, D is the diffusion coefficient of the electroactive species in $\mathrm{cm}^2\ \mathrm{s}^{-1}$, v is the scan rate in $\mathrm{V\ s}^{-1}$, and C the concentration of the electroactive species in mol cm^{-3} [131]. In equation 19, the first term corresponds to $0.446 \times F \times \sqrt{\frac{F}{RT}} = 2.69\ 10^5$, where T is the room temperature (298 K).

In this work, the CV measurements were performed using the VMP-300 potentiostat combined with the climate chamber and operated in the potential range from 0 V to 2 V with scan rate of 1 mV s^{-1}. The sample for CV measurements was sandwiched between a lithium metal foil and a thin gold layer. The cell assembly and measurements were performed in an Ar-filled glovebox and then sealed by hot glue to avoid contamination from ambient air. The measurements were carried out in Swagelok cells.

2.6 Scanning electron microscopy

A scanning electron microscope (SEM) produces images of a sample by scanning the surface with a focused beam of electrons. The interaction of the electrons with the sample surface produces different signals that provide information about the morphology and topology, composition and even electrical conductivity. The signals are generated by differently scattered electrons:

- Backscattered electrons (BSE) provide compositional insights. In this mode, the targeted electrons are scattered after an elastic collision. The number of BSE electrons reaching the detector is proportional to the mean atomic number Z. Heavy atoms appear brighter and vice versa. If two materials have identical Z, they produce identical brightness and are therefore indistinguishable.
- The secondary electrons (SE) are generated as ionization products of irradiated atoms by the electron beam. Due to their low energy, SEs can only escape from the atoms at the sample surface (few nm), therefore they are used to determine the surface topography and morphology of the samples. A major limitation is that the image appears brighter when SEs are emitted from the edges of the sample, the so-called “edge effect”. The SEM Ultra55 Zeiss was used in this work to investigate the microstructure of cross-sections of the sintered pellets. Thin platinum layer was sputtered on the surface of the samples before analysis to increase their electrical conductivity.

2.7 Energy dispersive X-ray analysis

Energy dispersive X-ray analysis (EDX) is an analytical technique used for elemental analysis or chemical characterization of a sample. It relies on an interaction between an X-ray excitation source and a sample. When the sample is exited with high-energy electrons in the SEM, characteristic X-rays of the elements are induced. By detecting a spectrum of the emitted X-rays in EDX or the intensity of a specific wavelength in WDX (wavelength dispersive X-ray analysis), the elements in the sample can be detected.

In addition to qualitative analysis performed in this work, quantitative analysis is also possible [129] when a standard material is available for calibration.

The SEM/EDX analysis was carried out using a Zeiss Merlin field emission SEM (Zeiss Microscopy GmbH, Germany) equipped with a windowless X-Max extreme EDX detector (Oxford Instruments, UK). The Oxford instruments AZtec software was used for data acquisition and analysis.

2.8 X-ray photoelectron spectroscopy

X-ray photoelectron spectroscopy (XPS) or ESCA (Electron Spectroscopy for Chemical Analysis) is an important technique for surface characterization [137]. This technique provides a complete elemental analysis (with the exception of hydrogen and helium) and chemical bonding information of the top 10 to 200 Å of any vacuum-stable solid surface (depending on the sample and instrumental conditions). Of all the instrumental techniques currently available for surface analysis, XPS is generally considered to be the most quantitative, the easiest to interpret and the most informative in term of chemical information [138]. XPS characterization was performed using PHI5000 Versa Probe II instrument with monochromatized Al-K_α radiation (1486.6 eV) in collaboration with Justus Liebig University (JLU) Giessen. The samples were either brought in contact with Li metal to investigate their reduction stability, or heat treated at high temperature (1000 °C) under inert atmosphere (Ar). Samples were then sealed in aluminum pouch bags for transfer and opened in an Ar-filled glovebox (H_2O < 0.1 ppm and O_2 < 0.1 ppm) and mounted on an electrically insulating sample holder. This sample holder was then transferred to the XPS chamber via an airtight transfer vessel. A dual beam charge compensation was applied during the measurements. The diameter of the analysis beam was 200 µm and the analyzer pass energy was 23.5 eV. For the Li-contacted sample, Ar-sputtering was applied to the sample surface (2x2 mm area) for depth profiling. The acceleration voltage was 1 kV for the first 6 minutes (3+3 minutes) and 2 kV for the following 16 minutes (8+8 minutes). Casa XPS software was used for data analysis. A linear energy calibration was applied on each spectrum so that the hydrocarbon peak was positioned at 284.8 Ev.

III Solid-state Li^+ ion conductors in the system Li_2O-M_2O_3-ZrO_2-SiO_2-P_2O_5 - Partial cation substitutions in $Li_{1+x}M_xZr_{2-x}P_3O_{12}$ with M = Sc, Y, Al

3.1 Scandium substitutions: $Li_{1+x}Sc_xZr_{2-x}(PO_4)_3$ ($0 \leq x \leq 2$)

For the investigation of the $Li_{1+x}Sc_xZr_{2-x}(PO_4)_3$ series, the substitution of zirconium with scandium was varied from x = 0 to x = 2 with intervals of 0.2. To obtain the optimum sintering condition for each material and dense ceramics of a high quality, the shrinkage behavior of the pellets was characterized by dilatometry (see Annex 2a and Figure 3.4.1a for the material where x = 0.2). The shrinkage was recorded during constant heating until a shrinkage of around 23 % was reached. The pressed pellets were subsequently sintered in the furnace in air at varying temperatures in 10 °C steps between the temperatures defined by 10 % shrinkage (T10%) and 23 % shrinkage (T23%) in the corresponding dilatometry curve. After several sintering tests in the same oven applying the same conditions (3 h, 300 K/h cooling and heating), the optimum sintering temperatures offering the highest relative densities were determined and are listed in Tables 3.1.1 and 3.1.4. No significant shrinkage was obtained below the listed temperatures. Above the listed temperatures, the formation of micro-cracks was observed. For the material where x = 1.6, the sintering experiments were performed only from 900 °C to 985 °C in 10 °C steps, since the pellets melted at about 1000 °C. For samples where x = 2, the sintering experiments were also carried out only from 900 °C to 1000 °C. The dilatometry curve showed expansion starting at about 1000 °C, and sintering at higher temperatures also resulted in the expansion of the pellets and a very low density.

Table 3.1.1: Optimized free sintering temperatures (in °C) for $Li_{1+x}M_xZr_{2-x}(PO_4)_3$ where M = Sc, Y, Al. In all cases, a constant dwell time of 3 h was applied at the given temperatures.

x	M = Sc	M = Y	M = Al
0	1300	1300	1300
0.2	1280	1250	1250
0.4	1250	1250	1100
0.6	1250	1250	1050
0.8	1250	1100	1010
1	1200	980	950
1.2	1230	1000	-
1.4	1250	1000	-
1.6	985	980	-
1.8	1150	980	-
2	1000	980	-

Figure 3.1.1 shows the XRD patterns of $Li_{1+x}Sc_xZr_{2-x}(PO_4)_3$ ($0 \leq x \leq 2$) after sintering at the temperatures listed in Table 3.1.1 The indexing of the reflections in the powder XRD patterns showed that all compositions crystallize with a NaSICON structure. The rhombohedral phase ($R\bar{3}c$; Inorganic Crystal Structure Database (ICSD) no. 191891) [21] was stabilized at RT for the composition where x = 0.2, similar to the substitutions with Ca or Sr in LZP [13, 18]. The diffraction peaks observed for x = 0.2 were assigned to a pure NaSICON structure without any impurity phase. For compositions where $0.4 \leq x \leq 1.4$, the XRD patterns show the presence of a mixture of rhombohedral and monoclinic ($P2_1/n$; ICSD no. 91112) [34] symmetry. Moreover, for the mixture of rhombohedral and monoclinic phases, the orthorhombic phase (*Pbcn;* ICSD no. 83913) [28] appeared in compositions where $1.6 \leq x \leq 2$, which is in good agreement with the previous work by Sato et al. for $Li_{3-2x}Sc_{2-2x}Zr_{2x}(PO_4)_3$ [28]. The contents (in wt.%) of the different phases for all $Li_{1+x}Sc_xZr_{2-x}(PO_4)_3$ compositions are listed in Table 3.1.2 and presented in Figure 3.5.

A significant amount of $Zr_2O(PO_4)_2$ was detected as an impurity in LZP. The formation of $Zr_2O(PO_4)_2$ during the sintering of $Li_{1+x}Sc_xZr_{2-x}(PO_4)_3$ was also observed by Šalkus et al. [24]. Furthermore, in LSP (x = 2) a small amount of unreacted scandium oxide was found. The amount of orthorhombic $Zr_2O(PO_4)_2$ phase (space group *Cmca;* ICSD no. 1922) [35] was refined as 10 wt.% and that of monoclinic Sc_2O_3 phase (space group *C2/m;* ICSD no. 160218) [36] as 4 wt.% according to Rietveld analysis. In Figure 3.1.1, the impurity phase is denoted by an asterisk for $Zr_2O(PO_4)_2$ and by a filled circle for Sc_2O_3.

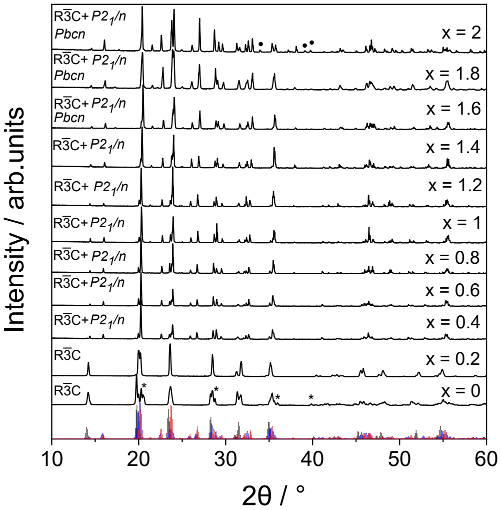

Figure 3.1.1: XRD patterns of LSZP where $0 \leq x \leq 2$ after sintering at optimum conditions (Tables 3.1.1 and 3.1.4). The reference patterns at the bottom are taken from the Inorganic Crystal Structure Database (ICSD), $P2_1/n$; ICSD no. 91112 (blue) [34], *Pbcn*; ICSD no. 83913 (red) [28], $R\bar{3}c$; ICSD no. 191891 (black) [21]. The symbols * and ● indicate $Zr_2O(PO_4)_2$ and Sc_2O_3, respectively.

The lattice parameters and cell volume of $Li_{1+x}Sc_xZr_{2-x}(PO_4)_3$ ($0 \le x \le 2$) obtained by Rietveld refinement and structural literature data of LZP [13] are summarized in Table 3.1.2. The refinements were performed on the basis of space groups given in Table 3.1.2. For better comparison, the lattice parameters and unit cell volume of rhombohedral (space group $R\bar{3}c$) and orthorhombic (space group *Pbcn*) symmetry were converted to monoclinic symmetry (space group $P2_1/n$). These converted data are summarized in Annex 3.

Table 3.1.2: Lattice parameters, unit cell volume, space group, and content of NaSICON polymorphs in $Li_{1+x}Sc_xZr_{2-x}(PO_4)_3$ ($0 \le x \le 2$).

X	Material	a (Å)	b (Å)	c (Å)	β (°)	V (Å³)	Space group	Content (wt.%)
0	$LiZr_2(PO_4)_3$ [13]	8.8600(1)	8.8600(1)	22.065(1)	90	1500.04	$R\bar{3}c$	-
0	$LiZr_2(PO_4)_3$ *	8.808(1)	8.808(1)	22.517(3)	90	1512.85	$R\bar{3}c$	90
0.2	$Li_{1.2}Sc_{0.2}Zr_{1.8}(PO_4)_3$	8.864(2)	8.864(2)	22.120(2)	90	1505.13	$R\bar{3}c$	100
0.4	$Li_{1.4}Sc_{0.4}Zr_{1.6}(PO_4)_3$	8.885(1)	8.885(1)	22.057(3)	90	1507.97	$R\bar{3}c$	58
		8.784(2)	8.967(3)	12.430(2)	91.017	978.89	$P2_1/n$	42
0.6	$Li_{1.6}Sc_{0.6}Zr_{1.4}(PO_4)_3$	8.907(3)	8.907(3)	22.057(1)	90	1515.44	$R\bar{3}c$	54
		8.764(2)	8.974(2)	12.447(3)	91.170	978.73	$P2_1/n$	46
0.8	$Li_{1.8}Sc_{0.8}Zr_{1.2}(PO_4)_3$	8.895(1)	8.895(1)	22.057(1)	90	1511.36	$R\bar{3}c$	52
		8.759(3)	8.977(1)	12.434(3)	91.200	977.46	$P2_1/n$	48
1	$Li_2ScZr(PO_4)_3$	8.839(2)	8.839(2)	22.057(2)	90	1492.39	$R\bar{3}c$	50
		8.750(3)	8.868(3)	12.353(1)	89.937	958.53	$P2_1/n$	50
1.2	$Li_{2.2}Sc_{1.2}Zr_{0.8}(PO_4)_3$	8.834(1)	8.834(1)	22.058(3)	90	1490.77	$R\bar{3}c$	49
		8.749(3)	8.885(2)	12.356(1)	89.862	960.49	$P2_1/n$	51
1.4	$Li_{2.4}Sc_{1.4}Zr_{0.6}(PO_4)_3$	8.839(2)	8.839(2)	22.058(3)	90	1492.46	$R\bar{3}c$	42
		8.776(1)	8.861(3)	12.361(2)	90.011	961.24	$P2_1/n$	58
1.6	$Li_{2.6}Sc_{1.6}Zr_{0.4}(PO_4)_3$	8.846(1)	8.846(1)	22.057(1)	90	1494.76	$R\bar{3}c$	32
		8.789(2)	8.845(1)	12.395(3)	90.040	963.57	$P2_1/n$	62
		12.365(1)	8.785(2)	8.854(1)	90	961.8	*Pbcn*	6
1.8	$Li_{2.8}Sc_{1.8}Zr_{0.2}(PO_4)_3$	8.865(3)	8.865(1)	22.058(3)	90	1501.25	$R\bar{3}c$	14
		8.812(3)	8.845(1)	12.375(2)	89.822	964.53	$P2_1/n$	72
		12.371(2)	8.807(1)	8.841(3)	90	963.2	*Pbcn*	14
2	$Li_3Sc_2(PO_4)_3$ **	8.809(1)	8.809(1)	22.058(2)	90	1482.35	$R\bar{3}c$	7
		8.816(2)	8.851(1)	12.286(1)	90.083	958.68	$P2_1/n$	73
		12.299(1)	8.856(2)	8.807(1)	90	959.3	*Pbcn*	16

*: Contains 10 wt.% $Zr_2O(PO_4)_2$; **: contains 4 wt.% Sc_2O_3

The evolution of the XRD pattern of $Li_{1.2}Sc_{0.2}Zr_{1.8}(PO_4)_3$ after sintering at different stages of heat treatment is shown in Figure 3.1.2. A significant change was observed in the patterns upon increasing the sintering temperature. Initially at 900 °C, the reflection at 2θ = 20.37° was sharper than after sintering at 1000 °C, consisting of one intense reflection with a shoulder at 2θ = 20.04°. At higher temperatures, the reflection started to increase in intensity and at 1250 °C it became a doublet with the same intensity.

Beyond 1250 °C, the two neighboring reflections converged and became a single reflection at 1280 °C. In combination with the vanishing of other reflections, this indicates a phase transition to a higher crystal symmetry. Analysis of XRD patterns from 900 °C to 1200 °C showed that monoclinic symmetry was predominant compared to rhombohedral symmetry. At 1250 °C, the rhombohedral symmetry was dominant, and the Rietveld refinement showed 24 wt.% and 76 wt.% for the monoclinic and rhombohedral phases, respectively. At 1280 °C, the pure rhombohedral phase was stabilized. Kumar et al. [11] also reported the formation of phase mixture in LZP consisting of triclinic $C\bar{1}$ and rhombohedral $R\bar{3}c$ fractions. This phase mixture differs from the result obtained here. The variation of crystallographic symmetry could be influenced by different factors such as the temperature of the heat treatment and also the use of different starting materials. However, as shown in Figure 3.1.2, sintering at 1280 °C can provide the pure rhombohedral NaSICON structure.

In addition, at 900 °C and 1000 °C, the sample contained different amounts of monoclinic ZrP_4O_{12} (space group *C1c1*; ICSD no. 23014) [37] as a secondary phase. However, no impurity was detected at 1200 °C and above.

Rietveld refinement was performed to obtain the lattice parameters, unit cell volume, and crystallographic density (d_X) of $Li_{1.2}Sc_{0.2}Zr_{1.8}(PO_4)_3$ during phase evolution. The results of the refinement are presented in Table 3.1.3. The increase in the sintering temperature of the investigated compound leads to a small increase of the unit cell volume up to 1250 °C, while the phase transition at 1280 °C leads to a significant expansion of the crystal lattice.

Table 3.1.3: Unit cell parameters and space group of $Li_{1.2}Sc_{0.2}Zr_{1.8}(PO_4)_3$ after sintering at different temperatures.

Temp. / °C	**a (Å)**	**b (Å)**	**c (Å)**	**β (°)**	**V (Å^3)**	**V/Z (Å^3)**	**Space group**	**Density (g/cm^3)**
900	8.910(1)	8.910(2)	22.057(1)	90	1516.47	252.7	$R\bar{3}c$	3.26
	8.806(4)	8.934(5)	12.360(3)	89.901(3)	972.40	243.1	$P2_1/n$	
1000	8.877(3)	8.877(1)	22.061(2)	90	1505.53	250.9	$R\bar{3}c$	3.24
	8.816(2)	8.932(1)	12.373(1)	89.907(1)	974.31	243.6	$P2_1/n$	
1200	8.861(1)	8.861(3)	22.065(2)	90	1500.38	250.1	$R\bar{3}c$	3.23
	8.818(2)	8.935(1)	12.373(1)	90.015(2)	974.85	243.7	$P2_1/n$	
1250	8.848(1)	8.848(2)	22.114(1)	90	1499.0	249.8	$R\bar{3}c$	3.23
	8.817(1)	8.935(2)	12.374(1)	90.018(1)	974.82	243.7	$P2_1/n$	
1280	8.864(2)	8.864(2)	22.120(2)	90	1505.13	250.8	$R\bar{3}c$	3.09

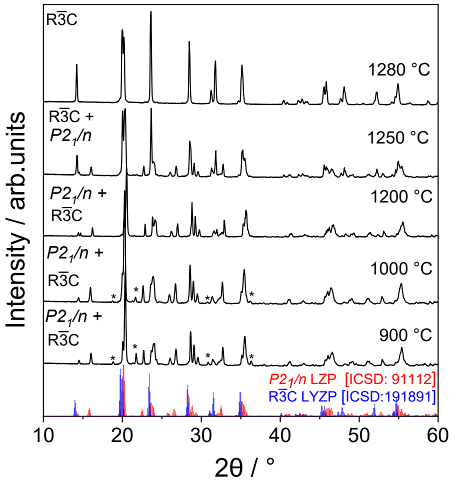

Figure 3.1.2: Phase evolution of $Li_{1.2}Sc_{0.2}Zr_{1.8}(PO_4)_3$ after sintering at different temperatures from 900 ° C to 1280 °C. *: ZrP_4O_{12}.

To study the impact of scandium substitution on ionic conductivity for zirconium in $Li_{1+x}Sc_xZr_{2-x}(PO_4)_3$, impedance spectra were measured at 25 °C. The Nyquist plots of the spectra are shown in Figure 3.1.3. A single semicircle is obtained in the complex impedance plots for all samples at high frequencies, which begins at the origin, with the exception of the LZP and LSP samples. The straight line at low frequencies is due to the ion-blocking electrode polarization. This is attributed to the accumulation of the mobile charge carriers at the electrolyte/electrode interface, indicating that the material is an ionic conductor [38]. The separation of grain and grain boundary resistance from the impedance spectra of $Li_{1+x}Sc_xZr_{2-x}(PO_4)_3$ samples is therefore not possible. Mariappan et al. and Wolfenstine et al. have investigated the impedance properties of Y-doped and Sr-doped LZP, respectively [12,39], and reported that the deconvolution of grain and grain boundary resistances for these materials is not feasible. The radius of the semicircle represents the increase of resistivity with increasing x. However, this trend is not evident for the unsubstituted sample LZP.

The impedance data were fitted using the given equivalent circuit, as shown in Figure 3.1.3. The scandium substitution generates a decrease in the total resistance and improves the ionic conductivity until $x = 0.2$ (see Table 3.1.4). With scandium substitution in LZP, the total ionic conductivity at 25 °C increases from 5.4×10^{-7} S cm^{-1} for the unsubstituted LZP to 2.7×10^{-5} S cm^{-1} for $Li_{1.2}Sc_{0.2}Zr_{1.8}(PO_4)_3$, showing the highest ionic conductivity in the $Li_{1+x}Sc_xZr_{2-x}(PO_4)_3$ series and exhibiting a higher ionic conductivity compared to reported values (Figure 3.1.4 and Table 1.2).

As x increases further (x > 0.2), ionic conductivity decreases continuously. However, at 25 °C, all scandium-substituted materials show ionic conductivity many times higher than that of pure LZP [10, 34, 40]. Even the LSP exhibits a high ionic conductivity of 6.5×10^{-7} S cm^{-1} at RT.

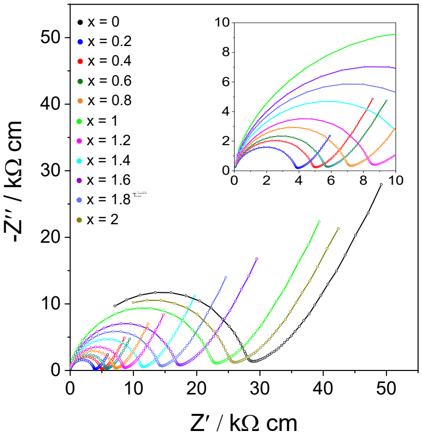

Figure 3.1.3: Nyquist plot of impedance spectra at 25 °C of $Li_{1+x}Sc_xZr_{2-x}(PO_4)_3$ where $0 \le x \le 2$ after accounting for the sample dimensions. The equivalent circuit is also shown.

Table 3.1.4: Free sintering temperature and time, relative density, and ionic conductivity at 25 °C for $Li_{1+x}Sc_xZr_{2-x}(PO_4)_3$ ($0 \le x \le 2$).

x	**Material**	**Sintering temperature (°C) and dwell time (h)**	**Relative density (%)**	**σ $_{25\,°C}$ (S cm^{-1})**
0	$LiZr_2(PO_4)_3$	1300 / 3	88	5.4×10^{-7}
0.2	$Li_{1.2}Sc_{0.2}Zr_{1.8}(PO_4)_3$	1280 / 3	85	2.7×10^{-5}
0.4	$Li_{1.4}Sc_{0.4}Zr_{1.6}(PO_4)_3$	1250 / 3	90	9.7×10^{-6}
0.6	$Li_{1.6}Sc_{0.6}Zr_{1.4}(PO_4)_3$	1250 / 3	98	8.2×10^{-6}
0.8	$Li_{1.8}Sc_{0.8}Zr_{1.2}(PO_4)_3$	1250 / 3	98	7.1×10^{-6}
1	$Li_2ScZr(PO_4)_3$	1200 / 3	97	8.2×10^{-7}
1.2	$Li_{2.2}Sc_{1.2}Zr_{0.8}(PO_4)_3$	1230 / 3	96	6.5×10^{-6}
1.4	$Li_{2.4}Sc_{1.4}Zr_{0.6}(PO_4)_3$	1250 / 3	94	5.6×10^{-6}
1.6	$Li_{2.6}Sc_{1.6}Zr_{0.4}(PO_4)_3$	985 / 3	90	2.7×10^{-6}
1.8	$Li_{2.8}Sc_{1.8}Zr_{0.2}(PO_4)_3$	1150 / 3	91	4.5×10^{-6}
2	$Li_3Sc_2(PO_4)_3$	1000 / 3	87	6.5×10^{-7}

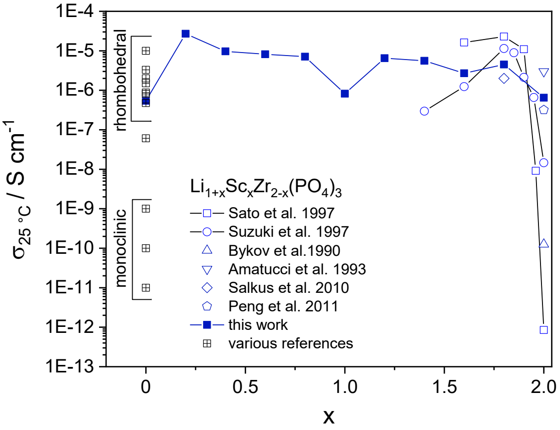

Figure 3.1.4: Variation of the total conductivity of $Li_{1+x}Sc_xZr_{2-x}(PO_4)_3$ as a function of x. The ionic conductivity of $LiZr_2(PO_4)_3$ (crossed squares) can be divided up into the dimorphic nature of the material. The literature data are listed in Table 1.2.

Figure 3.1.4 gives an overview of the variation of the total ionic conductivity at 25 °C of $Li_{1+x}Sc_xZr_{2-x}(PO_4)_3$ where $0 \leq x \leq 2$. It also contains a literature review of different compositions where x= 0 [20, 22, 34, 39, 41-45], x = 2 [25, 46, 47], x = 1.8 [24], $1.6 \leq x \leq 2$ [28], and $1.4 \leq x \leq 2$ [26]. In this work, at 25 °C, the highest ionic conductivity of this series was observed for the material where x = 0.2 (2.7×10^{-5} S cm^{-1}). This high value of ionic conductivity could not be associated with densification, since the relative density of this material after one-step sintering was only 85 %. However, the density was improved with a two-step sintering approach, as described in Section 3.4. The purity of the material could explain this high value of ionic conductivity, as it is the only material in the series that was indexed as a pure rhombohedral NaSICON phase without any trace of other impurities. In contrast, the $Li_2ScZr(PO_4)_3$ material with a higher relative density (97%) was obtained using the one-step sintering process, but yielded poor ionic conductivity (8.2×10^{-7} S cm^{-1}) at 25 °C. Although XRD analysis (Figure 3.1.1) clearly showed the presence of a mixture of rhombohedral and monoclinic phases for $0.4 \leq x \leq 1.4$ and rhombohedral, monoclinic, and orthorhombic phases for $1.6 \leq x \leq 2$, their conductivities are higher. Therefore, the low conductivity of $Li_2ScZr(PO_4)_3$ can be considered as a local minimum along the series. As previously reported, the $Li_{1+x}Sc_xZr_{2-x}(PO_4)_3$ materials where $1.6 < x < 2$ show similar conductivities: higher than the data of Šalkus et al. (x = 1.8; 2×10^{-6} S cm^{-1}) [24], but lower than the values reported by Suzuki et al. [26] and Sato et al. [28]. On the one hand, the lower reported values of ionic conductivity could be related to a low relative density, which was reported to be only 70 %, while 91 % was obtained in this work. On the other hand, the higher reported ionic conductivity could be explained by the better homogeneity and the absence of polymorphism in contrast to the $Li_{1+x}Sc_xZr_{2-x}(PO_4)_3$ material investigated here.

For the end members LZP (x = 0) and LSP (x = 2), the conductivities at 25 °C vary by about seven orders of magnitude. This strong scatter is largely dependent on the quality and thermal history of the materials and can be explained by the following reasons: a) Depending on the heat treatment and processing (e.g. quenching), the rhombohedral high-temperature phase can be stabilized below room temperature. This is well known for LZP [34, 43]. In turn, crystal symmetry strongly affects the ionic conductivity [42, 43]. b) Heat treatment and processing also affect the relative density, and there are many examples where conductivity decreases exponentially with increasing porosity. c) The final stoichiometry of the material is very important, especially for the end members, since small deviations of charge carriers (or vacancies at the other extreme) of only 1-2 % can lead to conductivity changes by several orders of magnitude [48, 49].

3.2 Yttrium substitutions: $Li_{1+x}Y_xZr_{2-x}(PO_4)_3$ ($0 \leq x \leq 2$)

Yttrium was substituted for zirconium in $Li_{1+x}Y_xZr_{2-x}(PO_4)_3$ in a stepwise manner from x = 0 to x = 2. According to the shrinkage behavior of the $Li_{1+x}Y_xZr_{2-x}(PO_4)_3$ pellets (see Annex 2b and Figure 3.4.1a for the material where x = 0.2) recorded with dilatometry, the pressed pellets were sintered at different temperatures. The sintering experiments in the furnace were again carried out between $T_{10\%}$ and $T_{23\%}$ in steps of 10 °C in air. The optimal sintering temperatures leading to the highest relative densities are listed in Tables 3.1.1 and 3.2.3 For materials where $x \geq 1$, sintering experiments were performed only from 900 °C to 1000 °C, as dilatometry measurements showed volume expansion starting at around 1010 °C, and sintering experiments in the furnace led to deformation and partial melting.

Figure 3.2.1 shows the reflections in the powder XRD patterns of $Li_{1+x}Y_xZr_{2-x}(PO_4)_3$ after sintering at optimum sintering conditions (Tables 3.1.1 and 3.2.3). The reflections observed for the sample where x = 0.2 were assigned to a pure and well-crystallized rhombohedral ($R\overline{3}c$) NaSICON structure. $Li_{1+x}Y_xZr_{2-x}(PO_4)_3$ where x = 0.4 crystallized as a mixed rhombohedral ($R\overline{3}c$) and orthorhombic (*Pbcn*) NaSICON structure. The materials where $0.6 \leq x \leq 1.6$ contained the polymorph with the orthorhombic symmetry (*Pbcn*). Furthermore, tetragonal YPO_4 (space group $I4_1/amd$; ICSD no. 201131) [50] was detected as a secondary phase for $0.4 \leq x \leq 1.6$, as also observed by Li et al. [21]. Starting from x = 0.8, but especially at x = 1.8 and x = 2, YPO_4 appeared as a predominant phase with 95 wt.% and 93 wt.%, respectively. Moreover, small amounts (2-7 wt.%) of orthorhombic Li_3PO_4 (space group *Pcmn*; ICSD no.20208) [51] were detected as an impurity in the YPO_4. Li_3PO_4 is easily formed during the synthesis of $LiZr_2(PO_4)_3$, as described in [21]. The content of rhombohedral and orthorhombic NaSICON phases as well as YPO_4 at different Y^{3+} substitution levels from $x = 0.2$ to $x = 1.6$ are summarized in Table 3.2.1 and presented in Figure 3.5.b.

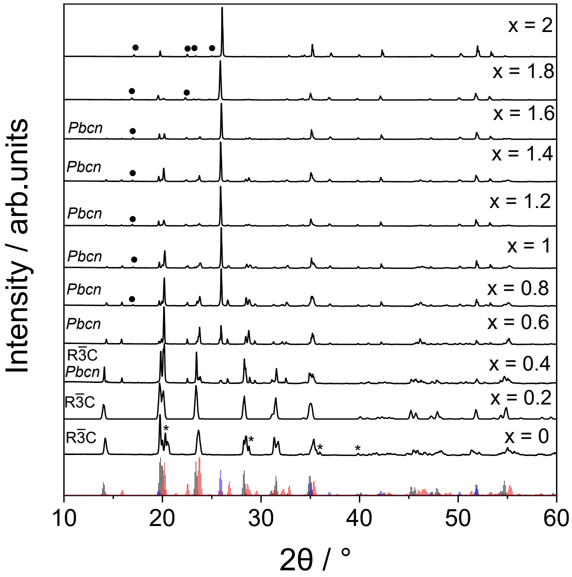

Figure 3.2.1: XRD patterns of $Li_{1+x}Y_xZr_{2-x}(PO_4)_3$ where $0 \le x \le 2$ after sintering at optimum conditions (Tables 3.1.1 and 3.2.3). The reference patterns of LYZP are taken from the inorganic crystal structure database (ICSD), $R\bar{3}c$; ICSD no. 191891(black) [21], *Pbcn*; ICSD no. 83913 (red) [28], YPO_4 (*$I4_1/amd$*), ICSD no. 201131 (blue) [50]. The symbols * and ● indicate $Zr_2O(PO_4)_2$ and Li_3PO_4, respectively.

Table 3.2.1: Lattices parameters, unit cell volume, and space group of LYZP where ($0.2 \le x \le 1.6$).

x	**Material**	**a (Å)**	**b (Å)**	**c (Å)**	**V (Å^3)**	**Space group**	**Content (wt.%)**	**Content YPO_4 (wt.%)**
0.2	$Li_{1.2}Y_{0.2}Zr_{1.8}(PO_4)_3$	8.872(2)	8.872(2)	22.221(1)	1514.74	$R\bar{3}c$	100	0
0.4	$Li_{1.4}Y_{0.4}Zr_{1.6}(PO_4)_3$	8.869(3)	8.869(3)	22.14(1)	1508.20	$R\bar{3}c$	61	6
		8.829(9)	12.438(5)	8.948(9)	982.67	*Pbcn*	33	
0.6	$Li_{1.6}Y_{0.6}Zr_{1.4}(PO_4)_3$	8.831(3)	12.41(1)	8.951(1)	981.99	*Pbcn*	85	15
0.8	$Li_{1.8}Y_{0.8}Zr_{1.2}(PO_4)_3$*	8.819(1)	12.41(3)	8.921(2)	976.35	*Pbcn*	26	72
1	$Li_2YZr(PO_4)_3$*	8.804(2)	12.372(1)	8.903(2)	969.74	*Pbcn*	30	68
1.2	$Li_{2.2}Y_{1.2}Zr_{0.8}(PO_4)_3$*	8.888(3)	12.355(1)	8.818(3)	968.31	*Pbcn*	35	63
1.4	$Li_{2.4}Y_{1.4}Zr_{0.6}(PO_4)_3$*	8.886(2)	12.344(3)	8.820(3)	967.45	*Pbcn*	37	61
1.6	$Li_{2.6}Y_{1.6}Zr_{0.4}(PO_4)_3$*	8.882(3)	12.30(3)	8.830(2)	964.66	*Pbcn*	38	59

*: Contains 2-7 wt.% Li_3PO_4

The XRD patterns of $Li_{1.2}Y_{0.2}Zr_{1.8}(PO_4)_3$ from 900 °C to 1200 °C show the presence of a phase mixture of rhombohedral and monoclinic symmetry. At temperatures from 900 °C to 1200 °C, the intensity of reflections associated with the rhombohedral phase increased significantly, and most importantly, at 1250 °C, the material displayed a phase change to pure rhombohedral symmetry. At 1280 °C, in addition to the rhombohedral symmetry, very small reflections of the monoclinic phase were again observed in the pattern (Figure 3.2.2).

Rietveld refinement revealed rhombohedral and monoclinic phase ratios of 40/50 wt.%, 60/40 wt.%, and 80/20 wt.% at 900 °C, 1100 °C, and 1200 °C, respectively. Furthermore, at 900 °C, 2 wt.% of unreacted P_2O_5 with space group $R\bar{3}c$ (ICSD no. 16610) [52] and 8 wt.% of tetragonal YPO_4 were detected as secondary phases. At 1280 °C, 20 wt.% of tetragonal ZrO_2 with space group $P4_2/nmc$ (ICSD no. 97004) [53] was detected.

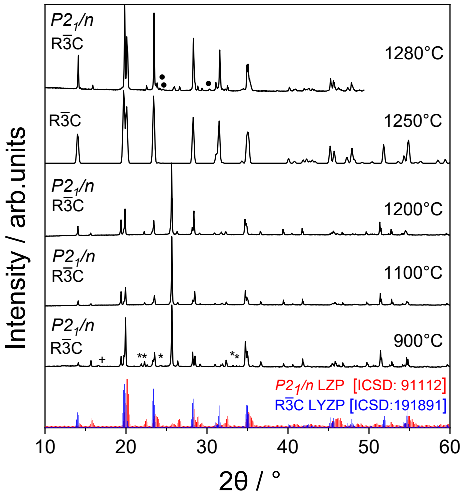

Figure 3.2.2: Phase evolution of $Li_{1.2}Y_{0.2}Zr_{1.8}(PO_4)_3$ after sintering at different temperatures from 900 °C to 1280 °C. The symbols +, *, and ● indicate P_2O_5, YPO_4, and ZrO_2, respectively.

Table 3.2.2: Unit cell parameters and space group of the $Li_{1.2}Y_{0.2}Zr_{1.8}(PO_4)_3$ after sintering at different temperatures.

Temp. / °C	a (Å)	b (Å)	c (Å)	β (°)	V (Å^3)	Space group
900	8.869(1)	8.869(1)	22.134(2)	90	1507.79	$R\bar{3}c$
	8.876(2)	8.944(1)	12.468(3)	89.903	989.8	*P21n*
1000	8.872(1)	8.872(1)	22.157(2)	90	1510.37	$R\bar{3}c$
	8.857(2)	8.941(1)	12.475(1)	89.902	987.8	*P21n*
1200	8.883(2)	8.883(2)	22.148(1)	90	1513.51	$R\bar{3}c$
	8.861(1)	8.919(1)	12.475(3)	89.801	985.9	$P2_1n$
1250	8.872(2)	8.872(2)	22.221(1)	90	1514.74	$R\bar{3}c$
1280	8.885(3)	8.885(3)	22.181(1)	90	1516.44	$R\bar{3}c$

The impact of substituting yttrium for zirconium in $Li_{1+x}Y_xZr_{2-x}(PO_4)_3$ on ionic conductivity was also investigated by impedance spectroscopy at 25 °C. The Nyquist plots of the impedance spectra are shown in Figure 3.7. Here, only the compositions where $0 \leq x \leq 1$ are shown due to the increasing content of YPO_4 in the phase mixture that disproves the conductivity data. Again, only one depressed semicircle is obtained at high frequencies starting at zero, except for the compositions $x = 0$ and $x = 1$ whose depressed semicircles did not begin at the origin.

The radius of the semicircle increases with increasing yttrium substitution level from $x = 0.2$ to $x = 1$.

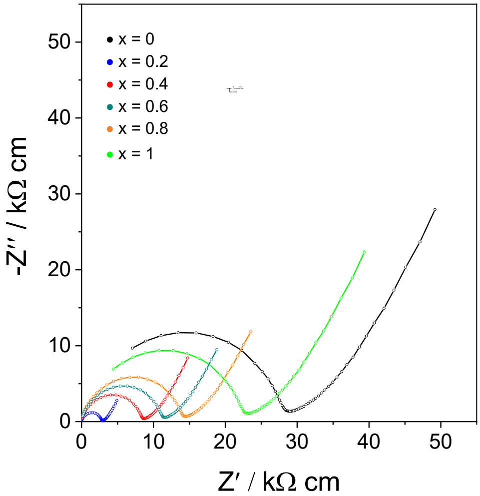

Figure 3.2.3: Nyquist plot of impedance spectra at 25 °C of $Li_{1+x}Y_xZr_{2-x}(PO_4)_3$ where $0 \leq x \leq 1$ after accounting for the sample dimensions. The equivalent circuit is also shown.

The resistance was obtained by fitting the impedance spectra using the given equivalent circuit in Figure 3.2.3. The total conductivity σ_t of the samples was calculated using Equation 14 and the values are listed in Table 3.2.3. Initially, the yttrium substitution in $Li_{1+x}Y_xZr_{2-x}(PO_4)_3$ leads to an increase in ionic conductivity. The total ionic conductivity at 25 °C increases from 5.4×10^{-7} S cm^{-1} for LZP to 6.7×10^{-5} S cm^{-1} for $Li_{1.2}Y_{0.2}Zr_{1.8}(PO_4)_3$ as the highest ionic conductivity in the $Li_{1+x}Y_xZr_{2-x}(PO_4)_3$ series and exhibits a higher ionic conductivity in comparison to the reported values for the same stoichiometry [12, 21], as listed in Table 1.2 and shown in Figure 3.2.4. The maximum value of ionic conductivity for $Li_{1.2}Y_{0.2}Zr_{1.8}(PO_4)_3$ is comparable to that of a similar material ($x = 0.15$) sintered by spark plasma sintering (SPS), displaying a conductivity value of 7.1×10^{-5} S cm^{-1}. The influence of the different sintering process is discussed in section 3.4.

As x increases further ($x > 0.2$), the ionic conductivity decreases continuously with a sharp decline at $x = 1$, which is attributed to the rhombohedral → orthorhombic phase transition and the increasing amount of

YPO_4 phase, which was also reported elsewhere [21]. However, at 25 °C, all yttrium-containing materials show an ionic conductivity several times higher than that of LZP [10, 34, 40].

Table 3.2.3: Free sintering temperature and time, relative density, and ionic conductivity at 25 °C for $Li_{1+x}Y_xZr_{2-x}(PO_4)_3$ ($0 \leq x \leq 1$).

x	Material	Sintering temperature (°C) and dwell time (h)	Relative density (%)	$\sigma_{25\,°C}$ (S cm^{-1})
0	$LiZr_2(PO_4)_3$	1300 / 3	88	5.4×10^{-7}
0.2	$Li_{1.2}Y_{0.2}Zr_{1.8}(PO_4)_3$	1250 / 3	89	6.7×10^{-5}
0.4	$Li_{1.4}Y_{0.4}Zr_{1.6}(PO_4)_3$	1250 / 3	94	4.8×10^{-5}
0.6	$Li_{1.6}Y_{0.6}Zr_{1.4}(PO_4)_3$	1250 / 3	94	3.9×10^{-5}
0.8	$Li_{1.8}Y_{0.8}Zr_{1.2}(PO_4)_3$	1100 / 3	91	2.7×10^{-5}
1	$Li_2YZr(PO_4)_3$	980 / 3	89	7.5×10^{-7}

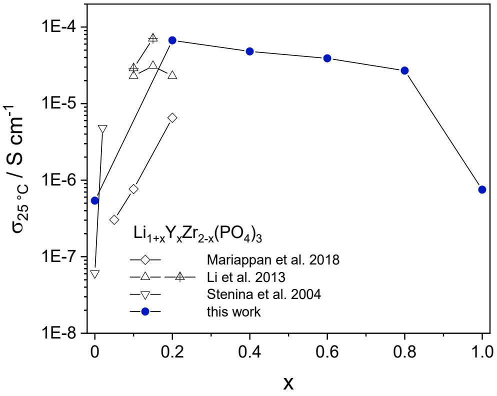

Figure 3.2.4: Variation of total conductivity of $Li_{1+x}Y_xZr_{2-x}(PO_4)_3$ as a function of x. The crossed triangles denote the samples densified by spark plasma sintering. The literature data are listed in Table 1.2. For the ionic conductivity data of $LiZr_2(PO_4)_3$, see Figure 3.2.1.

3.3 Aluminum substitutions: $Li_{1+x}Al_xZr_{2-x}(PO_4)_3$ ($0 \leq x \leq 1$)

Aluminum was substituted for zirconium in $Li_{1+x}Al_xZr_{2-x}(PO_4)_3$ from x = 0 to x = 1. According to the shrinkage behavior of the $Li_{1+x}Al_xZr_{2-x}(PO_4)_3$ pellets (see Annex 2c and Figure 3.4.1a for the material where x = 0.2) recorded with dilatometry, the pressed pellets were sintered at different temperatures between $T_{10\%}$ and $T_{23\%}$ in steps of 10 °C in air. The optimal sintering temperatures leading to the highest relative densities are listed in Tables 3.1.1 and 3.2.3. For the material where x = 1, the sintering experiments were performed only from 900 °C to 950 °C; higher sintering temperatures resulted in melting.

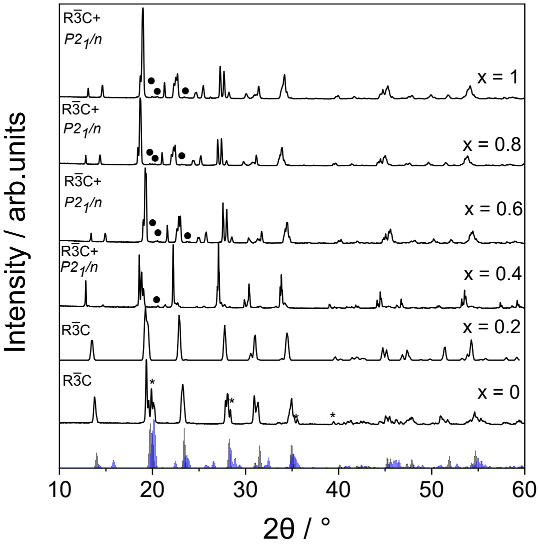

Figure 3.3.1: XRD patterns of $Li_{1+x}Al_xZr_{2-x}(PO_4)_3$ where $0 \leq x \leq 1$ after sintering at optimum conditions (Tables 3.1.1 and 3.3.3). The symbols * and ● indicate $Zr_2O(PO_4)_2$ and $AlPO_4$, respectively. For the reference patterns at the bottom, see Figure 3.1.1.

The XRD patterns of $Li_{1+x}Al_xZr_{2-x}(PO_4)_3$ are shown in Figure 3.9. For x > 0.2, all compositions were identified as a phase mixture of rhombohedral and monoclinic symmetry. Impurity peaks can be observed in materials where $x \geq 0.4$ and were attributed to trigonal $AlPO_4$ with space group $P3_12_1$ (ICSD no. 33746) [54]. The impurity peaks increase in intensity with increasing Al^{3+} substitution. This could be related to the limited solubility and the low sintering temperatures, since the materials where x = 0.6, 0.8, and 1 have melting points of 1070 °C, 1032 °C, and 965 °C, respectively.

Table 3.3.1: Lattices parameters, unit cell volume, and space group of $Li_{1+x}Al_xZr_{2-x}(PO_4)_3$ where $0.2 \leq x \leq 1$.

x	**Material**	**a (Å)**	**b (Å)**	**c (Å)**	**β (°)**	**V (Å^3)**	**Space group**	**Content (wt.%)**
0.2	$Li_{1.2}Al_{0.2}Zr_{1.8}(PO_4)_3$	8.858(1)	8.858(1)	22.140(1)	90	1504.46	$R\bar{3}c$	98
0.4	$Li_{1.4}Al_{0.4}Zr_{1.6}(PO_4)_3$	8.841(2)	8.841(2)	22.081(3)	90	1494.69	$R\bar{3}c$	82
		8.803(1)	8.929(3)	12.379(1)	89.801	973.01	$P2_1/n$	15
0.6	$Li_{1.6}Al_{0.6}Zr_{1.4}(PO_4)_3$	8.831(1)	8.831(1)	22.072(2)	90	1490.71	$R\bar{3}c$	71
		8.804(2)	8.897(1)	12.419(2)	89.974	972.68	$P2_1/n$	25
0.8	$Li_{1.8}Al_{0.8}Zr_{1.2}(PO_4)_3$	8.831(2)	8.831(2)	22.071(1)	90	1490.64	$R\bar{3}c$	60
		8.810(1)	8.872(2)	12.391(2)	90.015	968.51	$P2_1/n$	35
1	$Li_2AlZr(PO_4)$	8.831(2)	8.831(2)	22.070(1)	90	1490.57	$R\bar{3}c$	53
		8.807(1)	8.869(1)	12.388(1)	89.987	967.62	$P2_1/n$	42

The unit cell volumes shown in Table 3.3.1 decrease with increasing x in $Li_{1+x}Al_xZr_{2-x}(PO_4)_3$ ($0 \leq x \leq 1$). Since the ionic radius of Al^{3+} is much smaller than that of Zr^{4+}, this trend is anticipated. While the rhombohedral lattice parameters almost remain constant where x ≥ 0.6, indicating the solubility limit of Al^{3+} in the lattice, the monoclinic lattice parameters continue to decrease slightly. This result is in good agreement with reported data [22]. For comparison, the rhombohedral lattice parameters and unit cell volume were converted to monoclinic symmetry (space group $P2_1/n$) for all $Li_{1+x}Al_xZr_{2-x}(PO_4)_3$ compositions. The data are summarized in Annex 5.

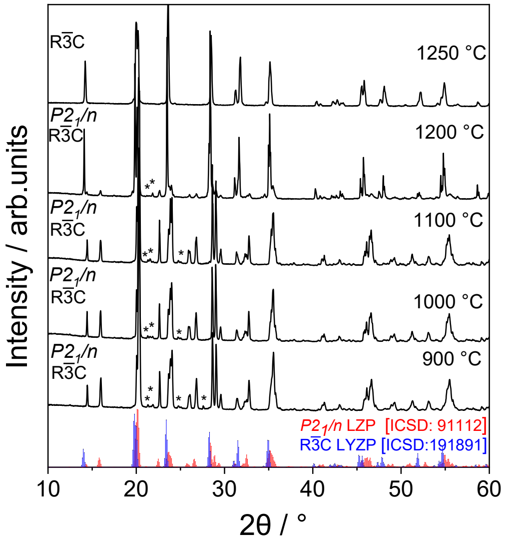

Figure 3.3.2: Phase evolution of $Li_{1.2}Al_{0.2}Zr_{1.8}(PO_4)_3$ after different sintering temperatures from 900 ° C to 1250 °C. *: $AlPO_4$.

The XRD patterns of $Li_{1.2}Al_{0.2}Zr_{1.8}(PO_4)_3$ from 900 °C to 1250 °C is shown in Figure 3.10 and clearly show the presence of a mixture of phases with rhombohedral and monoclinic symmetry up to 1200 °C. As the temperature increased, the intensity of the reflections of the rhombohedral phase increased significantly, and at 1250 °C the rhombohedral phase stabilized. The lattice parameters obtained after Rietveld refinement are listed in Table 3.3.2. Furthermore, trigonal $AlPO_4$ was detected as a secondary phase from 900 °C to 1200 °C. This secondary phase formation was also reported by Amatucci et al. for $Li_3Sc_{2-x}Al_x(PO_4)_3$ [25].

Table 3.3.2: Unit cell parameters and space group of $Li_{1.2}Al_{0.2}Zr_{1.8}(PO_4)_3$ after sintering at different temperatures.

Temperature /°C	a (Å)	b (Å)	c (Å)	β (°)	V (Å^3)	Space group
900	8.947(3)	8.947(3)	22.140(1)	90	1534.84	$R\bar{3}c$
	8.792(1)	8.892(1)	12.324(1)	89.801	963.47	$P2_1/n$
1000	8.974(3)	8.974(3)	22.140(2)	90	1544.12	$R\bar{3}c$
	8.791(1)	8.888(1)	12.328(1)	89.801	963.24	$P2_1/n$
1100	8.887(1)	8.887(1)	22.140(2)	90	1514.32	$R\bar{3}c$
	8.801(1)	8.886(2)	12.338(1)	89.801	964.90	$P2_1/n$
1200	8.855(1)	8.855(1)	22.140(1)	90	1503.44	$R\bar{3}c$
	8.817(2)	8.870(1)	12.475(1)	90.009	975.63	$P2_1/n$
1250	8.858(1)	8.858(1)	22.140(1)	90	1504.46	$R\bar{3}c$

The resistance was obtained by fitting the impedance spectra (Figure 3.3.3) using the given equivalent circuit. The total conductivity σ_t of the samples is compiled in Table 3.3.3.

Figure 3.3.4 provides an overview of the evolution of total ionic conductivity at 25 °C for LAZP where $0 \leq x \leq 1$. In addition, literature data of total ionic conductivity (at 30 °C) of different compositions between x = 0 and x = 0.5 are included [22]. Electrical characterization of the series revealed a maximum conductivity of 3.7×10^{-6} S cm^{-1} for the sample where x = 0.2. Further Al substitution resulted in a steady decrease in ionic conductivity to 8.3×10^{-11} S cm^{-1} for x = 1. At first sight, the evolution of ionic conductivity is related to the phase purity of the samples: $Li_{1+x}Al_xZr_{2-x}(PO_4)_3$ where x = 0.2 is the only material in the series crystallizing as a pure rhombohedral NaSICON phase, whereas the materials where $0.4 \leq x \leq 1$ clearly showed the presence of a mixture of rhombohedral and monoclinic phases (Figure 3.3.1). Indeed, the substitution of Al for Zr in LZP can stabilize the structure to rhombohedral NaSICON at room temperature and increase the ionic conductivity until x = 0.2. Any further Al substitution resulted in phase mixture and decreasing lattice parameters, which have an adverse influence on ionic conductivity.

The results obtained in this study are slightly higher than the reported values [55] presented in Figure 3.3.4. The ionic conductivity of $Li_{1.2}Al_{0.2}Zr_{1.8}(PO_4)_3$ is higher not only in comparison with the same reported material but also with the material where x = 0.275, which gives a maximum total ionic conductivity of 3.1×10^{-6} S cm^{-1} in [22].

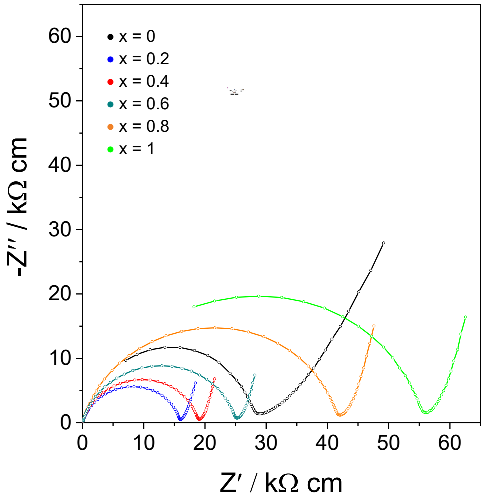

Figure 3.3.3: Nyquist plot of impedance spectra at 25 °C for $Li_{1+x}Al_xZr_{2-x}(PO_4)_3$ where $0 \leq x \leq 1$ after accounting for the sample dimensions. The equivalent circuit used for the fitting is shown in the inset.

Table 3.3.3: Sintering temperature and time, relative density, and ionic conductivity at 25 °C for $Li_{1+x}Al_xZr_{2-x}(PO_4)_3$ $(0 \leq x \leq 1)$.

x	**Material**	**Sintering temperature (°C) and dwell time (h)**	**Relative density / %**	**$\sigma_{25\,°C}$ (S cm^{-1})**
0	$LiZr_2(PO_4)_3$	1300 / 3	88	5.4×10^{-7}
0.2	$Li_{1.2}Al_{0.2}Zr_{1.8}(PO_4)_3$	1250 / 3	94	3.7×10^{-6}
0.4	$Li_{1.4}Al_{0.4}Zr_{1.6}(PO_4)_3$	1100 / 3	92	9.5×10^{-7}
0.6	$Li_{1.6}Al_{0.6}Zr_{1.4}(PO_4)_3$	1050 / 3	91	6.8×10^{-7}
0.8	$Li_{1.8}Al_{0.8}Zr_{1.2}(PO_4)_3$	1010 / 3	90	5.2×10^{-9}
1	$Li_2AlZr(PO_4)_3$	950 / 3	87	8.3×10^{-11}

3.4 Optimizing the sintering conditions of $Li_{1.2}M_{0.2}Zr_{1.8}(PO_4)_3$ (M = Sc, Y, Al)

3.4.1 Two-step sintering

The compositions where x = 0.2 in the $Li_{1+x}M_xZr_{2-x}P_3O_{12}$ system (M = Al, Sc, Y) showed the highest ionic conductivity for scandium, yttrium, and aluminum substitutions. Therefore, the three compounds with the compositions $Li_{1.2}Sc_{0.2}Zr_{1.8}(PO_4)_3$, $Li_{1.2}Y_{0.2}Zr_{1.8}(PO_4)_3$, and $Li_{1.2}Al_{0.2}Zr_{1.8}(PO_4)_3$ were selected to optimize the sintering conditions, to improve the densification, and to increase the ionic conductivity.

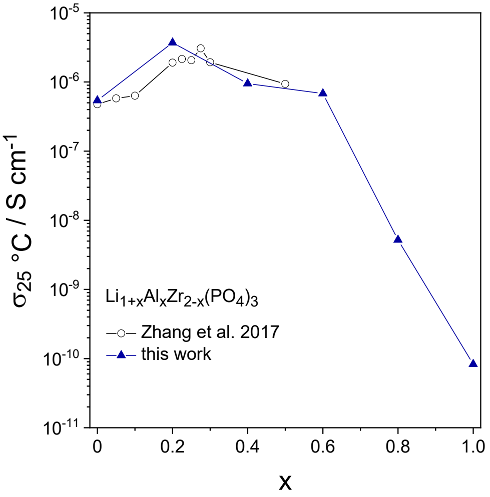

Figure 3.3.4: Variation of total conductivity of $Li_{1+x}Al_xZr_{2-x}(PO_4)_3$ as a function of x. The literature data are listed in Table 1.2.2. For ionic conductivity data of $LiZr_2(PO_4)_3$, see Figure 3.5.

As described above, the shrinkage behavior of the aforementioned compositions was recorded with dilatometry to identify the optimal sintering temperature. The shrinkage was measured during constant heating until a shrinkage of ~23 % was reached. The shrinkage curves of the three compounds are shown in Figure 3.4.1 a. The pellet of $Li_{1.2}Al_{0.2}Zr_{1.8}(PO_4)_3$ shows several shrinkage steps during the sintering process up to 1100 °C, and no further shrinkage is observed up to 1400 °C. The sample of $Li_{1.2}Sc_{0.2}Zr_{1.8}(PO_4)_3$ shrinks continuously starting from 650 °C, followed by higher shrinkage rates at 1350 °C and 1550 °C, and ending at 18% shrinkage. In the case of $Li_{1.2}Y_{0.2}Zr_{1.8}(PO_4)_3$, a two-stage shrinkage behavior is observed. The pellet shrinks sharply between 800 °C and 1200 °C with up to 18% shrinkage. After a temperature interval without further shrinkage, a second shrinkage starts at about 1400 °C. To reach the optimal sintering conditions for the three compositions, a series of sintering treatments was carried out from 1000 °C to 1300 °C with 10 °C intervals for 3 hours in air (not shown here), for which shrinkage was 7-12 % and 11-18 %, respectively. Whereas sintering at low temperature resulted in high porosity and low conductivity, sintering at high temperature led to the formation of cracks and lithium evaporation. Furthermore, optimizing the sintering conditions with two-step sintering slightly enhanced the relative density of the sintered pellets of the three materials (Table 11). Such sintering processes have already been used in the past for solid state electrolyte [56-58].

The resulting densities of the different heat treatments are shown in Figure 3.4.1b. Pellets of $Li_{1.2}Sc_{0.2}Zr_{1.8}(PO_4)_3$ were first exposed to 1280 °C for a short time (0.25 h), followed by annealing at a reduced temperature (980 °C) for a prolonged period of time (3 h). The relative density increased from

82% at 1280 °C/3 h (one-step sintering) to 94% for the two-step sintering protocol (1280 °C/0.25 h and then at 980 °C/3 h). In the case of $Li_{1.2}Y_{0.2}Zr_{1.8}(PO_4)_3$, the two-step sintering method also resulted in a significant increase of relative density from 89 % at 1250 °C/3 h (one-step sintering) to 95% after 1250 °C/0.25 h and then at 980 °C/4 h (two-step sintering). The improvement of the relative density of $Li_{1.2}Al_{0.2}Zr_{1.8}(PO_4)_3$ was not as successful compared to the other two materials. Here, the relative density increased from 94% at 1100 °C/3 h (one-step sintering) to 96% at 1100 °C/0.25 h and then at 980 °C/3 h (two-step sintering).

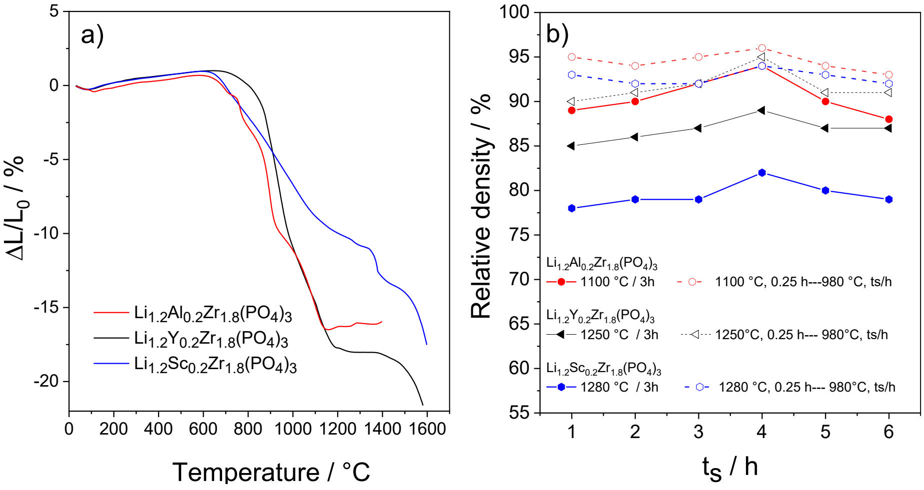

Figure 3.4.1: a) Free sintering curves of $Li_{1.2}Sc_{0.2}Zr_{1.8}(PO_4)_3$, $Li_{1.2}Y_{0.2}Zr_{1.8}(PO_4)_3$, and $Li_{1.2}Al_{0.2}Zr_{1.8}(PO_4)_3$ samples up to 1600 °C. b) Relative densities obtained after sintering under different sintering conditions. Filled symbols: one-step sintering; open symbols: two-step sintering.

The two-step sintering method resulted in reproducible relative densities of > 90 % for all three compositions. This sintering procedure not only increased the density of the specimens, but also reduced the loss of lithium oxide as the samples remained at a high temperature for only a short period of time.

3.4.2 FAST/SPS

The two-step sintering process was very helpful in optimizing the sintering conditions and improving the densification process, but the dwell time is a parameter that needs to be improved further. Therefore, to reduce the dwell time as well as the sintering temperatures, the three selected materials were sintered by high-pressure FAST/SPS for 0.17 hours at temperatures of 1200 °C, 1150 °C, and 1050 °C for $Li_{1.2}Sc_{0.2}Zr_{1.8}(PO_4)_3$, $Li_{1.2}Y_{0.2}Zr_{1.8}(PO_4)_3$, and $Li_{1.2}Al_{0.2}Zr_{1.8}(PO_4)_3$, respectively. As a result, higher relative densities were obtained compared to the one-step sintering procedure but not as high as in the two-step sintering process. The relative densities of materials sintered by one-step sintering, two-step sintering, and FAST/SPS are listed in Table 3.3.3. The two-step sintering method presents a simple alternative compared with FAST/SPS technology, which is a complex fabrication route and therefore industrially less viable [59]. Table 3.3.3 also shows that the ionic conductivity was improved for the three compositions due to the increased relative density.

Table 3.4.2: Comparison of relative densities and ionic conductivity for the $Li_{1.2}M_{0.2}Zr_{1.8}(PO_4)_3$ materials (M = Al, Sc, Y) using different sintering processes.

Material	**Sintering process**	**Sintering temperature (°C) and dwell time (h)**	**Relative density (%)**	**$\sigma_{25\,°C}$ (S cm^{-1})**
$Li_{1.2}Sc_{0.2}Zr_{1.8}(PO_4)_3$	One- step-sintering	1280 / 3	85	2.7×10^{-5}
	Two-step sintering	1280 / 0.25 + 980 / 3	94	4.8×10^{-5}
	FAST/SPS	1200 / 0.17	92	3.4×10^{-5}
$Li_{1.2}Y_{0.2}Zr_{1.8}(PO_4)_3$	One- step-sintering	1250 / 3	89	6.7×10^{-5}
	Two-step sintering	1250 / 0.25 + 980 / 3	95	7.3×10^{-5}
	FAST/SPS	1150 / 0.17	94	7.0×10^{-5}
$Li_{1.2}Al_{0.2}Zr_{1.8}(PO_4)_3$	One- step-sintering	1250 / 3	94	3.7×10^{-6}
	Two-step sintering	1250 / 0.25 + 980 / 3	96	7.1×10^{-6}
	FAST/SPS	1050 / 0.17	95	4.5×10^{-6}

Figure 3.4.2 shows SEM images of fracture surfaces of sintered pellets of $Li_{1.2}M_{0.2}Zr_{1.8}(PO_4)_3$ where M = Al, Sc, Y after sintering by one-step sintering, two-step sintering, and FAST/SPS. In terms of the homogeneity of the materials, the SEM images show that the two-step sintering process gives the best results of the three samples compared to the other two sintering processes. The two-step sintering process resulted in low porosity and an almost crack-free microstructure without areas of partial melting. In comparison, the one-step sintering process leads to crack formation in all samples due to stronger grain growth, while FAST/SPS enhances the partial melting of materials where M = Sc, Y, although this is not pronounced in the case of M = Al. The SEM analyses provided the following observations: a) Sintering at high temperatures for a long time in the furnace using the one-step sintering resulted in the formation of pores and micro-cracks, which can be related to the evaporation of Li_2O and accelerated grain growth, respectively. Weight loss related to the evaporation of Li_2O was observed by DTA/TG measurements (not shown here) in the range of 1250 °C to 1300°C. b) The formation of micro-cracks is minimized by the two-step sintering because the sample remains at a high temperature for only a short period of time. c) Partial melting after the FAST/SPS process, as observed predominantly in materials where M = Sc, Y, can be associated with the high temperatures applied, while this phenomenon is far less visible for M = Al because of the lower sintering temperature (Table 3.4.2). Therefore, a lower sintering temperature

leads to compact materials and high densification, as shown in the SEM images for M = Al by two-step sintering and FAST/SPS.

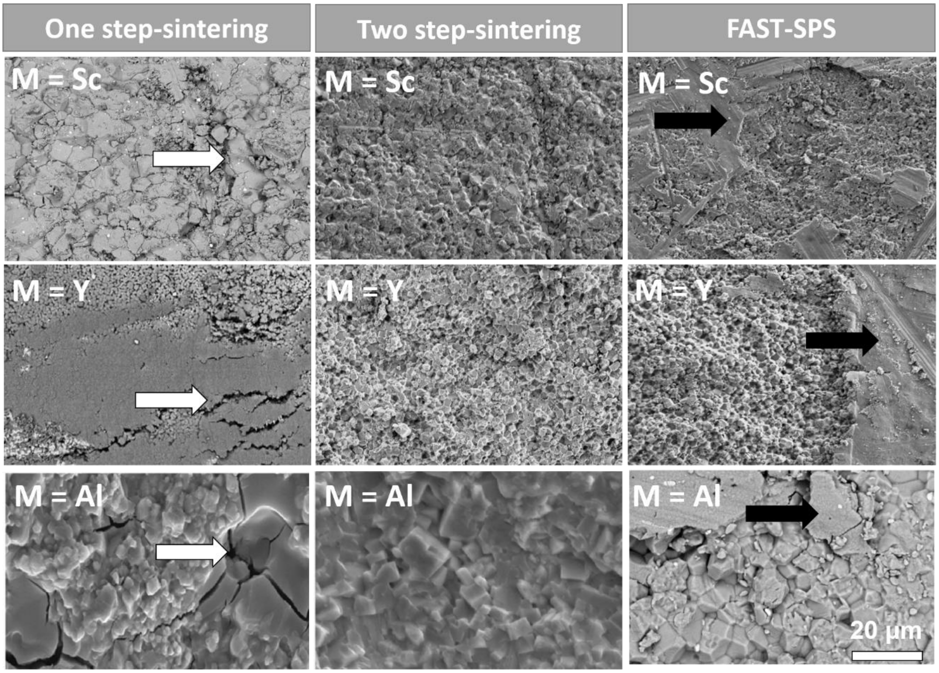

Figure 3.4.2: SEM images showing the microstructure of $Li_{1.2}M_{0.2}Zr_{1.8}(PO_4)_3$ (M = Al, Sc, Y) after sintering at different temperatures and dwell times (Table 3.3.3). The white arrows indicate the micro-cracks and the black arrows show the areas with partial melting.

3.4.3 Discussion of the substitution-dependent chemistry

The evolution of the refined content of the rhombohedral, monoclinic, and orthorhombic NaSICON phases and the unit cell volumes as a function of x in $Li_{1+x}M_xZr_{2-x}P_3O_{12}$ (M = Al, Sc, Y) is depicted in Figure 3.5. For better comparison of the unit cell volumes among the different space groups, the crystallographic data of rhombohedral and orthorhombic phases were converted to the monoclinic cell volume.

The substitution of Zr^{4+} with Sc^{3+} in $Li_{1+x}Sc_xZr_{2-x}(PO_4)_3$ ($0 \leq x \leq 2$) stabilized the pure rhombohedral phase at RT for the composition x = 0.2. Compositions where $0.4 \leq x \leq 1.4$ have a mixture of phases with rhombohedral and monoclinic symmetry. The rhombohedral phase content decreases while the monoclinic modification increases with the substitution of Sc^{3+} until both phases have an equal content at x = 1. In addition to these two phases, the orthorhombic phase appears in compositions where $1.6 \leq x \leq 2$ and increases with the Sc^{3+} substitution. The contents (in wt.%) of the different phases for this series of compositions are listed in Table 3.1.2 and presented in Figure 3.5a. The evolution of rhombohedral ($0 \leq x \leq 2$), orthorhombic ($1.6 \leq x \leq 2$), and monoclinic unit cell volumes ($0.4 \leq x \leq 2$) generally decreases with increasing x in $Li_{1+x}Sc_xZr_{2-x}(PO_4)_3$. Since Sc^{3+} (0.745Å) and Zr^{4+} (0.72Å) have similar ionic radii [60], the differences in the unit cell volume of the $Li_{1+x}Sc_xZr_{2-x}(PO_4)_3$ series (Figure 3.5b) are mainly caused by the difference in the Li^+ concentration in the formula unit. For the compositions x = 1.6, 1.8, and 2, the difference between the monoclinic and orthorhombic phases is only a slight twist of the unit cell. Since the monoclinic and orthorhombic phases are crystallographically very similar and have almost the same unit cell volume as the rhombohedral phase at x = 1.8 and 2, the resulting compounds can be considered to be a single phase with different short- and long-range distortions leading to multiple diffraction peaks in the XRD patterns. These results are consistent with previous work [28]. More crystallographic data can be found in Annex 3.

The substitution of Zr^{4+} with Y^{3+} in $Li_{1+x}Y_xZr_{2-x}(PO_4)_3$ causes a decrease of the orthorhombic and rhombohedral unit cell volumes (except for x = 0.6, Figure 3.5d). This trend cannot be caused by the different radii of Y^{3+} and Zr^{4+} ions, as the ionic radius of Y^{3+} (0.9 Å) is significantly larger than that of Zr^{4+} (0.72 Å) [60]. Rhombohedral lattice parameters in [21] are in accordance with the measured values. The previously mentioned substitution stabilized the pure rhombohedral phase at RT for the composition x = 0.2, showing the highest ionic conductivity value in this series. The further substitution of Y^{3+} first leads to a mixture of rhombohedral and orthorhombic phases (x = 0.4) and then to a pronounced formation of YPO_4 ($0.6 \leq x \leq 2$), resulting in lower ionic conductivity. From Figure 3.5c, it can be deduced that the solubility limit of Y^{3+} is about x = 0.3. The decrease in ionic conductivity depends firstly on the crystallographic results, i.e. the constricted orthorhombic unit cell volume of the materials where $0.4 \leq x \leq 1.6$, and secondly on the increasing impurity of the materials. The occurrence of both phenomena indicates the extraction of Y and P from the NaSICON phase, leading to different NaSICON compositions than expected. As an example, assuming the complete separation of Y from the NaSICON phase, the $Li_2YZr(PO_4)_3$ compound splits into YPO_4 and $Li_2Zr(PO_4)_2$. Rewriting the latter composition as $Li_3Zr_{1.5}(PO_4)_3$, it can be assumed that NaSICON compositions such as $Li_{2.5}[Zr_{1.5}Li_{0.5}](PO_4)_3$ are formed in which Li^+ ions occupy Zr^{4+} sites, indicated in Figure 1.1.3 as the region behind the orange area in the x-y plane. This aberrant NaSICON formation also explains the decreasing unit cell volumes.

Substituting Zr^{4+} with Al^{3+} in $Li_{1+x}Al_xZr_{2-x}P_3O_{12}$ ($0 \leq x \leq 1$) also stabilizes the rhombohedral NaSICON structure at RT for the composition where x = 0.2 and decreases the unit cell volume with increasing Al^{3+} content (Figure 3.5f), since the ionic radius of Al^{3+} (0.535 Å in sixfold coordination) is much smaller than that of Zr^{4+} as anticipated [60]. However, the progressive substitution with Al^{3+} ($x \geq 0.4$) reduces the rhombohedral unit cell volume, resulting in a NaSICON phase mixture with rhombohedral and monoclinic symmetry and leading to the formation of $AlPO_4$. Substituting Zr^{4+} with Al^{3+} reduces the rhombohedral content and increases the monoclinic one (Figure 3.5e).

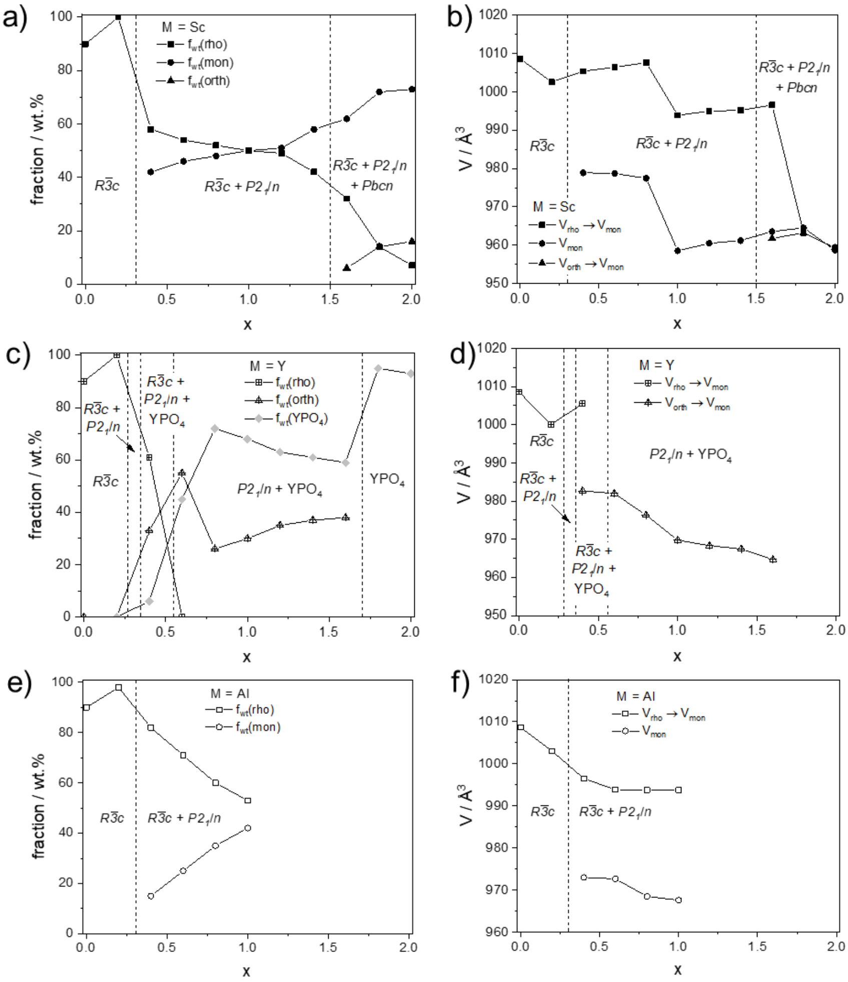

Figure 3.5: a, c, e) Evolution of the weight fraction of the NaSICON polymorphs (and YPO_4 in c); b, d, f) monoclinic unit cell volume as a function of x in $Li_{1+x}M_xZr_{2-x}P_3O_{12}$ where M = Sc, Y, and Al, respectively. Converted lattice parameters and literature data are listed in Annex 3 (LSZP ($0 \leq x \leq 2$)), Annex 4 (LYZP ($0.2 \leq x \leq 1.6$)), and Annex 5 (LAZP ($0.2 \leq x \leq 1$)).

Nuclear magnetic resonance investigations confirmed the presence of preferentially octahedral coordinated aluminum (Al_O) in $Li_{1+x}Al_xTi_{2-x}(PO_4)_3$, but with increasing x a significant proportion of Al was also found on tetrahedral sites (Al_T) [61, 62]. The presence of Al_T can be attributed to the segregation of the $AlPO_4$ phase, which is in good agreement with the XRD results of this work (Figure 3.3.1), but also to the limited substitution of P^{5+} (0.17 Å) with Al^{3+} (0.39 Å in fourfold coordination) [60] in the

NaSICON structure, presumably leading to the progressive destabilization of the lattice and the strong decline of ionic conductivity for compounds where $x > 0.6$ (Figure 3.3.4).

IV Solid-state Li^+ ion conductors in the system Li_2O-M_2O_3-ZrO_2-SiO_2-P_2O_5 Partial polyanion substitutions in $Li_{3+x}Sc_2Si_xP_{3-x}O_{12}$ ($0 \leq x \leq 0.6$) and $Li_{1.2+x}Sc_{0.2}Zr_{1.8}Si_xP_{3-x}O_{12}$ ($0.3 \leq x \leq 2.8$)

4.1 $Li_{3+x}Sc_2Si_xP_{3-x}O_{12}$ ($0 \leq x \leq 0.6$)

Powders belonging to the $Li_{3+x}Sc_2Si_xP_{3-x}O_{12}$ system with $0 \leq x \leq 0.6$ were synthesized via solution-assisted solid-state reaction (SA-SSR), as previously reported [51]. The ICP-OES results confirmed the nominal stoichiometry of the six calcined NaSICON $Li_{3+x}Sc_2Si_xP_{3-x}O_{12}$ powders with x = 0, 0.06, 0.15, 0.3, 0.4, and 0.6. The analytical values are very close to the targeted compositions after powder preparation, i.e. the substitution of P^{5+} with Si^{4+} was successful with a high level of precision (Table 4.1.1). The obtained atomic ratios were normalized to two moles scandium per formula unit. With the exception of $Li_3Sc_2P_3O_{12}$, the silicone and phosphorous contents deviate less than the experimental error (3 %). The lithium content was slightly lower than anticipated, which might be due to the uptake of small amounts of water in the Li_2CO_3 during storage.

Table 4.1.1: Composition of the $Li_{3+x}Sc_2Si_xP_{3-x}O_{12}$ ($0 \leq x \leq 0.6$) NaSICON powders calcined at 600 °C for 5 h determined by ICP-OES and normalized to two moles scandium per formula unit. The oxygen content was calculated on the basis of the cation contents.

x	**Analytical stoichiometry before sintering**
0	$Li_{2.98}Sc_2P_{2.9}O_{11.74}$
0.06	$Li_{3.04}Sc_2Si_{0.08}P_{2.96}O_{12.08}$
0.15	$Li_{3.14}Sc_2Si_{0.18}P_{2.83}O_{12.01}$
0.3	$Li_{3.26}Sc_2Si_{0.33}P_{2.72}O_{12.09}$
0.4	$Li_{3.37}Sc_2Si_{0.38}P_{2.62}O_{12}$
0.6	$Li_{3.57}Sc_2Si_{0.59}P_{2.41}O_{11.99}$

DTA/TG measurements were carried out up to 1600 °C to analyze the formation and stability of the crystalline phase, to quantify mass losses, and to identify the melting points. Materials of the studied series $Li_{3+x}Sc_2Si_xP_{3-x}O_{12}$ ($0 \leq x \leq 0.6$) have almost the same thermal behavior except for the material with x = 0.6. The TG curves show three successive mass losses accompanied by endothermic signals. As shown in Figures 4.1.1a and 4.1.1b, the first mass loss $\Delta m_1 \approx 0.9$ % was observed in the temperature range from 25 °C to 250 °C and is mainly associated with physisorbed water, whereas the second mass

loss $\Delta m_2 \approx 2$ % occurred up to 560 °C in two steps accompanied by an endothermic signal peaking around 330 °C, which has been attributed to the release of crystal water from the materials. Furthermore, the third loss $\Delta m_3 \approx 2.6$ % appeared in the temperature range from 1300 °C to 1600 °C and is ascribed to the evaporation of lithium oxide from the material [57]. The evaporation of lithium oxide is pronounced when the materials are fully molten. The broad exothermic signal between 400 °C and 600 °C, which is not accompanied by mass loss, is interpreted as the phase formation and crystallization region of the materials. Very sharp exothermic signals were detected at around 1400 °C, which are ascribed to the melting point of the materials with $0 \leq x \leq 0.4$, whereas the sample with $x = 0.6$ showed a partial melting point at 1100 °C followed by complete melting at 1170 °C. Weak signals at these two temperatures were also observed for $x = 0.3$ and $x = 0.4$. In fact, the increased silicate substitution in the $Li_{3+x}Sc_2Si_xP_{3-x}O_{12}$ series leads to a decrease of the melting temperature. This result is in agreement with previous observations [48].
Dilatometry was used to determine the optimal sintering temperature of the materials. In order to obtain full density for a typical pellet with a green density of 50 %, a theoretical final value of 20.6 % shrinkage is necessary. Larger shrinkage values obtained in dilatometer measurements indicate a (partial) melting of the material or a continuous plastic deformation of the sample induced by the low pressure of the push-rod [58]. The shrinkage behavior of the pellets of the $Li_{3+x}Sc_2Si_xP_{3-x}O_{12}$ series with $x = 0$, 0.06, 0.15, 0.3, 0.4, and 0.6 was recorded during constant heating (300 K/h) until a shrinkage of around 23 % was reached (Figure 4.1.1c). The shrinkage behavior of the samples strongly varies with increasing silicate content (Figure 4.1.1c). The samples with $x = 0$ and $x = 0.06$ show rather sluggish shrinkage at temperatures up to 1300 °C and a steep slope at about 1370 °C indicating their melting. Materials with $0.15 \leq x \leq 0.4$ exhibit shrinkage up to ~15 % at 1050 °C followed by expansion until 1250 °C, 1320 °C, and 1340 °C for compositions with $x = 0.15$, 0.3, and 0.4, respectively.

To achieve the optimum sintering conditions for each composition, the pressed pellets were sintered in air at different temperatures. The highest temperature was initially determined from the dilatometry measurements and optimized by lowering it by 50 °C in the subsequent tests. The sintering experiments in the furnace were carried out between 900 °C and 1400 °C for materials with $x = 0$ and $x = 0.06$, between 900 °C and 1350 °C for materials with $x = 0.15$, 0.3, and 0.4, and only from 900 °C to 1200 °C for the material with $x = 0.6$, since the pellets already melted at about 1220 °C. After several sintering tests in the same oven and under the same conditions (3 h, 300 K/h cooling and heating), the optimal sintering temperatures that yielded the highest relative densities were determined and are listed in Table 4.1.2. No significant shrinkage was observed below the given temperatures, while some micro-cracks were observed above them for compositions with $x = 0$, 0.06, and 0.6.

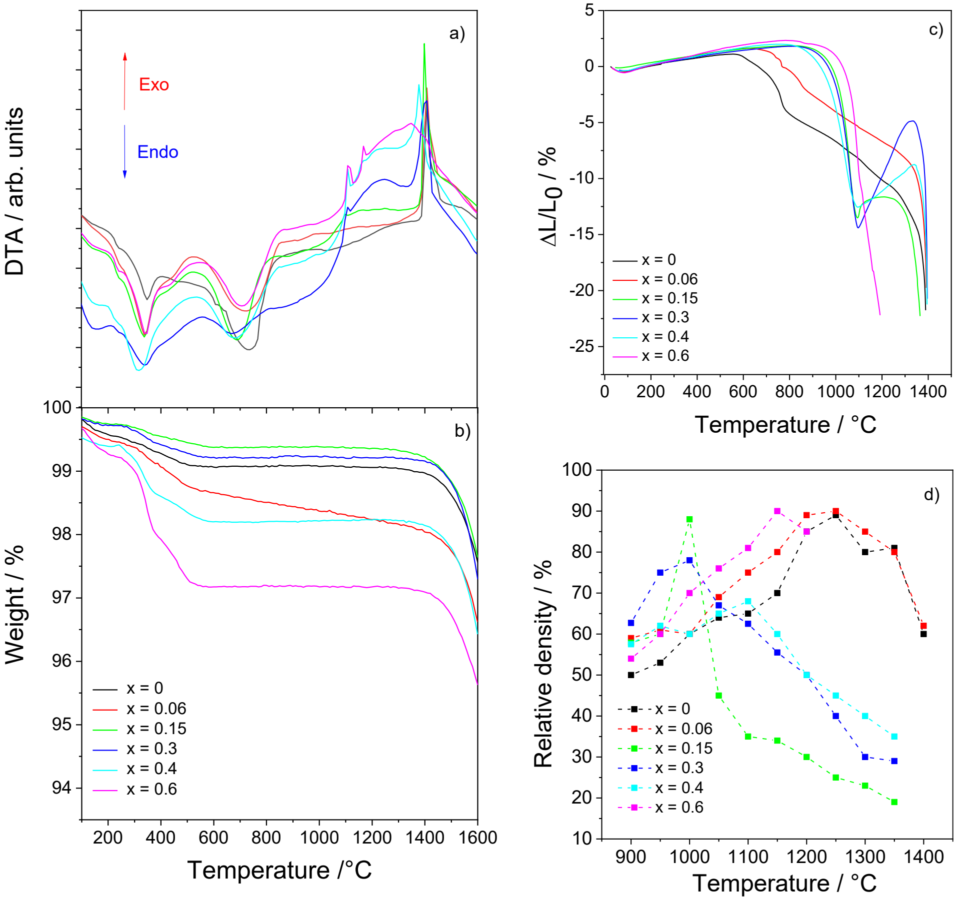

Figure 4.1.1: Thermal and dilatometry investigations of the Li$_{3+x}$Sc$_2$Si$_x$P$_{3-x}$O$_{12}$ series ($0 \leq x \leq 0.6$): **a)** DTA results, **b)** TG results, **c)** sintering curves of samples with a constant heating rate up to 1600 °C, **d)** relative densities obtained after sintering (3 h) at different sintering temperatures.

The sintering experiments in the furnace revealed a systematic decrease in density with increasing sintering temperature for compositions with x = 0.15, 0.3, and 0.4. The reason for this trend is the volume expansion, which was already recorded by dilatometry in connection with deformations and the partial melting of the pellets. The relative densities obtained at different sintering temperatures from 900 °C to 1400 °C are shown in Figure 4.1.1d.

In an attempt to further increase the relative density of the sintered pellets, an optimized two-step sintering procedure was applied [59]. The pellets were first subjected to the optimum sintering temperatures determined above (Table 4.1.2) for a short period of time (0.25 h) and then annealed at a reduced temperature for a longer period of time (4 h). The sintering conditions were systematically optimized by varying the second temperature in the range of 700 °C to 1000 °C for materials with x = 0 and x = 0.06 with 50 °C steps and in the range of 700 °C to 900 °C with 50 °C steps for materials with x = 0.15, 0.3, 0.4, and 0.6. The relative density of the pellets was thus increased for all compositions (Table 4.1.2).

It should be noted that the NaSICON solid electrolyte is highly susceptible to Li_2O loss during conventional sintering, which typically requires higher temperatures of about 1200 °C and a longer dwell time of several hours [34]. The lower sintering temperature and shorter dwell time are expected to minimize the Li_2O evaporation, resulting in higher conductivity [60]. In contrast, higher sintering temperatures typically lead to a higher relative density, which also has a positive effect on ionic conductivity. The combination of these two approaches is the key to manufacturing solid electrolytes with high ionic conductivity [61]

Table 4.1.2: Melting points determined by DTA measurements, sintering parameters for the one-step sintering and two-step sintering (T_s = sintering temperature, t_s = dwell time), and the resulting densities of $Li_{3+x}Sc_2Si_xP_{3-x}O_{12}$ ($0 \leq x \leq 0.6$) compounds.

Composition	**Melting temperature / °C**	**One-step sintering**		**Two-step sintering**		
		T_s / °C, t_s /h	**Relative density / %**	**T_{s1} / °C, t_{s1} / h**	**T_{s2} / °C, t_{s2} / h)**	**Relative density / %**
$Li_3Sc_2P_3O_{12}$	1410	1250, 3	89	1250, 0.25	800, 4	96
$Li_{3.06}Sc_2Si_{0.06}P_{2.94}O_{12}$	1410	1250, 3	90	1250, 0.25	800, 4	94
$Li_{3.15}Sc_2Si_{0.15}P_{2.85}O_{12}$	1390	1000, 3	88	1000, 0.25	800, 4	93
$Li_{3.3}Sc_2Si_{0.3}P_{2.7}O_{12}$	1100, 1390	1000, 3	78	1000, 0.25	800, 4	85
$Li_{3.4}Sc_2Si_{0.4}P_{2.6}O_{12}$	1100, 1380	1100, 3	68	1100, 0.25	800, 4	82
$Li_{3.6}Sc_2Si_{0.6}P_{2.4}O_{12}$	1100, 1170	1150, 3	90	1150, 0.25	800, 4	96

In order to evaluate the possible Li_2O loss after one-step and two-step sintering, the pellets were analyzed by ICP-OES. As can be seen in Figure 4.1.2 the lithium content is lower than anticipated in all cases. However, Li_2O loss can be limited by performing a two-step sintering procedure and the reduction of Li_2O loss is clearly seen in Figure 4.1.2.

During the two-step sintering procedure, the materials were annealed with shorter times compared to the conventional sintering process used by Peng et al. [48], in which the pressed pellets of the materials were sintered for 6 h. The lower temperature and shorter times likely result in less Li_2O loss, which, in turn, should result in higher grain boundary conductivity, as suggested by Ban et al. [62]. Therefore, the use of a two-step sintering procedure not only reduces the energy input and increases the relative density of the pellets, but also minimizes the loss of Li_2O due to the short dwell time at a high temperature [58, 59]. This heat treatment sequence was thus applied to sinter all samples for further investigations.

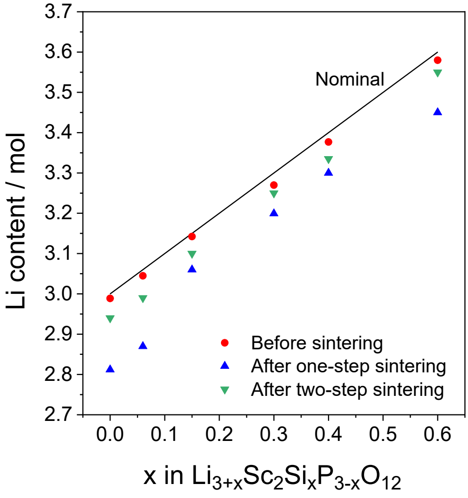

Figure 4.1.2: Variation of lithium content obtained from ICP-OES in the $Li_{3+x}Sc_2Si_xP_{3-x}O_{12}$ series ($0 \leq x \leq 0.6$) before sintering, after one-step sintering, and after two-step sintering. The results were normalized to 2 mole scandium per formula unit. The pellets were sintered at the temperatures listed in Table 4.1.2.

XRD patterns (Figure 4.1.4) of the studied materials $Li_{3+x}Sc_2Si_xP_{3-x}O_{12}$ ($0 \leq x \leq 0.6$) recorded after two-step sintering (Table 4.1.2) exhibit reflections of the orthorhombic structure (space group *Pbcn*, ICSD No. 83913) [29] and/or reflections of the monoclinic structure (space group $P2_1/n$, ICSD No. 91112) [53], since both phases are almost identical and resemble each other in their reflection patterns, as shown in Figure 4.1.3. However, since the two small reflections at $2\theta = 17.7°$ and 34° could hardly be detected in all XRD patterns, the lattice parameters (see Figure 4.1.5) were determined with the monoclinic symmetry in accordance with [30].

Moreover, a small amount of secondary phase such as orthorhombic Li_3PO_4 (ICSD No. 50058) (space group *Pmnb*) [63] in the compositions x = 0.4 and x = 0.6 were found as mentioned in [38, 64]. Cubic $Sc(PO_3)_3$ (ICSD No. 1719) (space group $I\bar{4}3d$) was also detected as an impurity in the material with x = 0.6 [65]. For the unsubstituted LSP, a very small amount of rhombohedral P_2O_5 (ICSD No. 16610) [66] remained unreacted during the synthesis, as also reported in previous work

[31, 55], and unreacted monoclinic Sc_2O_3 (space group *C2/m;* ICSD no. 160218) [67] was also detected. However, for the same $Li_{3+x}Sc_2Si_xP_{3-x}O_{12}$ series, it was previously detected that "$Li_{3.2}Sc_2(PO_4)_3$" is the main phase for all samples with small amounts of an unidentified impurity phase [48].

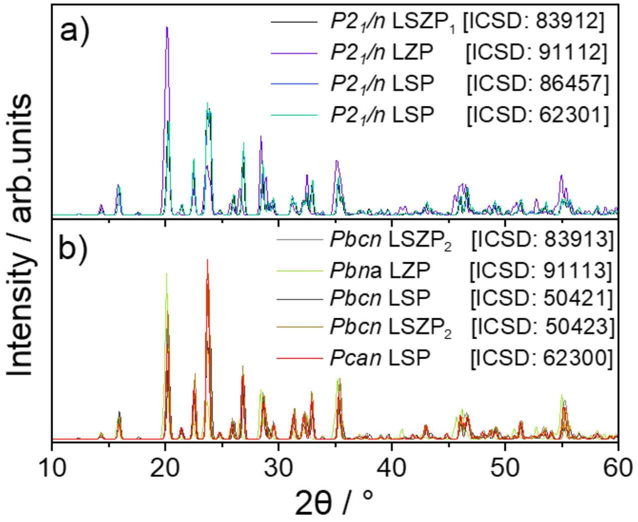

Figure 4.1.3: XRD patterns for reported NaSICON materials with a) monoclinic symmetry (space group $P2_1/n$): $Li_{2.96}(Sc_{1.96}Zr_{0.04})(PO_4)_3$ (LSZP1) [ICSD N°: 83912] [29], $LiZr_2(PO_4)_3$ (LZP) [ICSD N°: 91112] [53], $Li_3Sc_2(PO_4)_3$ (LSP) [ICSD N°: 86457] [54], and LSP [ICSD N°: 62301] [40], and b) orthorhombic symmetry (space groups *Pbcn*, *Pbna,* or *Pcan*): $Li_{2.8}(Sc_{1.8}Zr_{0.2})(PO_4)_3$ (LSZP2) [ICSD N°: 83913] [29], LSP [ICSD N°: 50421] [30], LSZP2 [ICSD N°: 50423] [30], LZP [ICSD N°: 91113] [53], and LSP [ICSD N°: 62300] [55]

The materials in the $Li_{3+x}Sc_2Si_xP_{3-x}O_{12}$ series demonstrate a non-linear dependence of monoclinic lattice parameters and the unit cell volume on the silicate substitution. The unit cell volume increases slightly up to x = 0.06, remains nearly constant up to x = 0.3, and increases for higher x values. The lattice parameter *a* increases slightly up to x = 0.3, decreases at x = 0.4, and increases again at x = 0.6, but *b* remains constant (Figure 4.1.5, the crystallographic data refined with orthorhombic and monoclinic symmetry are listed in Annex 7 and 8, respectively). The β angle is in the range of $89.8° \leq \beta \leq 90.2°$, thus indicating the close proximity to the orthorhombic setting.

The variation of the monoclinic lattice parameters during the progressive anionic substitution of $(PO_4)^{3-}$ by $(SiO_4)^{4-}$ is not primarily due to the different ionic radii of Si^{4+} (0.26 Å) and P^{5+} (0.17 Å) in the tetrahedral coordination [68], as this does not necessarily lead to a small volume increase of the tetrahedra. The electrostatic redistribution of charges and the additional uptake of Li^+ ions are more important factors here.

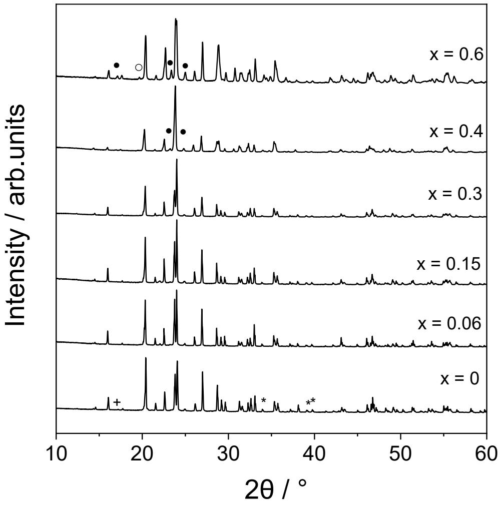

Figure 4.1.4: XRD patterns of $Li_{3+x}Sc_2Si_xP_{3-x}O_{12}$ ($0 \leq x \leq 0.6$) after two-step sintering (see Table 4.1.2). ○: $Sc(PO_3)_3$, +: P_2O_5, ●: Li_3PO_4, * : Sc_2O_3.

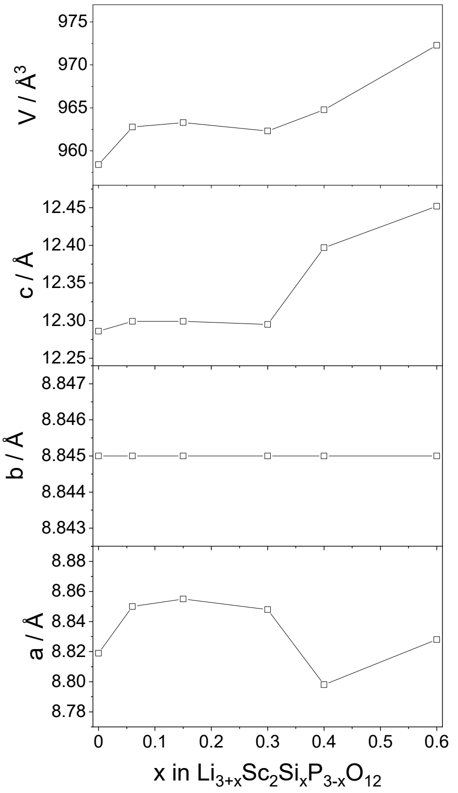

Figure 4.1.5: Variation of monoclinic lattice parameters and unit cell volume of the $Li_{3+x}Sc_2Si_xP_{3-x}O_{12}$ series ($0 \leq x \leq 0.6$).

The ionic conductivity of the six compositions studied was determined from impedance spectra measured at 25 °C. The Nyquist plot of the impedance spectra is shown in Figure 4.1.6 a, and the equivalent circuit used is also shown. For all samples, only one semicircle emanating from the origin at high frequencies and a straight line at low frequencies corresponding to the electrode polarization were observed.

The radius of the semicircle decreases with increasing silicate substitution in $Li_{3+x}Sc_2Si_xP_{3-x}O_{12}$ up to $x = 0.15$ and subsequently increases again. Phenomenologically, the sample with $x = 0.15$ thus shows the highest ionic conductivity along the series.

The total conductivity of the samples was calculated with Equation 14. The total ionic conductivity values at 25 °C as a function of composition are listed in Table 4.1.3, and the evolution of the total ionic conductivity is shown in Figure 4.1.6b. The total ionic conductivity initially increases with increasing x, and the maximum value of 1.2×10^{-5} S cm^{-1} was obtained with $Li_{3.15}Sc_2Si_{0.15}P_{2.85}O_{12}$. The observed increase in total conductivity can be mainly attributed to the substitution of silicate in $Li_{3+x}Sc_2Si_xP_{3-x}O_{12}$ and the additional Li^+ ions needed for charge balance. Consequently, more lithium ions led to a significant improvement in ionic conductivity.

Table 4.1.3: Resulting densities of ceramics densified in two sintering steps, ionic conductivity at 25 °C and activation energy for $Li_{3+x}Sc_2Si_xP_{3-x}O_{12}$ ($0 \leq x \leq 0.6$)

x	Relative density / %	$\sigma_{25°C}$ / S cm^{-1}	Activation energy / eV
0	96	0.2×10^{-5}	0.21
0.06	94	0.46×10^{-5}	0.24
0.15	93	1.20×10^{-5}	0.19
0.3	85	0.95×10^{-5}	0.20
0.4	82 3	0.76×10^{-5}	0.21
0.6	96	0.41×10^{-5}	0.24

The subsequent decrease in ionic conductivity can be attributed to two reasons. On the one hand, further increasing the lithium and silicate content seems to destabilize the NaSICON structure and generate an increasing amount of Li_3PO_4, especially for the composition with x = 0.6. On the other hand, the highest ionic conductivity value can also be attributed to the densification process and the quality of the ceramic material. Even when the lithium content is increased, the compositions with x = 0.3 and x = 0.4 exhibit poor ionic conductivity due to their low relative density. It is known that samples with a density below 90 % can easily lose up to 90 % of their ionic conductivity [46]. Therefore, the potential conductivity of $Li_{3.3}Sc_2Si_{0.3}P_{2.7}O_{12}$ and $Li_{3.4}Sc_2Si_{0.4}P_{2.6}O_{12}$ may be about one order of magnitude higher than was measured. The results are very similar to those of Peng et al. [48]. The ionic conductivity of LSP is lower compared to some of the reported values in the literature [29, 30, 32, 48, 56, 69-71]. The activation energy E_a of the ionic conductivity of all compounds was obtained from impedance measurements at different temperatures and using the Arrhenius law (Equation 16). The activation energy values were calculated from the slope of

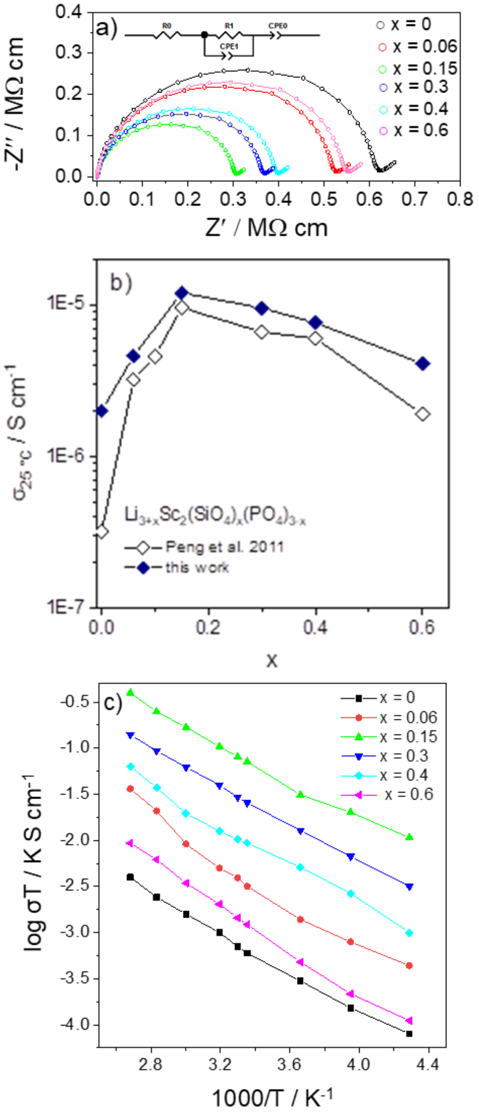

Figure 4.1.6: a) Nyquist plot of impedance spectra at 25 °C after accounting for the sample dimensions. The equivalent circuit for data fitting is also shown. b) Total ionic conductivity at 25 °C depending on the silicate content in $Li_{3+x}Sc_2Si_xP_{3-x}O_{12}$ ($0 \leq x \leq 0.6$). c) Arrhenius plot of σ_t of $Li_{3+x}Sc_2Si_xP_{3-x}O_{12}$ ($0 \leq x \leq 0.6$) measured in the temperature range of -40 °C to 100 °C.

ln $\sigma_t T$ versus inverse temperature in the temperature range of -40 °C to 100 °C as shown in Figure 4.1.6c. The calculated values of E_a after linear fitting are summarized in Table 4.1.3. The activation energy of $Li_{3+x}Sc_2Si_xP_{3-x}O_{12}$ specimens varies between 0.19 eV and 0.24 eV without any clear trend. These values are comparable with literature data of other NaSICON-type materials [e.g. 12, 18,20,49].

Overall, optimizing the sintering conditions resulted in increased ionic conductivity along the $Li_{3+x}Sc_2Si_xP_{3-x}O_{12}$ series compared to the data reported by Peng et al [48]. Nevertheless, the obtained ionic conductivities are still too low for battery applications.

4.2 $Li_{1.2+x}Sc_{0.2}Zr_{1.8}Si_xP_{3-x}O_{12}$ ($0 \leq x \leq 2.8$)

The powders belonging to the $Li_{1.2+x}Sc_{0.2}Zr_{1.8}Si_xP_{3-x}O_{12}$ system ($0 \leq x \leq 2.8$) were also synthesized by SA-SSR. The ICP-OES results are summarized in Table 4.2.1. The obtained atomic ratios were normalized to 1.8 moles zirconium per formula unit. The final compositions of the calcined solid electrolyte powders are close to the nominal stoichiometry.

The coupled thermogravimetric DTA/TG study shows that the six Si-containing materials, chosen from the $Li_{1.2+x}Sc_{0.2}Zr_{1.8}Si_xP_{3-x}O_{12}$ ($0.3 \leq x \leq 2.8$) system, clearly have the same thermal behavior except for the material with the lowest silicate content (x = 0.3), as shown in Figures 4.2.1a and 4.2.1b. The TG curves show four temperature regions with mass losses.

Table 4.2.1: Composition of $Li_{1.2+x}Sc_{0.2}Zr_{1.8}Si_xP_{3-x}O_{12}$ powders with $0 \leq x \leq 2.8$ calcined at 600 °C determined by ICP-OES and normalized to 1.8 moles zirconium per formula unit. The oxygen content was calculated on the basis of the cation contents.

x	Analytical stoichiometry before sintering
0	$Li_{1.21}Sc_{0.21}Zr_{1.8}P_{3.02}O_{11.99}$
0.3	$Li_{1.53}Sc_{0.21}Zr_{1.8}Si_{0.31}P_{2.70}O_{12.01}$
0.8	$Li_{2.02}Sc_{0.20}Zr_{1.8}Si_{0.75}P_{2.08}O_{12}$
1.3	$Li_{2.60}Sc_{0.19}Zr_{1.8}Si_{1.27}P_{1.71}O_{11.98}$
1.8	$Li_{2.95}Sc_{0.19}Zr_{1.8}Si_{1.78}P_{1.31}O_{12.02}$
2.3	$Li_{3.59}Sc_{0.21}Zr_{1.8}Si_{2.28}P_{0.75}O_{11.99}$
2.8	$Li_{4.11}Sc_{0.21}Zr_{1.8}Si_{2.82}P_{0.22}O_{12.01}$

The first weight loss occurs below 200 °C and is attributed to the release of moisture. The second weight loss starts at about 300 °C and can be attributed to the evaporation of crystal water and the emission of carbon dioxide. In the DTA curves, this weight loss is accompanied by the presence of an endothermic broad signal centered at 350 °C. This endothermic signal was detected for all compositions except for $x = 1.8$ and $x = 2.3$. The third weight loss between 800 °C and 950 °C only affects the powders with $x = 2.3$ and $x = 2.8$ and is associated with an endothermic signal at about 950 °C and 980 °C, respectively. This endothermic peak is very likely a partial melting of these two samples and the reason for the first strong shrinkage in the dilatometry curves (Figure 4.2.1c). The fourth weight loss appears in the temperature range from 1300 °C to 1400 °C, which has been attributed to the evaporation of Li_2O. The exothermic peaks observed at 1050 °C and at 1150 °C in the DTA curves, which are not accompanied by mass losses, probably correspond to the decomposition of the compounds. The melting point of the materials with $x = 0.3$ and $x = 0.8$ could not be clearly detected. Only the materials with $x = 2.3$ and $x = 2.8$ show three exothermic peaks, indicating a complex decomposition behavior between 950 °C and 1200 °C.

The sintering behavior of the calcined powders was examined by dilatometry. The pellets shrink up to ~ 23 % between 1030 °C and 1220 °C. The sintering behavior is almost identical for all materials. With the exception of the samples with higher silicate content ($x = 1.8$, 2.3, and 2.8), which, as mentioned above, exhibit multiple-step shrinkage behavior, the other pellets show the onset of sintering between 850 °C ($x = 0.3$) and 950 °C ($x = 0.8$, 1.3) and the maximum shrinkage rate at about 1050 °C.

The pressed pellets were sintered at different temperatures to adjust the optimal sintering temperature for each composition. The sintering experiments in the furnace were carried out between $T_{10\%}$ and $T_{20\%}$, corresponding to 10 % and 20 % shrinkage in the dilatometry curves, in increments of 20 °C for 3 h in air. The resulting optimum sintering temperatures in relation to the densification of the materials are shown in Figure 4.2.1d. The relative density increases gradually with increasing sintering temperature up to 1200 °C, and the highest densities of 89 % and 91 % were obtained for compositions with $x = 0.3$ and $x = 0.8$, respectively. The composition with $x = 1.3$ exhibited the highest relative density of 90 % at 1060 °C and melted at 1070 °C.

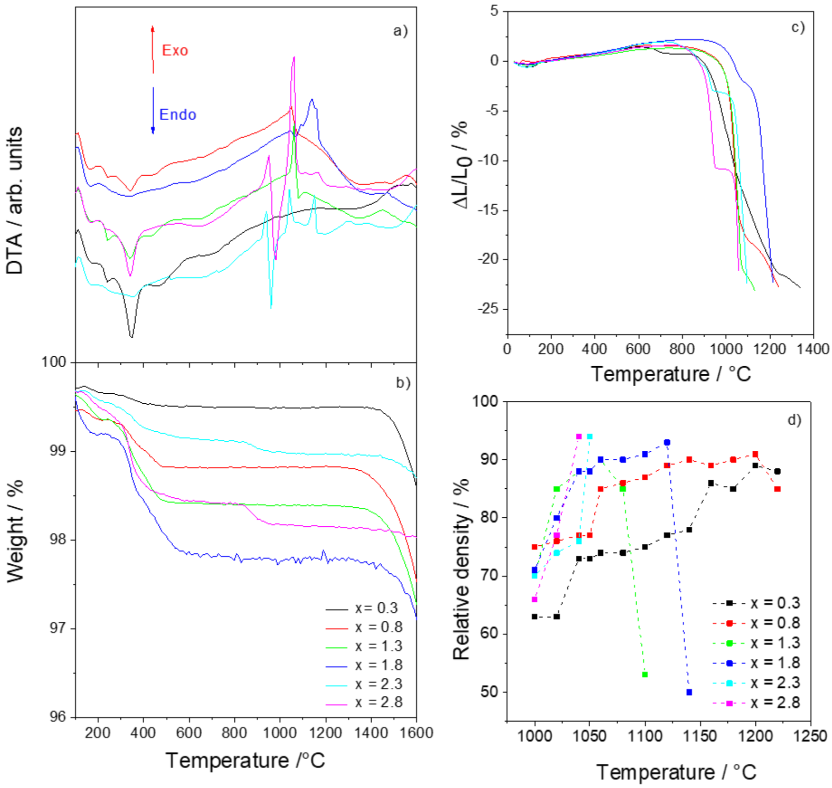

Figure 4.2.1: Thermal and dilatometry investigations of the $Li_{1.2+x}Sc_{0.2}Zr_{1.8}Si_xP_{3-x}O_{12}$ series (0.3 ≤ x ≤ 2.8): a) DTA results, b) TG results, c) sintering curves with a constant heating rate up to 1400 °C, and d) relative densities obtained at different sintering temperatures after one-step sintering.

Table 4.2.2: Melting points determined by DTA measurements, one-step sintering and two-step sintering parameters, and resulting densities of $Li_{1.2+x}Sc_{0.2}Zr_{1.8}Si_xP_{3-x}O_{12}$ (0.3 ≤ x ≤ 2.8) compounds. For comparison, the values for $Li_{1.2}Sc_{0.2}Zr_{1.8}P_3O_{12}$ are included (see [50]).

Composition	**Melting temperature/ °C**	**One-step sintering**		**Two-step sintering**		
		T_s / °C, t_s /h	**Relative density / %**	**T_{s1} (°C, t_{s1}/h)**	**T_{s2} (°C, t_{s2}/h)**	**T_s / °C, t_s /h**
$Li_{1.2}Sc_{0.2}Zr_{1.8}P_3O_{12}$	1520	1280, 3	85	1280, 0.25	980, 3	94
$Li_{1.5}Sc_{0.2}Zr_{1.8}Si_{0.3}P_{2.7}O_{12}$	1380	1200, 3	89	1200, 0.25	800, 4	93
$Li_2Sc_{0.2}Zr_{1.8}Si_{0.8}P_{2.2}O_{12}$	1290	1200, 3	91	1200, 0.25	800, 4	94
$Li_{2.5}Sc_{0.2}Zr_{1.8}Si_{1.3}P_{1.7}O_{12}$	1070	1060, 3	90	1060, 0.25	800, 4	91

$Li_3Sc_{0.2}Zr_{1.8}Si_{1.8}P_{1.2}O_{12}$	1140	1120, 3	93	1120, 0.25	800, 4	94
$Li_{3.5}Sc_{0.2}Zr_{1.8}Si_{2.3}P_{0.7}O_{12}$	1060, 1160	1050, 3	94	1050, 0.25	800, 4	96
$Li_4Sc_{0.2}Zr_{1.8}Si_{2.8}P_{0.2}O_{12}$	1040, 1150	1040, 3	94	1040, 0.25	800, 4	95

Almost identical behavior was observed for the composition with x = 1.8, which exhibited the highest relative density of 93 % at 1120 °C and melted at 1140 °C. Materials with high silicate content (x = 2.3 and x = 2.8) showed the highest relative density of 94 % at 1050 °C and 1040 °C, respectively, and melted at around 1060 °C. As an overall result, sintering of the pellets in the furnace at $T_{20\%}$ showed a high relative density for all compositions. Two-step sintering was also carried out with this set of compositions to improve the quality of the ceramics. The relative densities are summarized in Table 4.2.2. Increasing the partial anion substitution of silicate for phosphate in $Li_{1.2+x}Sc_{0.2}Zr_{1.8}Si_xP_{3-x}O_{12}$ lowered the sintering temperature from 1280 °C and 1200 °C (x = 0, see [50], and x = 0.3, respectively) to 1040 °C with x = 2.8.

After sintering at temperatures associated with 20 % shrinkage, the lithium content was slightly lower than the desired compositions (Figure 4.2.2) due to weight losses during sintering. Nevertheless, this result is very promising with respect to the loss of Li_2O, since the evaporation of Li_2O was much higher for the $Li_{3+x}Sc_2Si_xP_{3-x}O_{12}$ series (Figure 4.1.2). The substitution of phosphate with silicate in the $Li_{1.2+x}Sc_{0.2}Zr_{1.8}Si_xP_{3-x}O_{12}$ series lowered the sintering temperatures while reducing the evaporation of lithium species.

These results are in good agreement with the weight losses above 1200 °C in the DTA curves of both series, which were attributed to the evaporation of lithium oxide from the materials in the temperature range from 1300 °C to 1600 °C. The weight loss in the $Li_{3+x}Sc_2Si_xP_{3-x}O_{12}$ series was $\Delta m_3 \approx 2.58$ %, but only ≈ 1.53 % in the $Li_{1.2+x}Sc_{0.2}Zr_{1.8}Si_xP_{3-x}O_{12}$ series. Δm_3 was calculated according to equation 20 in the temperature interval mentioned above.

$$\Delta m_3 = \Sigma \frac{\Delta m_i}{n} \qquad \text{Equation 20}$$

with Δm_3 = mean value of the third mass loss of all compounds i, which is attributed to the evaporation of Li_2O from the materials, n = number of compounds.

The results show that Li_2O vaporization was affected by the sintering process and the presence of zirconium in the composition.

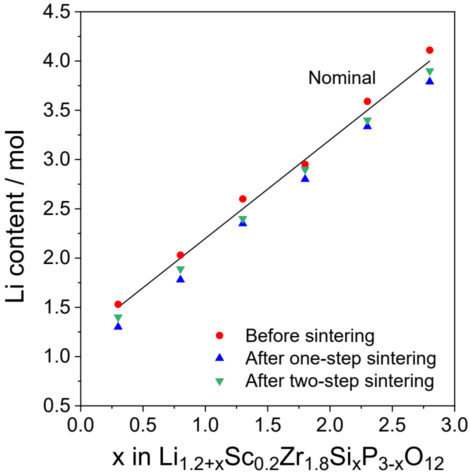

Figure 4.2.2: Variation of lithium content obtained from ICP-OES in the $Li_{1.2+x}Sc_{0.2}Zr_{1.8}Si_xP_{3-x}O_{12}$ series with ($0.3 \leq x \leq 2.8$) before and after sintering. The results were normalized to 1.8 moles zirconium per formula unit. The pellets were sintered at temperatures listed in Table 4.2.2.

The XRD patterns of the materials $Li_{1.2+x}Sc_{0.2}Zr_{1.8}Si_xP_{3-x}O_{12}$ with $0.3 \leq x \leq 2.8$ after sintering at temperatures listed in Table 4.2.2 are shown in Figure 4.2.3. The patterns of the materials with $0.3 \leq x \leq 1.8$ were refined with monoclinic NaSICON symmetry (*P2₁/n*) [29] and with orthorhombic symmetry (*Pbcn*) [53] (see also Annexes 9 and 10), since both phases are similar in their reflection patterns, as shown in Figure 4.1.3. The results are in good agreement with the reported data for the composition $Li_3Sc_2(PO_4)_3$ [70]. The compositions with x = 2.3 only crystallized with monoclinic symmetry with (*P2₁/n*). The XRD patterns of the material with x = 2.8 exhibited complete decomposition.

The materials with x = 2.3 and x = 2.8 clearly show the presence of several secondary phases such as orthorhombic Li_3PO_4 with space group *Pmnb* (ICSD No. 50058), monoclinic ZrO_2 (*P2₁/c*; ICSD No. 60900) [72], and orthorhombic Li_2SiO_3 (*Ccm2₁*; ICSD No. 853) [73]. In addition, tetragonal $ZrSiO_4$ (*I4₁/amd*; ICSD No. 100243) [74] was also observed as an impurity phase in different amounts – not only for the decomposed materials (x = 2.3 and x = 2.8), but also for the compositions with $0.3 \leq x \leq 1.8$.

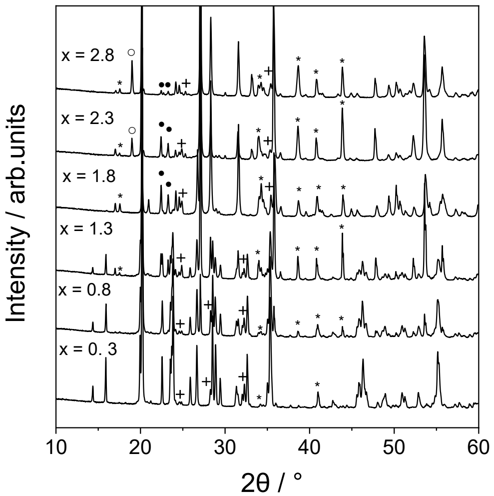

Figure 4.2.3: XRD patterns of $Li_{1.2+x}Sc_{0.2}Zr_{1.8}Si_xP_{3-x}O_{12}$ with $(0.3 \leq x \leq 2.8)$ after sintering at temperatures referring to the optimum densification: 1200 °C (x = 0.3, 0.8), 1060 °C (x = 1.3), 1120 °C (x = 1.8), 1050 °C (x = 2.3), 1040 °C (x = 2.8). +: ZrO_2, ●: Li_3PO_4, ○: Li_2SiO_3, ★: $ZrSiO_4$.

Using Rietveld refinements, the $ZrSiO_4$ content in materials with x = 0.3, 0.8, 1.3, 1.8, 2.3, and 2.8 was estimated to be 5, 11, 12, 14, 16, and 13 wt.%, respectively (Table 4.2.3). From these values and the appearance of $ZrSiO_4$ over a wide range, it is clear that only a smaller fraction of the silicate substitution is incorporated in the NaSICON structure than expected. The molar amount of silicate in both phases can be calculated from the densities of $Li_{1.2}Sc_{0.2}Zr_{1.8}P_3O_{12}$ (3.09 g cm^{-3} [50]) and $ZrSiO_4$ (4.56 g cm^{-3} [73]) and the molar masses (Table 4.2.3). The silicate content in the NaSICON phase is always lower than the nominal value, and from the derived trend it can be deduced that coexistence with $ZrSiO_4$ starts at $x < 0.2$. These results indicate a continuous destabilization of the NaSICON materials along the series until decomposition occurs, which was detected at 960 °C and 980 °C in the DTA curves of the materials with x = 2.3 and x = 2.8, respectively, together with the various phases recorded by XRD.

Table 4.2.3: Fractions of NaSICON polymorphs and impurities in the $Li_{1.2+x}Sc_{0.2}Zr_{1.8}Si_xP_{3-x}O_{12}$ series (in wt.%) as well as the molar distribution of silicate between $ZrSiO_4$ and the NaSICON phase.

x	**Monoclinic / wt.%**	**Ortho-rhombic / wt.%**	**$ZrSiO_4$ / wt.%**	**ZrO_2 / wt.%**	**Li_3PO_4/ wt.%**	**Li_2SiO_3 / wt.%**	**$ZrSiO_4$ / mol**	**Silicate in NaSICON / mol**
0.3	40	55	5	0	0	0	0.12	0.18
0.8	42	47	11	0	0	0	0.24	0.56
1.3	48	40	12	0	0	0	0.26	1.04
1.8	55	31	14	0	0	0	0.29	1.51
2.3	68	0	16	8	6	2	-	-
2.8	Decomposition							

Figure 4.2.4 shows the variation of the refined cell parameters and cell volume of the $Li_{1.2+x}Sc_{0.2}Zr_{1.8}Si_xP_{3-x}O_{12}$ ($0.3 \leq x \leq 1.8$) series. The cell parameters were refined based on orthorhombic and monoclinic symmetry for the NaSICON phases. The converted monoclinic values of $Li_{1.2}Sc_{0.2}Zr_{1.8}P_3O_{12}$ (see [50]) are given for comparison.

In the orthorhombic system, a slight enlargement of the lattice is observed in the *a*, *b*, and *c* directions until x = 0.8, at which point the lattice shrinks again in all three directions. In the monoclinic system, the lattice parameters *a* and *c* are the first to show shrinkage, while the lattice parameter *b* remains almost constant. The cell volume decreases in both modifications, but decreases first in the monoclinic lattice from x = 0 to x = 0.2. The subsequent region of almost constant volume shows that the solubility limit for the silicate substitution is already reached at x = 0.2 and likely even earlier, since a small amount of $ZrSiO_4$ has already been formed. The following volume decrease of the orthorhombic lattice between x = 0.3 and x = 1.8 can be interpreted as the first stage of destabilization of the NaSICON lattice.

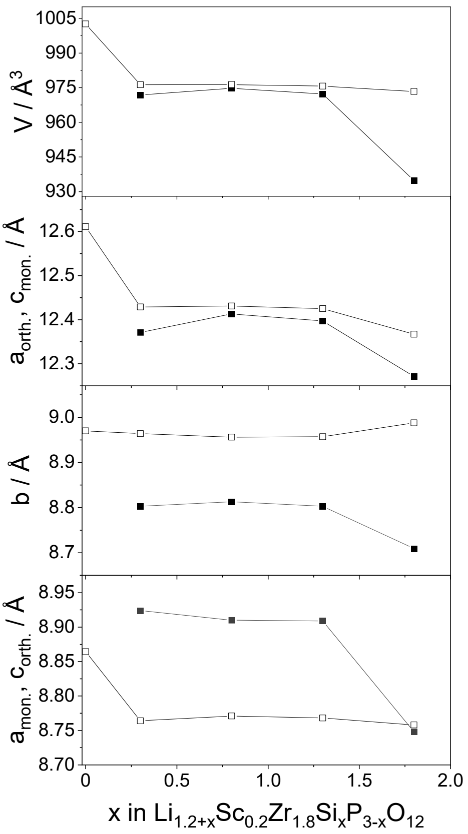

Figure 4.2.4: Variation of orthorhombic (filled symbols) and monoclinic (open symbols) lattice parameters and unit cell volume in the $Li_{1.2+x}Sc_{0.2}Zr_{1.8}Si_xP_{3-x}O_{12}$ series ($0 \leq x \leq 1.8$).

Impedance spectra were measured at 25 °C, and the Nyquist plots of $Li_{1.2+x}Sc_{0.2}Zr_{1.8}Si_xP_{3-x}O_{12}$ with $0.3 \leq x \leq 1.8$ are shown in Figure 4.2.5. The fitted curves using the given equivalent circuit are also shown. For all samples, only one semicircle was observed at high frequencies, starting at the origin. The radius of the semicircle increases with increasing silicate substitution. The material $Li_{1.5}Sc_{0.2}Zr_{1.8}Si_{0.3}P_{2.7}O_{12}$ with the lowest silicate content ($x = 0.3$) thus shows the smallest R_t along the series. The total conductivity of the samples was calculated using Equation 14 and the values are listed in Table 4.2.4.

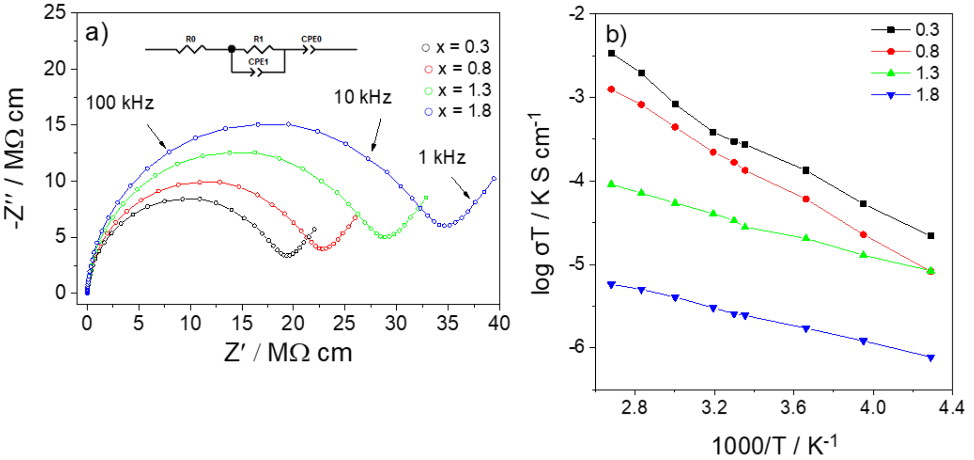

Figure 4.2.5: a) Nyquist plot of impedance spectra at 25 °C of $Li_{1.2+x}Sc_{0.2}Zr_{1.8}Si_xP_{3-x}O_{12}$ ($0.3 \leq x \leq 1.8$) after taking the sample dimensions into account. The equivalent circuit is also shown. b) Arrhenius plot of σ_t of $Li_{1.2+x}Sc_{0.2}Zr_{1.8}Si_xP_{3-x}O_{12}$ ($0.3 \leq x \leq 1.8$) measured in the temperature range of -40 °C to 100 °C.

The highest ionic conductivity (9.2×10^{-7} S cm^{-1}) is achieved for the material $Li_{1.5}Sc_{0.2}Zr_{1.8}Si_{0.3}P_{2.7}O_{12}$ with the lowest silicate content, and any further increase in silicate content leads to a sharp decrease in ionic conductivity. In contrast, the silicate-free material $Li_{1.2}Sc_{0.2}Zr_{1.8}P_3O_{12}$ has a higher conductivity than $Li_{1.5}Sc_{0.2}Zr_{1.8}Si_{0.3}P_{2.7}O_{12}$ (Table 4.2.3), showing that substitution with $(SiO_4)^{4-}$ is not beneficial throughout the series. These results are consistent with the XRD studies. The excess of non-substituting silicate forms a large amount of $ZrSiO_4$, as is clear from the XRD patterns in Figure 4.2.3, starting with the material $Li_{1.5}Sc_{0.2}Zr_{1.8}Si_{0.3}P_{2.7}O_{12}$, which only has two peaks assigned to $ZrSiO_4$. The increasing amounts of precipitates of Li_3PO_4, ZrO_2, Li_2SiO_3, and $ZrSiO_4$ have a significantly negative influence on ionic conductivity.

Table 4.2.4: Ionic conductivity at 25 °C and activation energy for $Li_{1.2+x}Sc_{0.2}Zr_{1.8}Si_xP_{3-x}O_{12}$ ($0.3 \leq x \leq 1.8$). For comparison, the $\sigma_{25°C}$ value of $Li_{1.2}Sc_{0.2}Zr_{1.8}P_3O_{12}$ is included (see [50]).

x	**Relative density / %**	**$\sigma_{25°C}$ / S cm^{-1}**	**Activation energy / eV**
0	94	4.8×10^{-5}	-
0.3	93	9.2×10^{-7}	0.26
0.8	94	4.5×10^{-7}	0.27
1.3	91	9.4×10^{-8}	0.13

1.8	94	8.2×10^{-9}	0.11

Among the materials of the $Li_{3+x}Sc_2Si_xP_{3-x}O_{12}$ series ($0 \leq x \leq 0.6$), $Li_{3.15}Sc_2Si_{0.15}P_{2.85}O_{12}$ shows the highest ionic conductivity (1.2×10^{-5} S cm^{-1}) at 25 °C with a relative density of 93 % after sintering in two steps at 1000 °C and 800 °C for 0.25 h and 4 h, respectively. The analogous series with sodium-based NaSICON materials, i.e. $Na_{3+x}Sc_2Si_xP_{3-x}O_{12}$ with $0 < x < 0.8$ [75, 76], was investigated earlier and showed increasing conductivity before reaching a maximum at $x = 0.4$, after which point there was an unfavorable ratio of the amount of charge carriers to vacancies. The $Na_{3.4}Sc_2Si_{0.4}P_{2.6}O_{12}$ material crystallized with the rhombohedral structure, and an ionic conductivity of 6.9×10^{-4} S cm^{-1} at 25 °C was reported with a relative density of 92 %.

The material with $x = 0$ in the $Li_{1.2+x}Sc_{0.2}Zr_{1.8}Si_xP_{3-x}O_{12}$ series ($0 \leq x \leq 2.8$) showed the highest ionic conductivity (4.8×10^{-5}) at 25 °C with a relative density of 94 %. An almost identical series of sodium-based NaSICON materials with the formula $Na_{3+x}Sc_xZr_{2-x}Si_2PO_{12}$ ($0 \leq x \leq 0.6$) was reported by Ma et al. [51]. An optimum total ionic conductivity of 4.0×10^{-3} S cm^{-1} at 25 °C was achieved with $Na_{3.4}Sc_{0.4}Zr_{1.6}Si_2PO_{12}$; a relative density of 95 % was obtained by free sintering at 1260 °C for 5 h. The XRD patterns of this compound show the presence of a mixture with 55 and 45 % of monoclinic and rhombohedral symmetry, respectively.

The comparison of lithium-based NaSICON materials with sodium-based analogues shows that the highest values of ionic conductivity can be obtained with the sodium-based NaSICON materials [51, 75,76], and we can conclude that the materials with zirconium in their structure have a higher ionic conductivity than materials with scandium.

The activation energy E_a of the ionic conductivity of all compounds except $x = 2.3$ and 2.8 was obtained from impedance measurements in the temperature range of -40 °C to 100 °C as shown in Figure 4.2.5b and summarized in Table 4.2.4. The E_a of $Li_{1.2+x}Sc_{0.2}Zr_{1.8}Si_xP_{3-x}O_{12}$ ($0.3 \leq x \leq 1.8$) specimens decrease from 0.26 eV to 0.11 eV with increasing x. Whereas the E_a values for $x = 0.3$ and 0.8 are again in good agreement with previous work, the samples with $x = 13$ and 1. 8 show exceptionally low activation energies. These low activation energies may be explained with the increasing amount of $ZrSiO_4$ which leads to an excess of lithium oxide in the matrix, the formation of additional lithium compounds and, hence, to an enhanced hygroscopicity of the samples. Therefore it cannot be excluded that the low E_a values in combination with the low ionic conductivities are a result of mixed Li^+/H^+ conductivity.

V Stability

5.1 Electrochemical stability window

5.1.1 Characterization of electrochemical stability window using cyclic voltammetry

In general, oxide and phosphate electrolytes feature higher electrochemical stability and a broader electrochemical window than sulfide, polymer, or liquid electrolytes [55, 63]. One of the most promising Li-ion solid electrolytes with a NaSICON structure like LATP, however, still faces challenges in the low voltage range due to the reduction of Ti^{4+} to Ti^{3+} in direct contact with lithium anodes [64]. For this purpose, selected NaSICON electrolytes such as LiZr$_2$(PO$_4$)$_3$ (LZP), Li$_{1.2}$Y$_{0.2}$Zr$_{1.8}$(PO$_4$)$_3$ (LYZP), and Li$_3$Sc$_2$(PO$_4$)$_3$ (LSP) were investigated with regard to their reduction stability range.

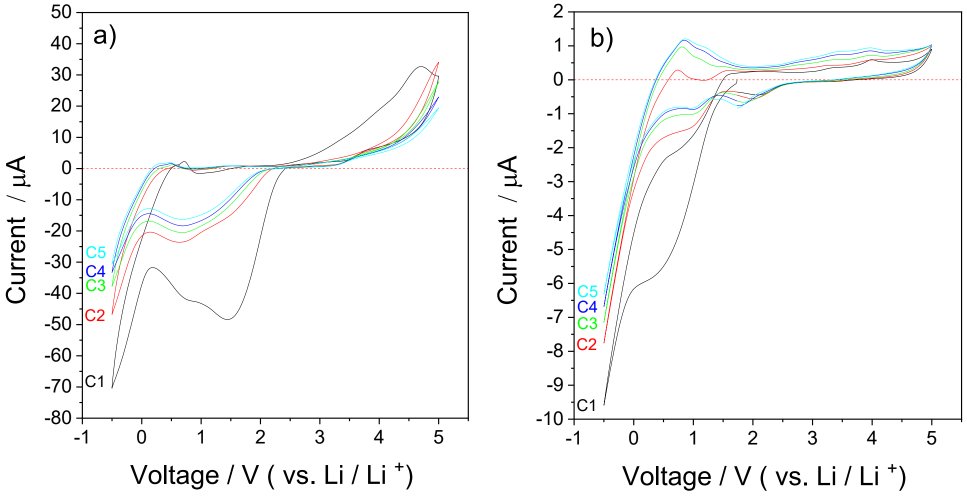

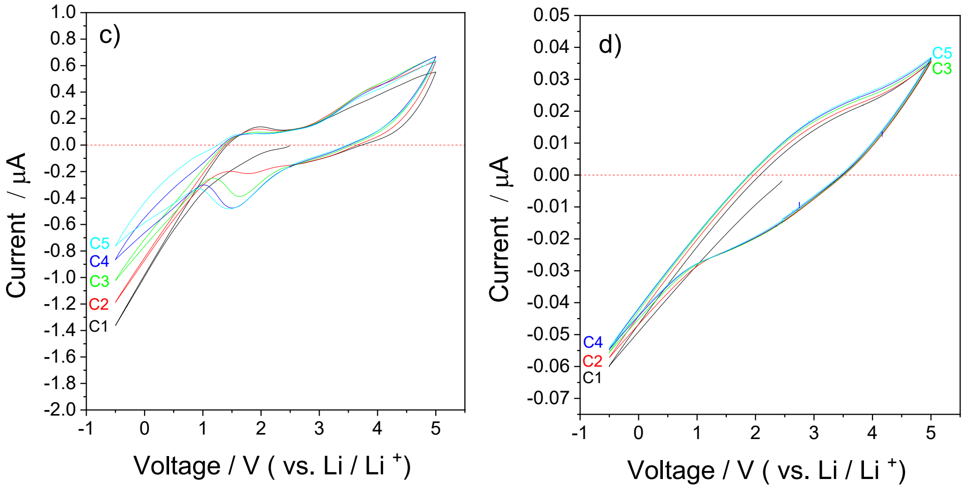

Figure 5.1: Cyclic voltammograms of a) LATP, b) LYZP, c) LZP, and d) LSP in Au│NaSICON│Li cells ranging from -0.5 to 5 V with a speed of 1 mV s^{-1}

Asymmetric cells in which the sintered pellets of the selected materials LZP, LYZP, and LSP were sandwiched between the Au and Li electrodes (Au│NaSICON│Li) were investigated by cyclic voltammetry (CV). Similar characterization was also performed for $Li_{1.5}Al_{0.5}Ti_{1.5}(PO_4)_3$ (LATP) to compare its electrochemical stability window with that of LZP, LYZP, and LSP.

As mentioned earlier, titanium-containing materials are instable against lithium [65] and indeed the cyclic voltammograms of LATP shown in Figure 5.1a confirm the reactions occurring during cycling. A pair of broad quasi-reversible peaks corresponding to the Ti^{4+}/Ti^{3+} redox process is observed at an average potential of about 2.6 V vs. Li^+/Li, with the onset of Ti^{4+} to Ti^{3+} reduction starting as early as ~ 2.5 V vs. Li^+/Li and the peak potential at ~ 1.7 V vs. Li^+/Li. The peak of the corresponding oxidation process is observed at ~ 4.7 V vs. Li^+/Li [66, 67]. The current density decreases in the following cycles, indicating a low Coulomb efficiency of this process. These peaks are superimposed on the reduction current at negative potentials below ~ 1 V, which correspond to the Li plating process with a possible formation of Li alloys (e.g. Li–Au alloy due to the reaction with the Au adhesion layer) [68].

The substitution of Ti^{4+} with Zr^{4+} and Sc^{3+} significantly increases the reduction stability of the resulting compounds, as shown in Figure 5.1b-d. In contrast to LATP, a reduction process is observed at much more negative potentials in LYZP, with a reduction onset at ~ 1.5 V vs. Li^+/Li and a peak potential at ~ 0.5 V vs. Li^+/Li. The cause of this process is still unknown, although it is thought to be the reduction of Zr^{4+} [15], which is in good agreement with the detection of the Zr^{3+} species in the XPS spectra described in Section 5.1.2. However, the exact origin of this process and the compounds formed still needs to be confirmed. It should be mentioned, however, that the reduction current is much lower compared to LATP and that the current corresponding to this process decreases sharply in the subsequent cycles. In the reverse scan, a very small peak of an oxidation process is observed at a potential of ~ 4 V vs. Li^+/Li, and in the second reduction scan, a very small reduction peak is detected at ~ 1.7 V vs. Li^+/Li. This peak most likely corresponds to the reduction of a compound formed during the oxidation scan, but the origin of this process still needs to be explained.

LZP (Figure 5.1c) and LSP (Figure 5.1d) generally exhibit very low currents and poor electrochemical performance due to their low ionic conductivity in the range of 10^{-7} S/cm, and LSP in particular shows near-Ohmic behavior. LZP, similar to LYZP, shows a linear onset of reduction currents at potentials below ~ 1 V vs. Li^+/Li. These currents can also be attributed to the reduction of Zr^{4+} and Li plating at more negative potentials, which are, however, poorly resolved due to the low ionic conductivity of this compound and the resulting high resistive polarizations. In the oxidation scan, a small oxidation peak is observed at a potential of ~ 4 V vs. Li^+/Li, with the corresponding reverse reduction peak detected in the second reduction scan. The potential of these peaks is similar to those of LYZP and likely to have the same origin.

LSP (Figure 5.1d) exhibited the widest electrochemical window of all the compounds studied, with no reduction or oxidation peaks detected in the potential range from -0.5 V to 5 V vs. Li^+/Li, but showed high Ohmic polarization due to its low ionic conductivity.

The conclusions about the reduction stability of the investigated NaSICON materials obtained by CV measurements are in good agreement with the optical appearance of the pellets after contact with Li metal. As shown in Figure 5.2 b), f), and j), no instant color change was observed for LSP, LZP, and LYZP after direct contact with lithium metal. However, in the case of the LATP electrolyte (Figure 5.2n), an immediate color change from white to black was clearly observed after direct contact with lithium metal. A longer exposure time with lithium metal of up to 24 h did not lead to a color change in the case of LSP (Figure 5.1c), while the zirconium-containing materials LZP and LYZP started to react locally, as shown in Figures 5.1g) and 5.1k). In the case of LZP, only isolated black spots were observed, while in the case of LYZP, the majority of the surface was colored black. However, the chemical stability of these materials to Li metal is much higher than that of LATP, which reacted completely with the adhering Li metal and formed a thick black layer on the entire surface.

After a cycling test of asymmetric Au|NaSICON|Li cells at RT for 100 hours, no change was observed on the surface of the LSP pellet, while LZP and LYZP showed some color changes. LZP formed a considerable number of black spots, and the LYZP showed a black layer on the surface of the pellet. However, LATP reacted completely with lithium metal and formed a very thick black layer on the surface, indicating the low stability of the solid electrolyte in contact with lithium.

The experiments show that LSP has very good chemical stability and no interaction with lithium, indicating the possibility of its direct combination with the lithium metal anode. LYZP and LZP exhibit much higher reduction stability than LATP, but react to some extent in direct contact with lithium metal.

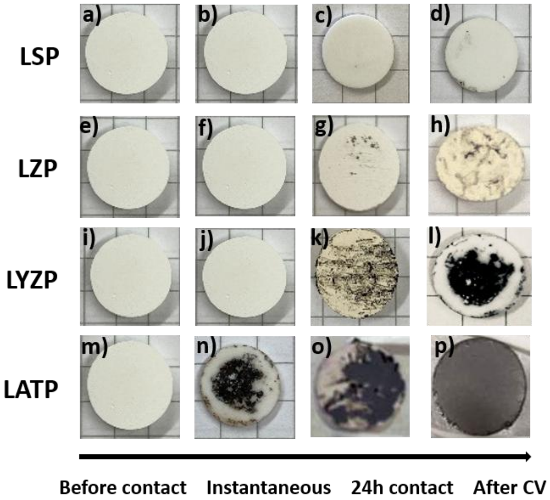

Figure 5.2: a-d) Pellets of LSP, e-h) LZP, i-l) LYZP and m-p) LATP after different exposure times with metallic lithium. The CV test was performed with Au|NaSICON|Li cells.

5.1.2 Characterization of the black surface layer on $Li_{1.2}Y_{0.2}Zr_{1.8}(PO_4)_3$ after cycling

After the cycling experiments, no indication of phase decomposition was observed by XRD, i.e. the black layer coating the surface of LYZP is most likely very thin or amorphous.
Therefore, XPS measurements were performed to explore the reaction products in more detail. In the first set of experiments, the black surface layer formed after cycling the Au│ LYZP │Li cell was investigated. For comparison, a second set of measurements was applied to characterize LYZP after heat treatment at 1000 °C in an inert atmosphere (Ar) for 3 hours. Normalized C 1s, O 1s, P 2p, and Zr 3d XPS spectra of these samples are shown in Figure 5.3 together with the spectra of the reference sample. As seen in the C 1s spectra, there are slight differences between the samples. The treated samples indicate the formation of a small amount of high binding energy species (e.g. at 288.6 eV). Such a binding energy corresponds to C=O/O−C−O related species, which might also have formed during transport and the exposure of samples to the ambient atmosphere. In the O 1s spectra, the reference sample has two main peaks located at 531.4 eV and 532.3 eV. After contact with Li metal, the position of the low energy peak shifts to around 531.2 eV. However, upon high-temperature heat treatment, a new peak appears at around 530.1 eV. This may originate from near-surface phase transitions or reactions due to the thermal instability of the material in an Ar atmosphere, for example the formation of new oxide phases. Unfortunately, it is not possible to make precise deductions at this binding energy, since many metal oxide compounds exhibit peaks at this energy region.

In the P 2p spectra, all samples seem to consist of closely located spin orbit components of $Li_{1.2}Y_{0.2}Zr_{1.8}(PO_4)_3$. However, the sample that was in contact with Li metal shows a contribution from a new set of peaks, which may originate from the formation of Li_3P at around 133 eV. It has previously been reported that the reaction with Li can result in the formation of Li_8ZrO_6 and Li_3P [96, 140]. In this case, however, no additional crystalline phase was observed by XRD, which implies that an amorphous layer may contribute to the shift of the main O 1s peak to a lower binding energy. In the heated sample, the shift to a low binding energy is more significant and the contribution can be easily identified with the formation of the third peak (black). This clearly shows that the decomposition products are different for the samples in contact with Li and the heat-treated samples. The Zr 3d spectra also confirm these differences (note that the brown peak in the Zr 3d spectra is due to the P 2s contribution).

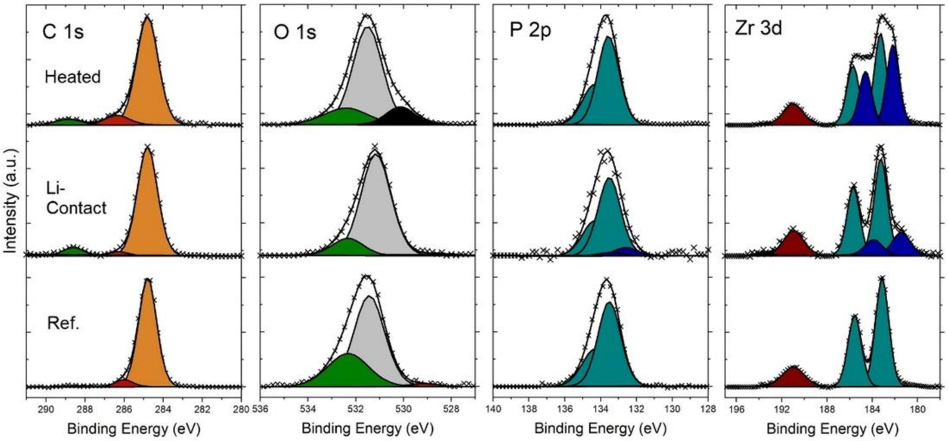

Figure 5.3: XPS spectra of $Li_{1.2}Y_{0.2}Zr_{1.8}(PO_4)_3$ samples before and after reduction either via Li contact or heating in an Ar atmosphere at 1000 °C. Normalized C 1s, O 1s, P 2p, and Zr 3d spectra from left to right.

For the heat-treated sample, the formation of a lower energy set of spin orbit peaks (shown in blue) is much more intense and positioned at slightly lower energies. The largest 3d 5/2 signal of the reference sample appears at 183.2 eV, which is in very good agreement with the binding energy of 183.1 eV for Zr^{4+} ions in ZrO_2 [141]. For the sample that was heat-treated in Ar, the additional doublet appears at a shift of about 1 eV peaking at 182.2 eV of the larger signal. In the case of Li contact, peaks are again shifted to lower energies (largest peak at 181.4 eV). The overall peak shift agrees with a previous study on the interfacial stability of Li and LZP [140] and with the binding energy of Zr^{3+} (182.1-181.8 eV depending on the experimental conditions) [141]. Therefore, both reducing conditions lead to the formation of Zr^{3+} ions and are the reason for the black coloration.

Although the relative concentration of decomposition products is not high, depth profiling (Annex 11) shows that the formation of Li-rich compounds is not limited to the surface and can be detected with high intensity after the sputtering process. It shows that the surface of the sample (which might also consist of residual Li metal) reacted with the atmosphere during storage and transport after the removal of the Li metal contact.

VI Conclusion

The focus of this thesis was to increase the reduction stability of NaSICON compounds by replacing critical Ge^{4+} and Ti^{4+} ions with more reduction-stable ions. With this aim, NaSICON materials with partial cation substitution in $Li_{1+x}M_xZr_{2-x}P_3O_{12}$ with M = Sc, Y, Al, partial polyanion substitutions in $Li_{3+x}Sc_2Si_xP_{3-x}O_{12}$ with $0 \leq x \leq 0.6$ (derived from the parent compound $Li_3Sc_2(PO_4)_3$) and the partial polyanion substitution of P^{5+} with Si^{4+} in the $Li_{1.2+x}Sc_{0.2}Zr_{1.8}Si_xP_{3-x}O_{12}$ system with $0 \leq x \leq 2.8$ were synthesized and the effect of substitution on crystallographic parameters, relative density, sintering temperature, ionic conductivity, and electrochemical stability systematically investigated.

The main results of this work can be summarized as follows:

Partial cation substitution

XRD investigations of materials in the $Li_{1+x}M^{3+}_xZr_{2-x}(PO_4)_3$ system where M = Al, Sc, Y indicated that the samples contained different polymorphs of the NaSICON structure and crystallized with rhombohedral ($R\bar{3}c$) or monoclinic ($P2_1/n$) symmetries, or a mixture of both. In some cases, reflections of the orthorhombic phase (*Pbcn*) were also detected in addition to those of the $R\bar{3}c$ and $P2_1/n$ symmetries. The purity and crystallographic structure of the materials strongly affected the ionic conductivity. The compositions where x = 0.2 in the three systems showed the highest ionic conductivity, as these compositions exhibited high purity and a well-crystallized rhombohedral NaSICON structure. Ionic conductivity significantly increased from 5.4×10^{-7} S cm^{-1} for the unsubstituted $LiZr_2(PO_4)_3$ to 3.6×10^{-6} S cm^{-1}, 2.7×10^{-5} S cm^{-1}, and 6.7×10^{-5} S cm^{-1} for the compositions $Li_{1.2}Al_{0.2}Zr_{1.8}(PO_4)_3$, $Li_{1.2}Sc_{0.2}Zr_{1.8}(PO_4)_3$, and $Li_{1.2}Y_{0.2}Zr_{1.8}(PO_4)_3$, respectively, with a consistent relative density of 94-96%. Therefore, those three compositions were selected from the systems to further optimize sintering conditions, improve densification, and increase ionic conductivity using the two-step sintering method and FAST/SPS. Sintering the materials using the two-step sintering process resulted in the reduction of pores and of micro-crack formation. The application of this sintering procedure not only increased the density of the samples, but also reduced the loss of lithium oxide because the samples remained at a high temperature only for a short period of time. Ionic conductivity was improved for the three compositions by increasing the density, and the highest value after optimizing the sintering conditions was 7.3 × 10^{-5} S cm^{-1} for the composition $Li_{1.2}Y_{0.2}Zr_{1.8}(PO_4)_3$.

Partial polyanion substitutions

Rietveld refinement of room temperature powder XRD patterns of materials of the $Li_{3+x}Sc_2Si_xP_{3-x}O_{12}$ series with $0 \leq x \leq 0.6$ derived from the parent compound $Li_3Sc_2(PO_4)_3$ and the partial substitution of P^{5+} with Si^{4+} in the $Li_{1.2+x}Sc_{0.2}Zr_{1.8}Si_xP_{3-x}O_{12}$ system with $0 \leq x \leq 2.8$ revealed the incidence of mixed orthorhombic and monoclinic symmetry in all cases. Optimizing the sintering conditions through two-step sintering led to enhanced relative density and limited Li_2O loss because the sample is exposed to shorter durations at high temperature (depending on composition) and increased ionic conductivity. The total ionic conductivity initially increases with increasing x in the $Li_{3+x}Sc_2Si_xP_{3-x}O_{12}$ series and the maximum value of conductivity (1.2 × 10^{-5} S cm^{-1}) was obtained with $Li_{3.15}Sc_2Si_{0.15}P_{2.85}O_{12}$. This trend can be mainly attributed to the substitution of silicate in $Li_{3+x}Sc_2Si_xP_{3-x}O_{12}$ and the additional Li^+ ions needed for charge balance. Consequently, more lithium ions led to a significant improvement in ionic conductivity. Although the ionic conductivity was improved along the series, it still remains at a level that is unfavorable for battery application.

The series $Li_{1.2+x}Sc_{0.2}Zr_{1.8}Si_xP_{3-x}O_{12}$ was synthesized for the first time and the highest ionic conductivity was achieved for the material $Li_{1.5}Sc_{0.2}Zr_{1.8}Si_{0.3}P_{2.7}O_{12}$ with the lowest silicate content (9.2 × 10^{-7} S cm^{-1}). Any further increase in silicate content leads to a sharp decrease in ionic conductivity. Therefore, it can be concluded that this Zr-containing series showed the highest ionic conductivity without silicate substitution. Because of the increasing amounts of additional phases, the substitution with $(SiO_4)^{4-}$ is not beneficial throughout the series.

The NaSICON materials $LiZr_2(PO_4)_3$, $Li_{1.2}M_{0.2}Zr_{1.8}(PO_4)_3$ (M = Sc, Y) and $Li_3Sc_2(PO_4)_3$ were selected and electrochemically investigated with respect to their reduction stability. For comparison, the electrolyte $Li_{1.5}Al_{0.5}Ti_{1.5}(PO_4)_3$ was also included in the studies. Finally, $Li_3Sc_2(PO_4)_3$ proved to be chemically and electrochemically very stable and might act as an anode protection material in combination with lithium metal.

Annexes

Annex 1: Ionic conductivity of $Li_{3+2x}(Sc_{1-x}Mg_x)_2(PO_4)_3$, $Li_{3-2x}(Sc_{1-x}M_x)_2(PO_4)_3$ (M = Ti, Zr, Sn, Hf), and $Li_{3-4x}(Sc_{1-x}M_x)_2(PO_4)_3$ (M = Nb, Ta) at room temperature [1].

Series	**x**	**log σ (S cm^{-1})**
$Li_{3-2x}(Sc_{1-x}Mg_x)_2(PO_4)_3$	0	-7.84
	0.025	-7.54
	0.05	-5.59
	0.1	-5.16
	0.15	-5.45
$Li_{3-2x}(Sc_{1-x}Ti_x)_2(PO_4)_3$	0.02	-7.27
	0.05	-7.03
	0.08	-5.56
	0.1	-5.13
	0.2	-4.99
	0.3	-5.27
$Li_{3-2x}(Sc_{1-x}Zr_x)_2(PO_4)_3$	0.025	-6.18
	0.05	-5.67
	0.75	-5.05
	0.1	-4.94
	0.2	-5.91
	0.3	-6.53
$Li_{3-2x}(Sc_{1-x}Sn_x)_2(PO_4)_3$	0.05	-7.08
	0.1	-5.75
	0.2	-5.58
$Li_{3-2x}(Sc_{1-x}Hf_x)_2(PO_4)_3$	0.05	-5.47
	0.1	-5.19
	0.2	-6.09
$Li_{3-4x}(Sc_{1-x}Nb_x)_2(PO_4)_3$	0.025	-6.69
	0.05	-6.47
	0.1	-5.09
	0.125	-5.42
	0.15	-5.58
$Li_{3-4x}(Sc_{1-x}Ta_x)_2(PO_4)_3$	0.025	-6.70
	0.05	-6.35
	0.1	-5.66
	0.15	-5.69

Annex 2: Shrinkage curves up to 1600 °C of a) $Li_{1+x}Sc_xZr_{2-x}(PO_4)_3$, b) $Li_{1+x}Y_xZr_{2-x}(PO_4)_3$, and c) $Li_{1+x}Al_xZr_{2-x}(PO_4)_3$.

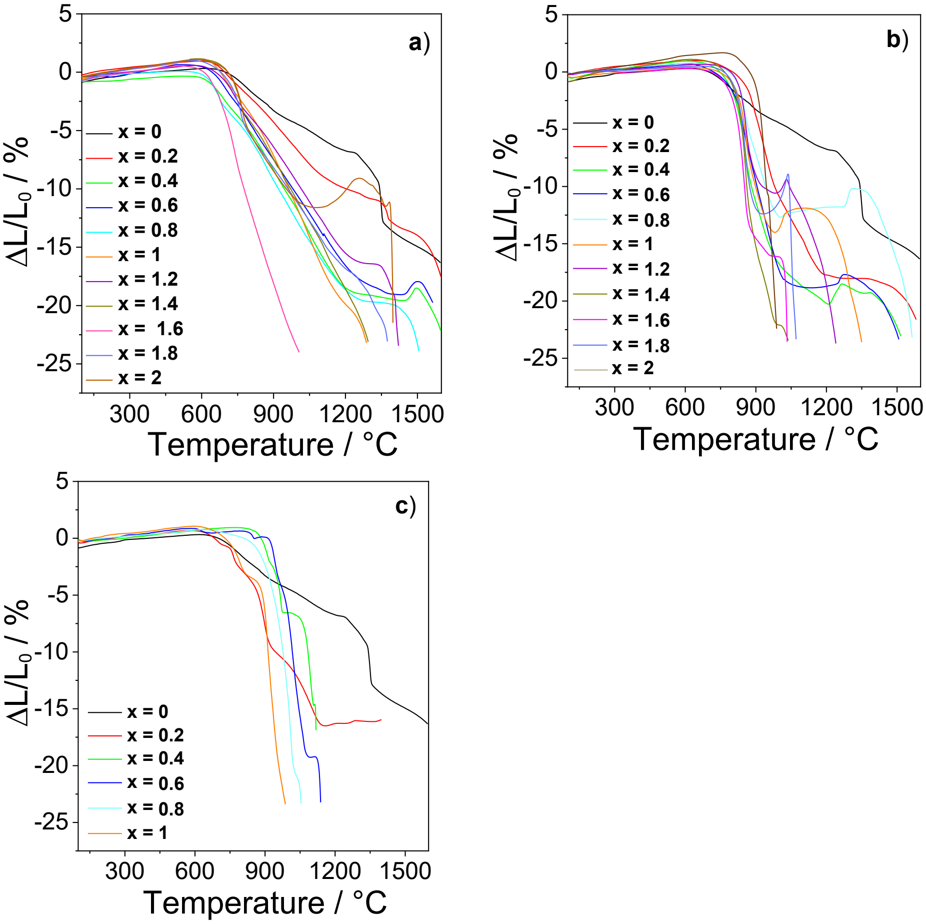

Annex 3: Converted lattice parameters and unit cell volume for LSZP (0 ≤ x ≤ 2).

x	Material	a (Å)	b (Å)	c (Å)	β (°)	V (Å^3)	Space group
Rhombohedral (space group R$\bar{3}c$) → Monoclinic (space group $P2_1/n$)							
0	$LiZr_2(PO_4)_3$	9.066	8.808	12.641	92.309	1008.62	$P2_1/n$
0.2	$Li_{1.2}Sc_{0.2}Zr_{1.8}(PO_4)_3$	8.970	8.864	12.611	90.955	1002.56	$P2_1/n$
0.4	$Li_{1.4}Sc_{0.4}Zr_{1.6}(PO_4)_3$	8.965	8.885	12.622	90.7240	1005.36	$P2_1/n$
0.6	$Li_{1.6}Sc_{0.6}Zr_{1.4}(PO_4)_3$	8.966	8.889	12.629	90.5910	1006.46	$P2_1/n$
0.8	$Li_{1.8}Sc_{0.8}Zr_{1.2}(PO_4)_3$	8.968	8.895	12.631	90.664	1007.63	$P2_1/n$
1	$Li_2ScZr(PO_4)_3$	8.948	8.834	12.574	91.0370	993.90	$P2_1/n$
1.2	$Li_{2.2}Sc_{1.2}Zr_{0.8}(PO_4)_3$	8.95	8.839	12.579	91.004	994.97	$P2_1/n$
1.4	$Li_{2.4}Sc_{1.4}Zr_{0.6}(PO_4)_3$	8.950	8.839	12.579	91.007	995.23	$P2_1/n$
1.6	$Li_{2.6}Sc_{1.6}Zr_{0.4}(PO_4)_3$	8.952	8.846	12.585	90.961	996.56	$P2_1/n$
1.8	$Li_{2.8}Sc_{1.8}Zr_{0.2}(PO_4)_3$	8.807	8.841	12.371	90.003	963.24	$P2_1/n$
2	$Li_3Sc_2(PO_4)_3$	8.856	8.807	15.156	125.756	959.26	$P2_1/n$
Orthorhombic (space group *Pbcn*) → Monoclinic (space group $P2_1/n$)							
1.6	$Li_{2.6}Sc_{1.6}Zr_{0.4}(PO_4)_3$	8.854	8.785	12.365	90	961.8	$P2_1/n$
1.8	$Li_{2.8}Sc_{1.8}Zr_{0.2}(PO_4)_3$	8.841	8.807	12.371	90	963.2	$P2_1/n$
2	$Li_3Sc_2(PO_4)_3$	8.807	8.856	12.299	90	959.3	$P2_1/n$

Annex 4: Converted lattice parameters and unit cell volume for LYZP (0.2 ≤ x ≤ 1.6).

x	Material	a (Å)	b (Å)	c (Å)	β (°)	V (Å^3)	Space group
Rhombohedral (space group $R\bar{3}c$) → Monoclinic (space group $P2_1/n$)							
0.2	$Li_{1.2}Y_{0.2}Zr_{1.8}(PO_4)_3$	8.958	8.861	12.601	90.876	1000.07	$P2_1/n$
0.4	$Li_{1.4}Y_{0.4}Zr_{1.6}(PO_4)_3$	8.982	8.869	12.624	91.022	1005.51	$P2_1/n$
Orthorhombic (space group *Pbcn*) → Monoclinic (space group $P2_1/n$)							
0.4	$Li_{1.4}Y_{0.4}Zr_{1.6}(PO_4)_3$	8.829	12.438	8.948	90	982.67	$P2_1/n$
0.6	$Li_{1.6}Y_{0.6}Zr_{1.4}(PO_4)_3$	8.831	12.41	8.951	90	981.99	$P2_1/n$
0.8	$Li_{1.8}Y_{0.8}Zr_{1.2}(PO_4)_3$	8.921	8.819	12.41	90	976.35	$P2_1/n$
1	$Li_2YZr(PO_4)_3$	8.903	8.804	12.372	90	969.74	$P2_1/n$
1.2	$Li_{2.2}Y_{1.2}Zr_{0.8}(PO_4)_3$	8.818	8.888	12.355	90	968.31	$P2_1/n$
1.4	$Li_{2.4}Y_{1.4}Zr_{0.6}(PO_4)_3$	8.820	8.886	12.344	90	967.45	$P2_1/n$
1.6	$Li_{2.6}Y_{1.6}Zr_{0.4}(PO_4)_3$	8.830	8.882	12.30	90	964.67	$P2_1/n$

Annex 5: Converted lattice parameters and unit cell volume for LAZP (0.2 ≤ x ≤ 1).

x	**Material**	**a (Å)**	**b (Å)**	**c (Å)**	**β (°)**	**V (Å³)**	**Space group**
Rhombohedral (space group R$\bar{3}c$) → Monoclinic (space group $P2_1/n$)							
0.2	$Li_{1.2}Al_{0.2}Zr_{1.8}(PO_4)_3$	8.979	8.858	12.613	91.089	1003.02	$P2_1/n$
0.4	$Li_{1.4}Al_{0.4}Zr_{1.6}(PO_4)_3$	8.957	8.841	12.5855	91.050	996.51	$P2_1/n$
0.6	$Li_{1.6}Al_{0.6}Zr_{1.4}(PO_4)_3$	8.952	8.831	12.5743	91.089	993.85	$P2_1/n$
0.8	$Li_{1.8}Al_{0.8}Zr_{1.2}(PO_4)_3$	8.951	8.831	12.5742	91.086	993.81	$P2_1/n$
1	$Li_2AlZr(PO_4)_3$	8.951	8.831	12.5741	91.083	993.76	$P2_1/n$

Annexes 6: Lattice parameters, cell volume, and space group of materials with the composition $Li_{1+x}M_xZr_{2-x}P_3O_{12}$ where M = Sc, Y, Al, as taken from the literature.

x	**a (Å)**	**b (Å)**	**c (Å)**	**β (°)**	**V (Å³)**	**V/Z (Å³)**	**Space group**	**Ref.**
0	8.8600(1)	8.8600(1)	22.065(1)	90	1500.04	250.01	R$\bar{3}c$	[2]
0	8.81277	8.9452	12.375	90.801	975.45	243.86	$P2_1/n$	[3]
0	15.0718	8.8556	9.112	123.912	1010.53	252.63	C$\bar{1}$	[4]
0	8.8549	8.8549	22.1440	90	1503.69	250.62	R$\bar{3}c$	[5]
0	8.86	8.86	22.06	90	1500.0	250	R$\bar{3}c$	[6]
0	8.854	8.854	22.1442	90	1503.38	250.56	R$\bar{3}c$	[7]
0	8.8600	8.8600	22.0650	90	1500.1	250.02	R$\bar{3}c$	[15]
M = Sc								
1.8	12.3542	8.794	8.820	90	958.33	239.58	Pbcn	[8]
1.8	12.370	8.8086	8.8356	90	962.81	240.70	Pbcn	[9]
1.8	8.836	12.366	8.798	90	961.26	240.32	Pbcn	[10]
1.96	8.8572	12.2998	8.8183	90.05(5)	960.68	240.17	$P2_1/n$	[9]
2	8.8483(4)	12.274(5)	8.7959(4)	90.015(6)	955	238.75	$P2_1/n$	[8]
2	8.860(3)	12.279(2)	8.804(2)		957.88	239.47	$P2_1/n$	[10]
2	8.853(2)	12.273(2)	8.802(1)	90.02(2)	956.36	239.09	$P2_1/n$	[11]
2	8.853(2)	12.273(2)	8.802(2)	90.00(2)	956.36	239.10	$P2_1/n$	[12]
2	8.828	12.399	8.823	90	965.75	241.44	Pcan	[12]
2	8.829	12.397	8.821	90	965.49	241.373	Pcan	[13]
M = Y								
0.1	8.8698	8.8698	22.1344	90	1507.86	251.31	R$\bar{3}c$	[15]
01.5	8.8727	8.8727	22.1578	90	1510.41	251.74	R$\bar{3}c$	[15]
0.2	8.8838	8.8838	22.1488	90	1513.84	252.31	R$\bar{3}c$	[15]
M = Al								
0.05				90	1510	251.67	R$\bar{3}c$	[14]
0.1				90	1500	250	R$\bar{3}c$	[14]
0.2				90	1495	249.17	R$\bar{3}c$	[22]
0.25				90	1490	248.33	R$\bar{3}c$	[14]
0.275				90	1487	247.83	R$\bar{3}c$	[14]
0.5				90	1486	247.67	R$\bar{3}c$	[14]

Annex 7: Orthorhombic unit cell parameters of $Li_{3+x}Sc_2Si_xP_{3-x}O_{12}$ ($0 \leq x \leq 0.6$).

Composition	**a / Å**	**b / Å**	**c / Å**	**V / Å^3**	**R$_{WP}$ / %**
$Li_3Sc_2P_3O_{12}$	12.292 (4)	8.861 (2)	8.812 (3)	959.8	8.11
$Li_{3.06}Sc_2Si_{0.06}P_{2.94}O_{12}$	12.301 (2)	8.867 (3)	8.812 (1)	961.2	6.93
$Li_{3.15}Sc_2Si_{0.15}P_{2.85}O_{12}$	12.295 (2)	8.861 (1)	8.813 (1)	960.1	7.78
$Li_{3.3}Sc_2Si_{0.3}P_{2.7}O_{12}$	12.324 (1)	8.879 (2)	8.826 (1)	965.8	9.14
$Li_{3.4}Sc_2Si_{0.4}P_{2.6}O_{12}$	12.451 (2)	8.875 (2)	8.835 (1)	976.2	8.22
$Li_{3.6}Sc_2Si_{0.6}P_{2.4}O_{12}$	12.385 (1)	8.829 (2)	8.804 (2)	962.7	9.04

Annex 8: Monoclinic unit cell parameters of $Li_{3+x}Sc_2Si_xP_{3-x}O_{12}$ ($0 \leq x \leq 0.6$).

Composition	**a / Å**	**b / Å**	**c / Å**	**β / °**	**V / Å^3**	**R$_{WP}$ / %**
$Li_3Sc_2P_3O_{12}$	8.819 (1)	8.845 (2)	12.286 (1)	89.939	958.398	5.91
$Li_{3.06}Sc_2Si_{0.06}P_{2.94}O_{12}$	8.848 (3)	8.845 (1)	12.295 (2)	89.939	962.305	4.78
$Li_{3.15}Sc_2Si_{0.15}P_{2.85}O_{12}$	8.850 (1)	8.845 (3)	12.299 (2)	89.990	962.775	4.83
$Li_{3.3}Sc_2Si_{0.3}P_{2.7}O_{12}$	8.855 (3)	8.845 (2)	12.299 (1)	90.102	963.285	6.05
$Li_{3.4}Sc_2Si_{0.4}P_{2.6}O_{12}$	8.798 (1)	8.845 (3)	12.397 (1)	90.170	964.781	5.39
$Li_{3.6}Sc_2Si_{0.6}P_{2.4}O_{12}$	8.828 (2)	8.845 (2)	12.452 (1)	89.801	972.287	5.55

Annex 9: Orthorhombic unit cell parameters of $Li_{1.2+x}Sc_{0.2}Zr_{1.8}Si_xP_{3-x}O_{12}$ ($0.3 \leq x \leq 1.8$).

Composition	**a / Å**	**b / Å**	**c / Å**	**V / Å^3**	**R$_{wp}$ / %**
$Li_{1.2}Sc_{0.2}Zr_{1.8}P_3O_{12}$					
$Li_{1.5}Sc_{0.2}Zr_{1.8}Si_{0.3}P_{2.7}O_{12}$	12.371 (1)	8.803 (2)	8.924 (1)	971.84	2.97
$Li_2Sc_{0.2}Zr_{1.8}Si_{0.8}P_{2.2}O_{12}$	12.413 (3)	8.813 (1)	8.910 (2)	974.72	2.98
$Li_{2.5}Sc_{0.2}Zr_{1.8}Si_{1.3}P_{1.7}O_{12}$	12.397 (3)	8.803 (1)	8.909 (1)	972.25	3.85
$Li_3Sc_{0.2}Zr_{1.8}Si_{1.8}P_{1.2}O_{12}$	12.271 (1)	8.709 (3)	8.748 (3)	934.81	5.06

Annex 10: Monoclinic unit cell parameters of $Li_{1.2+x}Sc_{0.2}Zr_{1.8}Si_xP_{3-x}O_{12}$ ($0.3 \leq x \leq 1.8$).

Composition	**a / Å**	**b / Å**	**c / Å**	**β / °**	**V / Å^3**	**R$_{wp}$ / %**
$Li_{1.2}Sc_{0.2}Zr_{1.8}P_3O_{12}$	8.864 (1)	8.970 (3)	12.611 (2)	90.955	1002.56	6.12
$Li_{1.5}Sc_{0.2}Zr_{1.8}Si_{0.3}P_{2.7}O_{12}$	8.764 (2)	8.964 (1)	12.429 (3)	91.039	976.27	5.07
$Li_2Sc_{0.2}Zr_{1.8}Si_{0.8}P_{2.2}O_{12}$	8.771 (3)	8.956 (2)	12.431 (1)	90.923	976.37	1.98
$Li_{2.5}Sc_{0.2}Zr_{1.8}Si_{1.3}P_{1.7}O_{12}$	8.768 (3)	8.957 (1)	12.425 (1)	90.824	975.70	6.03
$Li_3Sc_{0.2}Zr_{1.8}Si_{1.8}P_{1.2}O_{12}$	8.758 (1)	8.988 (3)	12.367 (2)	91.042	973.33	7.97

Annex 11: C 1s, O 1s, P 2p, Zr 3d, and Li 1s spectra of $Li_{1.2}Y_{0.2}Zr_{1.8}P_3O_{12}$ samples before and after various sputtering times. The data are shown without normalization.

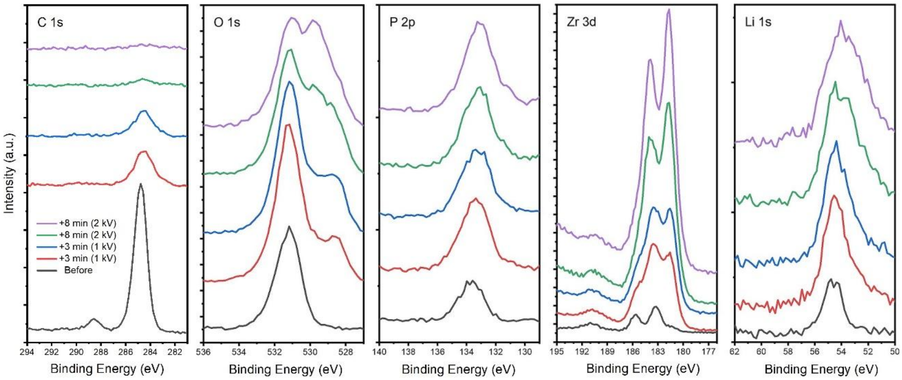

List of Publications

1. K. Lasri, D. Brandell, I. Saadoune, M. Larzek, K. Edström, Electrochemical characterizations of $Co_{0.5}TiOPO_4$ as anode material for lithium-ion batteries. Solar Energy Materials and Solar Cells, 2016. **148**: p. 44-51.
2. Z. Yang, J. Zhang, M. C. Kintner-Meyer, X. Lu, D. Choi, J. P. Lemmon, J. Liu, Electrochemical energy storage for green grid. Chemical reviews, 2011. **111**(5): p. 3577-3613.
3. H. Pan, Y. S. Hu, L. Chen, Room-temperature stationary sodium-ion batteries for large-scale electric energy storage. Energy & Environmental Science, 2013. **6**(8): p. 2338.
4. M. Armand, J. M. Tarascon, Building better batteries. nature, 2008. **451**(7179): p. 652.
5. M. Yoshio, R. J-Brodd, A. kozawa (Eds.), Lithium-Ion Batteries. Science And Technologies, Springer, 2009
6. Y. Nishi, Lithium ion secondary batteries; past 10 years and the future. Journal of Power Sources, 2001. **100**(1-2): p. 101-106.
7. Y. Xia, S. Shi, C. Li, C. Liang, Y. Gan, H. Huang, X. Tao, W. Zhang, Electrochemical properties of Sn-doped $Li_3V_2(PO_4)_3$ cathode material synthesized via a citric acid assisted sol–gel method. Journal of Alloys and Compounds, 2015. **652**: p. 298-306.
8. R. Essehli, I. Belharouak, H. Ben-Yahia, R. Chamoun, B. Orayech, B. El-Bali, K. Bouziane, X. Zhou, Z. L. Zhou, alpha-$Na_2Ni_2Fe(PO_4)_3$: a dual positive/negative electrode material for sodium ion batteries. Dalton Trans, 2015. **44**(10): p. 4526-32.
9. B. Dunn, H. Kamath, Jean-Marie. Tarascon, Electrical energy storage for the grid: a battery of choices. Science, 2011. **334**(6058): p. 928-935.
10. J. B. Goodenough, K. S. Park, The Li-Ion Rechargeable Battery: A Perspective. Journal of the American Chemical Society 2013, **135**(4), 1167-1176.
11. F. Zheng, M. Kotobuki, S. Song, M. O. Lai, L. Lu, Review on solid electrolytes for all-solid-state lithium-ion batteries. Journal of Power Sources, 2018. **389**: p. 198-213.
12. A. Rossbach, F. Tietz, S. Grieshammer, Structural and transport properties of lithium-conducting NASICON materials. Journal of Power Sources, 2018. **391**: p. 1-9.
13. P. Knauth, Inorganic solid Li-ion conductors: An overview. Solid State Ionics, 2009. **180**(14-16): p. 911-916.

14. X. Yao, B. Huang, J. Yin, G. Peng, Z. Huang, C. Gao, D. Liu, X. Xu, All-solid-state lithium batteries with inorganic solid electrolytes: Review of fundamental science. Chinese Physics B, 2016. **25**(1): p. 018802.

15. C. R. Mariappan, P. Kumar, A. Kumar, S. Indris, H. Ehrenberg, G.V. Prakash, R. Jose, Ionic conduction and dielectric properties of yttrium doped $LiZr_2(PO_4)_3$ obtained by a Pechini-type polymerizable complex route. Ceramics International, 2018. **44**(13): p. 15509-15516.

16. Z. Zhang, Y. Shao, B. Lotsch, Y.S. Hu, H. Li, J. Janek, F.L. Nazar, C.W. Nan, J. Maier, M. Armand, New horizons for inorganic solid state ion conductors. Energy & Environmental Science, 2018. **11**(8): p. 1945-1976.

17. P. J. Lian, B. S. Zhao, L. Q. Zhang, N. Xu, M.T. Wu, X. P. Gao, Inorganic sulfide solid electrolytes for all-solid-state lithium secondary batteries. Journal of Materials Chemistry A, 2019. **7**(36): p. 20540-20557.

18. D. T. Hallinan, I. Villaluenga, N.P. Balsara, Polymer and composite electrolytes. MRS Bulletin, 2018. **43**(10): p. 759-767.

19. L. Long, W. Shuanjin, X. Min, M. Yuezhong, Polymer electrolytes for lithium polymer batteries. Journal of Materials Chemistry A, 2016. **4**(26): p. 10038-10069.

20. J. C. Bachman, S. Muy, H. H. Chang, N. Pour, S. F. Lux, O. Paschos, F. Maglia, S. Lupart, P. Lamp, Inorganic solid-state electrolytes for lithium batteries: mechanisms and properties governing ion conduction. Chemical reviews, 2016. **116**(1): p. 140-162.

21. M. Hou, F. Liang, K. Chen, Y. Dai, D. Xue, Challenges and perspectives of NASICON-type solid electrolytes for all-solid-state lithium batteries. Journal of Nanotechnology, 2020. **31**(13): p. 132003.

22. J. Dai, C. Yang, C. Wang, G. Pastel, L. Hu, Interface Engineering for Garnet-Based Solid-State Lithium-Metal Batteries: Materials, Structures, and Characterization. Advanced Materials, 2018. **30**(48): p. 1802068.

23. H. Aono, N. Imanaka, G. Adachi, High Li^+ Conducting Ceramics. Accounts of Chemical Research, 1994. **27**(9): p. 265-270.

24. H. Aono, E. Sugimoto, Y. Sadaoka, N. Imanaka, G. Adachi, Ionic conductivity of solid electrolytes based on lithium titanium phosphate. Journal of the electrochemical society, 1990. **137**(4): p. 1023-1027.

25. A. Manthiram, X. Yu, S. Wang, Lithium battery chemistries enabled by solid-state electrolytes. Nature Reviews Materials, 2017. **2**(4): p. 16103.

26. M. Tatsumisago, A. Hayashi, Sulfide glass-ceramic electrolytes for all-solid-state lithium and sodium batteries. International Journal of Applied Glass Science, 2014. **5**(3): p. 226-235.

27. R. Kanno, M. Murayama, Lithium ionic conductor thio-LISICON: the $Li_2SGeS_2P_2S_5$ system. Journal of the electrochemical society, 2001. **148**(7): p. A742.

28. N. Kamaya, K. Homma, Y. Yamakawa, M. Hirayama, R. Kanno, M. Yonemura,T . Kamiyama,Y . Kato,S . Hama, K., Koji, A lithium superionic conductor. Nature materials, 2011. **10**(9): p. 682-686.

29. A. R. Kulkarni, H. S. Maiti, A. Paul, Fast ion conducting lithium glasses. Bulletin of Materials Science, 1984. **6**(2): p. 201-221.

30. F. Mizuno, A. Hayashi, K. Tadanaga, M. Tatsumisago, New, highly ion-conductive crystals precipitated from Li2S–P2S5 glasses. Advanced Materials, 2005. **17**(7): p. 918-921.

31. H. Muramatsu, A. Hayashi, T. Ohtomo, S. Hama, M. Tatsumisago, Structural change of Li_2S–P_2S_5 sulfide solid electrolytes in the atmosphere. Solid State Ionics, 2011. **182**(1): p. 116-119.

32. D. E. Fenton, Complexes of alkali metal ions with poly (ethylene oxide). polymer, 1973. **14**: p. 589.

33. F. M. Gray, J. R. MacCallum, C.A. Vincent, Poly (ethylene oxide)-$LiCF_3SO_3$-polystyrene electrolyte systems. Solid State Ionics, 1986. **18**: p. 282-286.

34. W. Gorecki, R. Andreani, C. Berthier, M. Armand, M . Mali, J. Roos, D, Brinkmann, NMR, DSC, and conductivity study of a poly (ethylene oxide) complex electrolyte: PEO ($LiClO_4$) x. Solid State Ionics, 1986. **18**: p. 295-299.

35. I. E. Kelly, J. R. Owen, B. C. H. Steele, Poly (ethylene oxide) electrolytes for operation at near room temperature. Journal of Power Sources, 1985. **14**(1-3): p. 13-21.

36. G. B. Appetecchi, F. Croce, B. Scrosati, Kinetics and stability of the lithium electrode in poly (methylmethacrylate)-based gel electrolytes. Electrochimica Acta, 1995. **40**(8): p. 991-997.

37. T. Iijima, Y. Toyoguchi, N. Eda, Quasi-solid organic electrolytes gelatinized with polymethyl-methacrylate and their applications for lithium batteries. Denki Kagaku, 1985. **53**(8): p. 619-623.

38. K. M. Abraham, M. Alamgir, Li^+ conductive solid polymer electrolytes with liquid-like conductivity. J Electrochem Soc, 1990. **137**(5): p. 1657-1658.

39. Z. Wang, B. Huang, H. Huang, L. Chen, R. Xue, F. Wang, Investigation of the position of Li^+ ions in a polyacrylonitrile-based electrolyte by Raman and infrared spectroscopy. Electrochimica acta, 1996. **41**(9): p. 1443-1446.

40. H. S. Choe, J. Giaccai, M. Alamgir, K. M. Abraham, Preparation and characterization of poly (vinyl sulfone)-and poly (vinylidene fluoride)-based electrolytes. Electrochimica acta, 1995. **40**(13-14): p. 2289-2293.

41. M. Alamgir, K. Abraham, Li ion conductive electrolytes based on poly (vinyl chloride). Journal of the Electrochemical Society, 1993. **140**(6): p. L96.

42. C. Capiglia, Y. Saito, H. Kataoka, T. Kodama, E. Quartarone, P. Mustarelli, Structure and transport properties of polymer gel electrolytes based on PVdF-HFP and LiN $(C_2F_5SO_2)_2$. Solid State Ionics, 2000. **131**(3-4): p. 291-299.

43. G. Feuillade, P. Perche, Ion-conductive macromolecular gels and membranes for solid lithium cells. Journal of Applied Electrochemistry, 1975. **5**(1): p. 63-69.

44. Y. F. Zhou, S. Xie, X. W. Ge, C. H. Chen, A. Amine, Preparation of rechargeable lithium batteries with poly (methyl methacrylate) based gel polymer electrolyte by in situγ-ray irradiation-induced polymerization. Journal of applied electrochemistry, 2004. **34**(11): p. 1119-1125.

45. G. B. Appetecchi, F. Croce, L. Persi, F. Ronci, B. Scrosati, Transport and interfacial properties of composite polymer electrolytes. Electrochimica Acta, 2000. **45**(8-9): p. 1481-1490.

46. B. Kumar, J. Fellner, Polymer ceramic composite protonic conductors. Journal of power sources, 2003. **123**(2): p. 132-136.

47. N. Miyake, J. S. Wainright, R.F. Savinell, Evaluation of a sol-gel derived Nafion/silica hybrid membrane for polymer electrolyte membrane fuel cell applications: II. Methanol uptake and methanol permeability. Journal of the Electrochemical Society, 2001. **148**(8): p. A905.

48. H. Gwon, J. Hong, H. Kim, D. H. Seo, S. Jeon, K. Kang, Recent progress on flexible lithium rechargeble batteries. Energy and Environemental science, 2014. **7** (2): p. 538-551.

49. W. L. Qiu, X. H. Ma, Q. H. Yang, Y. B. Fu, X. F. Zong, Novel preparation of nanocomposite polymer electrolyte and its application to lithium polymer batteries. Journal of Power Sources, 2004. **138**(1-2): p. 245-252.

50. S. S. Zhang, M. H. Ervin, K. Xu, T. R. Jow, Microporous poly (acrylonitrile-methyl methacrylate) membrane as a separator of rechargeable lithium battery. Electrochimica Acta, 2004. **49**(20): p. 3339-3345.

51. Y. Xiao, Y. Wang, S.H. Bo, J.C. Kim, L.J. Miara, G. Ceder, Understanding interface stability in solid-state batteries. Nature Reviews Materials, 2020. **5**(2): p. 105-126.

52. J. Janek, W.G. Zeier, A solid future for battery development. Nature Energy, 2016. **1**: p. 16141.

53. Y. Ren, K. Chen, R. Chen, T. Liu, Y. Zhang, C.W. Nan, Oxide electrolytes for lithium batteries. Journal of the American Ceramic Society, 2015. **98**(12): p. 3603-3623.

54. H. Y. P. Hong, Crystal structures and crystal chemistry in the system $Na_{1+x}Zr_2SixP_{3-x}O_{12}$. Materials Research Bulletin, 1976. **11**(2): p. 173-182.

55. J. B. Goodenough, H. Y. P. Hong, J. A. Kafalas, Fast Na+-ion transport in skeleton structures. Materials Research Bulletin, 1976. **11**(2): p. 203-220.

56. E. Rangasamy, L. Zengcai, G. Mallory, P. Kartik, S. Gayatri, Z. Wei, W. Hui, G. Steve, L. Chengdu, An iodide-based $Li_7P_2S_8I$ superionic conductor. Journal of the American Chemical Society, 2015. **137**(4): p. 1384-1387.

57. M. Rawlence, I. Garbayo, S. Buecheler, J. L. M. Rupp, On the chemical stability of post-lithiated garnet Al-stabilized $Li_7La_3Zr_2O_{12}$ solid state electrolyte thin films. Nanoscale, 2016. **8**(31): p. 14746-14753.

58. V. Thangadurai, S. Narayanan, D. Pinzaru, Garnet-type solid-state fast Li-ion conductors for Li batteries: critical review. Chemical Society Reviews, 2014. **43**(13): p. 4714-4727.

59. C. Wang, K. Fu, S. P. Kammampata, D. W. McOwen, A. J. Samso, L. Zhang, G. T. Hitz, A. M. Nolan, E. D. Wachsman, Y. Mo, Garnet-type solid-state electrolytes: materials, interfaces, and batteries. Chemical reviews, 2020. **120**(10): p. 4257-4300.

60. B. Orayech, (2015), Study of crystal structure and phase transition studies in perovskite-type oxides using powder-diffraction techniques and symmetry-mode analysis. (Doctoral dissertation).

61. S. J. Skinner, Recent advances in Perovskite-type materials for solid oxide fuel cell cathodes. International Journal of Inorganic Materials, 2001. **3**(2): p. 113-121.

62. H. Y. P. Hong, Crystal structure and ionic conductivity of $Li_{14}Zn$ $(GeO_4)_4$ and other new Li^+ superionic conductors. Materials Research Bulletin, 1978. **13**(2): p. 117-124.

63. U. V. Alpen, M. F. Bell, W. Wichelhaus, K. Y. Cheung, G. J. Dudley, Ionic conductivity of $Li_{14}Zn$ (GeO_{44} (Lisicon). Electrochimica Acta, 1978. **23**(12): p. 1395-1397.

64. D. Mazumdar, D.N. Bose, M. Mukherjee, Transport and dielectric properties of lisicon. Solid state ionics, 1984. **14**(2): p. 143-147.

65. J. Kuwano, A. R. West, New Li^+ ion conductors in the system, Li_4GeO_4-Li_3VO_4. Materials Research Bulletin, 1980. **15**(11): p. 1661-1667.

66. Y. W. Hu, I. D. Raistrick, R.A. Huggins, Ionic conductivity of lithium orthosilicate—lithium phosphate solid solutions. Journal of the Electrochemical Society, 1977. **124**(8): p. 1240.

67. S. Song, J. Lu, F. Zheng, H. M. Duong, L. Lu, A facile strategy to achieve high conduction and excellent chemical stability of lithium solid electrolytes. RSC advances, 2015. **5**(9): p. 6588-6594.

68. A. Hayashi, H. Muramatsu, T. Ohtomo, S. Hama, M. Tatsumisago, Improved chemical stability and cyclability in Li_2S–P_2S_5–P_2O_5–ZnO composite electrolytes for all-solid-state rechargeable lithium batteries. Journal of alloys and compounds, 2014. **591**: p. 247-250.

69. K. Minami, M.Keiichi, H. Akitoshi, U. Satoshi, T.Masahiro Electrical and electrochemical properties of glass–ceramic electrolytes in the systems Li_2S–P_2S_5–P_2S_3 and Li_2S–P_2S_5–P_2O_5. Solid State Ionics, 2011. **192**(1): p. 122-125.

70. N. Anantharamulu, K. Koteswara, G. Rambabu, B. Vijaya, V. Radha, M. Vithal, A wide-ranging review on Nasicon type materials. Journal of Materials Science, 2011. **46**(9): p. 2821-2837.

71. B. E. Taylor, A. D. English, T. Berzins, New solid ionic conductors. Materials Research Bulletin, 1977. **12**(2): p. 171-182.

72. R. DeWees, H. Wang, Synthesis and properties of NaSICON-type LATP and LAGP solid electrolytes. ChemSusChem, 2019. **12**(16): p. 3713-3725.

73. B. Kumar, D. Thomas, J. Kumar, Space-charge-mediated superionic transport in lithium ion conducting glass–ceramics. Journal of The Electrochemical Society, 2009. **156**(7): p. A506.

74. J. Fu, Fast Li^+ ion conducting glass-ceramics in the system Li_2O–Al_2O_3–GeO_2–P_2O_5. Solid State Ionics, 1997. **104**(3-4): p. 191-194.

75. P . Hartmann, T. Leichtweiss, M. R. Busche, M. Schneider, M. Reich, J. Sann, P. Adelhelm, J. Janek. Degradation of NaSICON-type materials in contact with lithium metal: formation of mixed conducting interphases (MCI) on solid electrolytes. The Journal of Physical Chemistry C, 2013. **117**(41): p. 21064-21074.

76. W. D. Richards, L. J. Miara, Y. Wang, J. C. Kim, G. Ceder, Interface stability in solid-state batteries. Chemistry of Materials, 2016. **28**(1): p. 266-273.

77. Y. Liu, Q. Sun, Y. Zhao, B. Wang, P. Kaghazchi, K. R. Adair, R. Li, C. Zhang, J. Liu, L.Y. Kuo, Stabilizing the interface of NaSICON solid electrolyte against Li metal with atomic layer deposition. ACS applied materials & interfaces, 2018. **10**(37): p. 31240-31248.

78. M. Catti, N. Morgante, R. M. Ibberson, Order–disorder and mobility of Li^+ in the β′-and β-$LiZr_2(PO_4)_3$ ionic conductors: A neutron diffraction study. Journal of Solid State Chemistry, 2000. **152**(2): p. 340-347.

79. V. Ramar, S. Kumar, S. R. Sivakkumar, P. Balaya, NaSICON-type La^{3+} substituted $LiZr_2(PO_4)_3$ with improved ionic conductivity as solid electrolyte. Electrochimica Acta, 2018. **271**: p. 120-126.

80. Y. Zhang, K. Chen, Y. Shen, L. Yuanhua, C.W. Nan, Enhanced lithium-ion conductivity in a $LiZr_2(PO_4)_3$ solid electrolyte by Al doping. Ceramics International, 2017. **43**: p. S598-S602.

81. A. Cassel, B. Fleutot, M. Courty, V. Viallet, M. Morcrette, Sol-gel synthesis and electrochemical properties extracted by phase inflection detection method of NaSICON-type solid electrolytes $LiZr_2(PO_4)_3$ and $Li_{1.2}Zr_{1.9}Ca_{0.1}(PO_4)_3$. Solid State Ionics, 2017. **309**: p. 63-70.

82. D. Petit, P. H. Colomban, G. Collin, J. P. Boilot, Fast ion transport in $LiZr_2(PO_4)_3$: Structure and conductivity. Materials research bulletin, 1986. **21**(3): p. 365-371.

83. F. Sudreau, D. Petit, J. P. Boilot, Dimorphism, phase transitions, and transport properties in $LiZr_2(PO_4)_3$. Journal of Solid State Chemistry, 1989. **83**(1): p. 78-90.

84. S. Kumar, P. Balaya, Improved ionic conductivity in NaSICON-type Sr^{2+} doped $LiZr_2(PO_4)_3$. Solid State Ionics, 2016. **296**: p. 1-6.

85. H. El-Shinawi, C. Greaves, J. Janek, Sol–gel synthesis and room-temperature properties of α- $LiZr_2(PO_4)_3$. RSC Advances, 2015. **5**(22): p. 17054-17059.

86. I. A. Stenina, I. Y. Pinus, A. I. Rebrov, A. B. Yaroslavtsev, Lithium and hydrogen ions transport in materials with NaSICON structure. Solid State Ionics, 2004. **175**(1-4): p. 445-449.

87. Y. Li, M. Liu, K. Liu, C. A. Wang, High Li^+ conduction in NASICON-type $Li_{1+x}Y_xZr_{2-x}(PO_4)_3$ at room temperature. Journal of Power Sources, 2013. **240**: p. 50-53.

88. T. Savitha, S. Selvasekarapandian, C. S. Ramya, Structural and electrical conductivity studies of $Li_xAlZr(PO_4)_3$ (x= 1.8, 2.0, 2.2), solid electrolyte for lithium-rechargeable batteries. Journal of Solid State Electrochemistry, 2008. **12**(7-8): p. 857-860.

89. T. Suzuki, K. Yoshida, K. Uematsu, T. Kodama, K. Toda, Z.G. Ye, M. Ohashi, M. Sato, Stabilization of superionic conduction phase in $Li_3Sc_2(PO_4)_3$. Solid State Ionics, 1997. **104**(1-2): p. 27-33.

90. G. G. Amatucci, A. Safari, F. K. Shokoohi, B. J. Wilkens, Lithium scandium phosphate-based electrolytes for solid state lithium rechargeable microbatteries. Solid State Ionics, 1993. **60**(4): p. 357-365.

91. P, Hui-Fen, G. Mei-Ling, W. Ming-Fang, Effect of annions substitutions of SiO_4 for $Li_3Sc_2(PO_4)_3$ superion conductor. Chinese Journal of Inorganic Chemestry 2011. **27**(10): p. 1969-1974.

92. M. Catti, A. Comotti, S. Di Blas, High-temperature lithium mobility in α-$LiZr_2(PO_4)_3$ NASICON by neutron diffraction. Chemistry of materials, 2003. **15**(8): p. 1628-1632.

93. S. Kumar, P. Balaya, Improved ionic conductivity in NASICON-type Sr^{2+} doped $LiZr_2(PO_4)_3$. Solid State Ionics, 2016. **296**: p. 1-6.

94. H. Xie, J.B. Goodenough, Y. Li, $Li_{1.2}Zr_{1.9}Ca_{0.1}(PO_4)_3$, a room-temperature Li-ion solid electrolyte. Journal of Power Sources, 2011. **196**(18): p. 7760-7762.

95. K. Arbi, M. Ayadi-Trabelsi, J. Sanz, Li mobility in triclinic and rhombohedral phases of the Nasicon-type compound $LiZr_2(PO_4)_3$ as deduced from NMR spectroscopy. Journal of Materials Chemistry, 2002. **12**(10): p. 2985-2990.

96. H. El-Shinawi, A. Regoutz, D.J. Payne, E.J. Cussen, S.A. Corr, NASICON $LiM_2(PO_4)_3$ electrolyte (M= Zr) and electrode (M= Ti) materials for all solid-state Li-ion batteries with high total conductivity and low interfacial resistance. Journal of Materials Chemistry A, 2018. **6**(13): p. 5296-5303.

97. J. Wolfenstine, S. Smith, T. Thompson, J. Sakamoto, J.L. Allen, D.R. Baker, Electrical, mechanical and chemical behavior of $Li_{1.2}Zr_{1.9}Sr_{0.1}(PO_4)_3$. Solid State Ionics, 2017. **300**: p. 38-45.

98. H. Xie, Y. Li, J.B. Goodenough, NASICON-type $Li_{1+2x}Zr_{2-x}Ca_x(PO_4)_3$ with high ionic conductivity at room temperature. RSC Advances, 2011. **1**(9): p. 1728-1731.

99. T. Šalkus, A. Kežionis, V. Kazlauskienė, J. Miškinis, A. Dindune, Z. Kanepe, J. Ronis, A.F. Orliukas, Surface and impedance spectroscopy studies of $Li_{2.8}Sc_{1.8-y}Y_yZr_{0.2}(PO_4)_3$ (where y = 0, 0.1) solid electrolyte ceramics. Materials Science and Engineering: B, 2010. **172**(2): p. 156-162.

100. T. Suzuki, K. Yoshida, K. Uematsu, T. Kodama, K. Toda, Z.G. Ye, M. Ohashi, M. Sato, Structure refinement of lithium ion conductors $Li_3Sc_2(PO_4)_3$ and $Li_{3-2x}(Sc_{1-x}M_x)_2(PO_4)_3$ (M = Ti, Zr) with x = 0.10 by neutron diffraction. Solid State Ionics, 1998. **113**: p. 89-96.

101. M. Sato, T. Suzuki, K. Yoshida, K. Uematsu, K. Toda, Z.G. Ye, Synthesis and properties of lithium ion conductors $Li_{3-2x}(Sc_{1-x}Zr_x)_2(PO_4)_3$. Journal of alloys and compounds, 1997. **250**(1-2): p. 510-514.

102. M. Sugantha, U.V . Varadaraju, Ionic conductivity of Li^+ ion conductors $Li_2M^{3+}M^{4+}P_3O_{12}$. Solid State Ionics, 1997. **95**(3-4): p. 201-205.

103. B. A. Maksimov, L. A. Muradyan, E. A. Genkina,V. I. Simonov, Crystal structure of the monoclinic modification of Li3Fe2(PO4)3. Soviet Physics Doklady, 1986. **31**: p. 370

104. T. Hupfer, E. C. Bucharsky, K. G. Schell, A. Senyshyn, M. Monchak, M. J. Hoffmann, H. Ehrenberg, Evolution of microstructure and its relation to ionic conductivity in $Li_{1+x}Al_xTi_{2-x}(PO_4)_3$. Solid State Ionics, 2016. **288**: p. 235-239.

105. E. D. Case, The effect of microcracking upon the Poisson's ratio for brittle materials. Journal of materials science, 1984. **19**(11): p. 3702-3712.

106. E. Antolini, Lithium loss kinetics from polycrystalline $Li_xNi_{1-x}O$ at high temperatures. Journal of Materials Chemistry, 1998. **8**(12): p. 2783-2786.

107. B. Davaasuren, F. Tietz, Impact of sintering temperature on phase formation, microstructure, crystallinity and ionic conductivity of $Li_{1.5}Al_{0.5}Ti_{1.5}(PO_4)_3$. Solid State Ionics, 2019. **338**: p. 144-152.

108. H. Bai, J. Hu, Y. Duan, F. Shao, T. Kozawa, M. Naito, J. Zhang, Influence of $LiBO_2$ addition on the microstructure and lithium-ion conductivity of $Li_{1+x}Al_xTi_{2-x}(PO_4)_3$ (x= 0.3) ceramic electrolyte. Ceramics International, 2018. **44**(6): p. 6558-6563.

109. W. Belam, A. Essoumhi, P. Satre, Synthesis and Physico-Chemical Characterizations of the Lithium-Substituted NASICONS Series with General Formula $Li_{2.8}Zr_{2-y}Si_{1.8-4y}P_{1.2+4y}O_{12}$ where ($0\leq y \leq 0.45$). Zeitschrift für Physikalische Chemie, 2007. **221**(2): p. 225-234.

110. S. Naqash, Q. Ma, F. Tietz, O. Guillon, $Na_3Zr_2(SiO_4)_2(PO_4)$ prepared by a solution-assisted solid state reaction. Solid State Ionics, 2017. **302**: p. 83-91.

111. T. Wriedt, W. Hergert, Mie Theory: a review, in Mie Theory. Vol. 169 of Springer Series in Optical Sciences.

112. W. Hergert, T. Wriedt, Mie Theory: a review, in Mie Theory. Springer, Berlin, Germany, 2012: p. 53-71.

113. K. Maca, V. Pouchly, A. R. Boccaccini, Sintering densification curve: A practical approach for its construction from dilatometric shrinkage data. Science of Sintering, 2008. **40**(2): p. 117-122.

114. H. Zhu, J. Liu, Emerging applications of spark plasma sintering in all solid-state lithium-ion batteries and beyond. Journal of Power Sources, 2018. **391**: p. 10-25.

115. A.M. Laptev, M. Bram, K. Vanmeensel, J. Gonzalez-Julian, O. Guillon Enhancing efficiency of field assisted sintering by advanced thermal insulation. Journal of materials processing technology, 2018. **262**: p. 326-339.

116. J. Cowley, J. L. Albain, G. G. Hembree, P. E. Ho/jlund-Nielsen, F. A. Koch, J. D. Landry, H. Shuman, System for reflection electron microscopy and electron diffraction at intermediate energies. Review of Scientific Instruments, 1975. **46**(7): p. 826-829.

117. B. Fultz, J. M. Howe, Inelastic electron scattering and spectroscopy. Transmission Electron Microscopy and Diffractometry of Materials, 2008: p. 163-221.

118. A. Le Bail, L. M. D. Cranswick, I. Madsen, A. Fitch, R. Allmann, C. Giacovazzo, A. Altomare, J. K. Cockcroft, R. Caliandro, P. Norby, Powder diffraction: theory and practice. 2008: Royal society of chemistry.

119. V. Petříček, M. Dušek, L. Palatinus, Crystallographic computing system JANA2006: general features. Zeitschrift für Kristallographie-Crystalline Materials, 2014. **229**(5): p. 345-352.

120. H. M. Rietveld, A profile refinement method for nuclear and magnetic structures. Journal of applied Crystallography, 1969. **2**(2): p. 65-71.

121. H. M. Rietveld, Line profiles of neutron powder-diffraction peaks for structure refinement. Acta Crystallographica, 1967. **22**(1): p. 151-152.

122. R. A. Young, P. E. Mackie, R. B. Von Dreele, Application of the pattern-fitting structure-refinement method of X-ray powder diffractometer patterns. Journal of Applied Crystallography, 1977. **10**(4): p. 262-269.

123. R. B. Von Dreele, Rietveld refinement, Powder Diffraction. 2008. p. 266-281.

124. R. A. Young, The Rietveld method. International Union of Crystallography and Oxford University Press. 1993, Oxford.

125. E. Barsoukov, J. R. Macdonald, Impedance Spectroscopy Theory, Experiment, and. Applications, 2005. Hoboken, NJ: John Wiley &Sons.

126. R. Ahmed, K. Reifsnider. Study of influence of electrode geometry on impedance spectroscopy. Conference: International Conference on Fuel Cell Science, Engineering and Technology, 2010. **44052** : p.167-175.

127. A. Lasia, Modern aspects of electrochemistry (eds) BE Conway, J O'M Bockris and RE White. 1999, New York: Kluwer Acadimic.

128. P. Hjalmarsson, M. Søgaard, M. Mogensen, Electrochemical behaviour of $(La_{1-x}Sr_x)_sCo_{1-y}Ni_yO_{3-\delta}$ as porous SOFC cathodes. Solid State Ionics, 2009. **180**(26-27): p. 1395-1405.

129. A. R .West, Solid state chemistry and its applications. 2014: John Wiley & Sons.

130. J. B. Goodenough, Oxide-ion electrolytes. Annual review of materials research, 2003. **33**(1): p. 91-128.

131. A. B. Bocarsly, Cyclic voltammetry. Characterization of Materials. Wiley Online Library, 2002.

132. P. Graves, D. Gardiner, Practical raman spectroscopy. Springer, 1989.

133. J. Narayan, Grain growth model for electric field-assisted processing and flash sintering of materials. Scripta materialia, 2013. **68**(10): p. 785-788.

134. A. Beran, E. Libowitzky, Spectroscopic methods in Mineralogy. 2004: The Mineralogical Society of Great Britain and Ireland.

135. T. C. Damen, S. Porto, B. Tell, Raman effect in zinc oxide. Physical Review, 1966. **142**(2): p. 570.

136. J. A. N. T. Soares, Introduction to optical characterization of materials, in Practical Materials Characterization. 2014, Springer , New York, NY. p. 43-92.

137. National Heart, Lung and Blood Institute, Guidelines for Physicochemical Characterization of Biomaterials, April 1979-1980: US Department of Health and Human Services, Public Health Service, National Institutes of Health.

138. J. D. Andrade, X-ray photoelectron spectroscopy (XPS), in Surface and interfacial aspects of biomedical polymers. 1985, Springer. p. 105-195.

139. M. Biesinger, X-ray Photoelectron Spectroscopy (XPS) reference pages. Surface Science Western, University of Western Ontario, Ontario, 2015.

140. Y. Li, W. Zhou, X. Chen, X. lu, Z. Cui, S. Xin, L. Xue, Q. Jia, J. B. Goodenouph Mastering the interface for advanced all-solid-state lithium rechargeable batteries. Proceedings of the National Academy of Sciences, 2016. **113**(47): p. 13313-13317.

141. Z. Bastl, A. I. Senkevich, I. Spirovová, V. Vrtílková, Angle-resolved core-level spectroscopy of Zr1Nb alloy oxidation by oxygen, water and hydrogen peroxide. Surface and Interface Analysis: An International Journal devoted to the development and application of techniques for the analysis of surfaces, interfaces and thin films, 2002. **34**(1): p. 477-480.

List of Tables

List of Figures

List of Abbreviations

AAM	Active Anode Material
ASSLiBs	All-Solid-State Li-ion Batteries
ASR	Area-Specific Resistance
CAM	Cathode active material
CTE	Coefficient of Thermal Expansion
CV	Cyclic Voltammetry or Cyclic Voltammogram
CPE	Constant Phase Element
DFT	Density Functional Theory
DTA	Differential Thermal Analysis
DSC	Differential Scanning Calorimetry
Ea	Ea Activation Energy
EDX	Energy-Dispersive X-ray spectroscopy
ESCA	Electron Spectroscopy for Chemical Analysis
FAST/SPS	Field-Assisted Sintering Technology / Spark Plasma Sintering
HT-XRD	High temperature X-Ray Diffraction
ICP-OES	Inductively Coupled Plasma Optical Emission Spectrometry
ICSD	Inorganic Crystal Structure Database
IEK	Institut für Energie- und Klimaforschung (Institute for Energy and Climate Research)
IS	Impedance Spectroscopy
LAGP	$Li_{1+x}Al_xGe_{2-x}(PO_4)_3$
LATP	$Li_{1+x}Al_xTi_{2-x}(PO_4)_3$
$LA_{0.5}TP$	$Li_{1.5}Al_{0.5}Ti_{1.5}(PO_4)_3$
LSZP	$Li_{1+x}Sc_xZr_{2-x}(PO_4)_3$
LIBs	Lithium Ion Batteries
LiSICON	Li^+ Super Ionic Conductor
$LS_{0.2}ZP$	$Li_{1.2}Sc_{0.2}Zr_{1.8}(PO_4)_3$
LYZP	$Li_{1+x}Y_xZr_{2-x}(PO_4)_3$
$LY_{0.2}ZP$	$Li_{1.2}Y_{0.2}Zr_{1.8}(PO_4)_3$

LAZP	$Li_{1+x}Al_xZr_{2-x}(PO_4)_3$
$LA_{0.2}ZP$	$Li_{1.2}Al_{0.2}Zr_{1.8}(PO_4)_3$
LZP	$LiZr_2(PO_4)_3$
LSP	$Li_3Sc_2(PO_4)_3$
LZS	$Li_4Zr_2Si_3O_{12}$
MS	Mass Spectrometry
NaSICON	Na^+ Super Ion Conductor
PAN	Poly(acrylonitrile)
PEO	Poly(ethylene oxide)
PMMA	Poly(methyl methacrylate)
PVDF	Poly(vinylidene fluoride)
PSD	Particle Size Distribution
Pt	Platinum
Rwp	Weighing profile factor
RT	Room Temperature
SA-SSR	Solution Assisted-Solid State Reaction
SEM	Scanning Electron Microscopy
SE	Secondary Electron
SSBs	Solid-State Batteries
SSEs	Solid-State Electrolytes
TG	Thermogravimetry
WDX	Wavelength Dispersive X-ray
XPS	X-ray photoelectron spectroscopy
XRD	X-Ray Diffraction
σ_{Total}, σ_b, σ_{gb}	Total conductivity, bulk conductivity, grain boundary conductivity

Acknowledgements

This PhD thesis owes gratitude towards several people without whom it would not have been possible to be completed, especially because of the pandemic challenges over the last two years. Their continuous support and help has indeed contributed over the whole PhD time.

My biggest acknowledgment goes to Dr. Frank Tietz, the group leader of Functional Materials at IEK-1, for accepting my application for master thesis research in 2018 and afterwards giving me the opportunity to work under his esteemed supervision. Frank never stopped helping and advising me along the way, I admire his brilliant scientific mind, his friendliness and his sense of humor. Thank you for trusting me and guiding me through these four years, thank you for your patience, motivation, and immense knowledge. I could not have imagined having a better advisor and mentor for my PhD study.

I would like to express my sincere gratitude to Prof. Dr. Dina Fattakhova, the head of the battery department for agreeing to supervise me and I am very thankful for her guidance, her constructive feedback and remarks in spite of a very busy schedule. Her prompt feedback on my submissions has indeed made it possible to complete this work in very challenging time. It was such a great experience to work under her esteemed supervision.

My sincere thanks also goes to Prof. Dr. Olivier Guillon, the director of IEK-1, for his insightful comments and encouragement, hard questions during my work report presentations which incented me to widen my research from various perspectives.

I would like to thank the following colleagues for contributing with this research project: Dr. Yoo Jung Sohn for XRD analysis, Mark Kappertz for helping on the preparation of SEM specimens and Dr. Doris Sebold for making the SEM investigations, Dr. Daniel Grüner for EDX analysis, Dr. Sandra Lobe for the Raman investigation. A special thank I address to Volker Bader, Marie-Theres Gerhards and Dr. Enkhtsetseg Dashjav for all the thermal treatments and the repair of all electronic compounds, DTA-TG measurement and Rietveld refinement, respectively. I also want to thank colleagues from my group, Dr. Qianli Ma, Dr. Monika Bhardwaj, also inspired me many times during my work on the thesis. Dr. Tu Lan, Dr. Apurv Dash, Aikai Yang, Ah-Ram Seok, Yavuz Selim with whom I have been sharing the office. Sven Uhlenbruck, Martin Finsterbusch, Philipp Odenwald, I learnt a lot from each of them especially during the Fest-Batt project meetings. ZEA-3 of Forschungszentrum Jülich for carrying out the ICP-OES measurements. From the Justus-Liebig University in Giessen, I have to thank Dr. Burak Aktekin for XPS investigations.

I would like to thank the crowd of the Helmholtz Interdisciplinary Doctoral Training in Energy and Climate Research (HITEC) School, especially Marianne Feldmann the managing director of the HITEC School. For fostering our interdisciplinary communication among all PhD students working in the fields of energy and climate research, enhancing our experience by providing additional scientific and professional qualifications and international exchanges that supplement our research work during our PhD time.

Last but not the least, I would like to thank the Deutsche Gesellschaft für Kristallographie (DGK) for giving me the opportunity to became a membership in the association and presenting my first conference: Conference Young Crystallographers DGK, held in Humboldt-Universität Berlin-Germany in 2016. Since that time I decided to continue my career in Germany and to start a new life outside of Morocco.

This work was supported by funding from the German Federal Ministry of Education and Research (BMBF) within the projects Festbatt-Oxide (03XP0173A) and Festbatt2-Oxide (13XP0434A) and is gratefully acknowledged.

Band / Volume 651
Integration of a rib-channel design to improve air-side contacting in solid oxide cell (SOC) stacks
Y. S. Ayhan (2024), 82 pp
ISBN: 978-3-95806-797-4

Band / Volume 652
Modelling Secondary Circulation in Convective Boundary Layer Using Large Eddy Simulation
L. Zhang (2024), 84 pp
ISBN: 978-3-95806-799-8

Band / Volume 653
Optionen zur Umsetzung der Klimaschutzziele im Verkehrssektor
S. Kraus (2025), XI, 317 pp
ISBN: 978-3-95806-802-5

Band / Volume 654
Modellierung der flächendifferenzierten Grundwasserneubildung für Schleswig-Holstein im Beobachtungszeitraum 1961-2021 und für Klimaszenarien bis 2100
I. McNamara, B. Tetzlaff, F. Wendland, T. Wolters (2025), 191 pp
ISBN: 978-3-95806-803-2

Band / Volume 655
Entwicklung alternativer Brenngaselektroden für die Hochtemperatur-Elektrolyse
F. E. Winterhalder (2025), vii, 161 pp
ISBN: 978-3-95806-805-6

Band / Volume 656
Oxide-based All-Solid-State Batteries for and from Recycling Processes
V. M. Kiyek (2025), viii, 128 pp, xix
ISBN: 978-3-95806-806-3

Band / Volume 657
Investigation of current and future anthropogenic chemical regimes in simulation chamber experiments
M. Färber (2025), 213 pp
ISBN: 978-3-95806-809-4

Band / Volume 658
Dynamischer Betrieb von Polymer-Elektrolyt-Membran Wasserelektrolyseuren
E. Rauls (2025), XIV, 239 pp
ISBN: 978-3-95806-811-7

Band / Volume 659
Pore-scale reactive transport modeling in cementitious materials: Development and application of a high-performance computing code based on the Lattice-Boltzmann method
S. Rohmen (2025), X, 295 pp
ISBN: 978-3-95806-812-4

Band / Volume 660
Recyclingmöglichkeiten für die Keramikkomponenten einer Festoxidzelle
S. Sarner (2025), VIII, 122 pp
ISBN: 978-3-95806-816-2

Band / Volume 661
Methodological Approach Enabling the Two-phase Flow Investigation in Alkaline Electrolysis under Demanding Conditions
S. Renz (2025), IX, 252 pp
ISBN: 978-3-95806-821-6

Band / Volume 662
Variable renewable energy potential estimates based on high-resolution regional atmospheric modelling over southern Africa
S. Chen (2025), XIII, 141 pp
ISBN: 978-3-95806-822-3

Band / Volume 663
Advances in Understanding Nitrate Aerosol Formation and the Implications for Atmospheric Radiative Balance
A. Milousis (2025), 195 pp
ISBN: 978-3-95806-823-0

Band / Volume 664
Optimization of NaSICON-type lithium- ion conductors for solid-state batteries
A. Loutati (2025), viii, 104 pp
ISBN: 978-3-95806-824-7

Weitere ***Schriften des Verlags im Forschungszentrum Jülich*** unter
http://wwwzb1.fz-juelich.de/verlagextern1/index.asp

Energie & Umwelt / Energy & Environment
Band / Volume 664
ISBN 978-3-95806-824-7

Mitglied der Helmholtz-Gemeinschaft

JÜLICH
Forschungszentrum